An Examination of Sea Ice Spring and Summer Retreat in the Canadian Arctic Archipelago: 1989 to 2010

by

Wenxia Tan

A thesis
presented to the University of Waterloo
in fulfillment of the
thesis requirement for the degree of
Doctor of Philosophy
in
Geography

Waterloo, Ontario, Canada, 2013

I hereby declare that I am the sole author of this thesis. This is a true copy of the thesis, including any required final revisions, as accepted by my examiners.

I understand that my thesis may be made electronically available to the public.

Abstract

The sea ice extent change and variability of the Canadian Arctic Archipelago (CAA) are quite different compared to the Arctic as a whole due to its unique geographic settings. In this thesis, the sea ice retreat processes, the connection with other Arctic regions, and the linkages to the surface radiation flux in the CAA are examined.

The sea ice retreat processes in the CAA follow a four-phase process: a slow ice melt phase that usually lasts until early June (phase 1); a quick melt phase with large daily sea ice extent change which lasts close to half-a-month (phase 2); a slow melt phase that looks like slow sea ice melt or even a small ice increase that lasts another half-a-month (phase 3); and a steady ice decrease phase (phase 4). With the help of Moderate-Resolution Imaging Spectroradiometer (MODIS) data, it is identified that the quick melt in phase 2 is actually melt ponding, with melt ponds being falsely identified as open water by passive microwave.

A simplified data assimilation method is then developed to improve the passive microwave sea ice concentration estimation by fusion with MODIS ice surface temperature data. The ice concentration from the analysis is found to improve the original passive microwave sea ice concentration estimation, with the largest improvements during sea ice melt.

The sea ice retreat patterns in the CAA region are correlated with the sea ice retreat patterns in other regions of the Arctic. A decision tree classifier is designed to segment the sea ice retreat patterns in the CAA into several classes and classification maps are generated. These maps are effective in identifying the geographic locations that have large changes in the sea ice retreat patterns through the years.

The daily progressions of the surface radiation components are described in detail. Due to the lack of multiple reflection, the percentage of shortwave radiation at the top of atmosphere that reaches the surface is influenced by the form of melt ponds over ice surface. The roles that each surface radiation component plays in forcing sea ice retreat are different in different years.

Acknowledgements

First and foremost, I would like to express greatest gratitude to my supervisor, Ellsworth LeDrew, for giving me the opportunity to pursue my Ph.D. with him, and for his guidance, inspiration, patience and trust throughout every stage of the process. Whenever I meet obstacles in research and feel frustrated, he never fails to give me helpful discussions, suggestions and confidence. His enlightened perspective and wisdom towards science and life have been a tremendous example for me. I feel very fortunate having the chance to work with him in the past four years.

I am grateful to my committee member, Richard Kelly, for all his help along the way of my study in Waterloo. Special thanks are given to Andrea Scott for her inspiration and useful discussions. Without her, chapter 5 of this research would not be possible. I also want to thank Claude Duguay for his detailed comments and Ed Jernigan for detailed corrections of the thesis. I wish to thank Steve Howell for the helpful suggestions and discussions and Alexander Brenning for the invaluable statistics advice. Thank Christina Haas for serving as the external of my thesis defence.

I would also like to thank Ziqiang Ou for taking me as a visiting graduate student at Canadian Ice Service, which has eventually led me to the world of sea ice. I would like to thank Julie Friddell for her help during my stay at CCIN. I wish to express my sincere thanks to Qingquan Li, Bijun Li and Bisheng Yang from Wuhan University for their continuous encouragement and help in all these years. I would like to thank many external academics for their willingness to share their time and thoughts with me through emails and through in person meetings.

I have worked with several course instructors within the department of Geography through teaching assistantships. Special thanks are given to Su-Yin Tan, Peter Glenday, Mike Lackner and Scott MacFarlane for their help during my TAs. Thank all the help from Susie Castela and Lynn Finch. Thank Jonathan Li for providing me the opportunity to come to Canada and start my Ph.D. study.

The provision of datasets by the National Snow and Ice Data Center (NSIDC) and European Centre for Medium-Range Weather Forecasts (ECMWF) is gratefully acknowl-

edged. Thanks all the people in these data centers and their time for answering my emails in a timely manner.

Friends also played a very important part especially during the hard times. Thanks to all of my friends, housemates and officemates for the company and help. I also want to thank the university Outers club for the awesome trips that let me explore the geographic nature of Canada and meet many other adventurers. A special thanks to my friend Ping Wu for her incredible willingness to lend an ear despite the 12 hour time difference.

And finally, I would like to thank my parents for their love and encouragement. I am sure that at times over the last few years they thought I would be in school forever, but they have always supported and encouraged me in all of my decisions. I owe my success to them.

Table of Contents

List of Tables

List of Figures

List of Abbreviations

ΔSIE Sea Ice Extent Change

3D-var Three-Dimensional variational

CAA Canadian Arctic Archipelago

CISDA Canadian Ice Service Digital Archive

EASE-Grid Equal-Area Scalable Earth Grid

ECMWF European Centre for Medium-Range Weather Forecasts

FYI First Year Ice

IMS NOAA Interactive Multisensor Snow and Ice Mapping System

IST Ice Surface Temperature

MODIS Moderate-Resolution Imaging Spectroradiometer

MYI Multi-Year sea Ice

NSIDC National Snow and Ice Data Center

QEI Queen Elizabeth Islands

SAT Surface Air Temperature

SIC Sea Ice Concentration

SIE Sea Ice Extent

SSM/I Special Sensor Microwave/Imager

YD Year Day

Chapter 1

Introduction and Statement of Objectives

1.1 Introduction

The recent two decades has witnessed a dramatic decline of Arctic sea ice cover. Not only are the ice extent and area decreasing, but also the ice is becoming thinner and younger (*Polyakov et al.*, 2012b). Arctic sea ice plays an important role in governing the climate system. Sea ice reflects much of the solar radiation in the summer and insulates the warm ocean from the cold atmosphere above in the winter (*Perovich and Richter-Menge*, 2009). Thus, the loss of Arctic sea ice has a great impact on the energy balance of the Earth (*Perovich and Polashenski*, 2012, *Persson*, 2012). The loss of Arctic sea ice has been attributed to some combination of influences of the changing atmospheric circulation patterns (*Overland et al.*, 2012) and the increase of solar heat input to the Arctic ice-ocean system due to albedo feedback (*Perovich et al.*, 2011a). However, the sea ice area change and variability of the Canadian Arctic Archipelago (CAA) are quite different compared to the Arctic as a whole due to its unique geographic settings (*Howell et al.*, 2008b, 2010). As of 2010, the record low sea ice extent for the Arctic Basin for the satellite era (since 1979) is year 2007 (*Stroeve et al.*, 2007), but that for the CAA is year 1998. Since the 1960s, sea ice area depletion in the CAA region has occurred in years 1962, 1971, 1976,

and 1984, 1998, 2007, 2008 and 2010. The mechanisms that control these depletion events are largely unknown, but the amount of ice inflow from Arctic Ocean is one of the key factors (*Howell et al.*, 2008a). Moreover, current sea ice research mainly focuses on the September minimum sea ice extent (*Tivy et al.*, 2011, *Parkinson and Cavalieri*, 2008), but sea ice is retreating throughout the year. Spring is the most critical time of the year for sea ice melting, and little work has been done to analyze the sea ice retreat in the spring season. Thus, there is a need to study the sea ice spring and summer retreat processes in the CAA region.

In this study, we aim to understand the processes responsible for the sea ice spring and summer retreat in the CAA region. The CAA is the main area of study, but the connections of the CAA with other Arctic regions are also explored. Firstly, the daily sea ice extent change in the spring and summer season is described. Secondly, the physical processes that explain the daily sea ice extent change are explored. Thirdly, using multiple sources of data, a simplified data assimilation technique is used to improve the estimation of sea ice concentration during sea ice retreat in the spring and summer. After that, we explore the connection of sea ice retreat in the CAA region with other Arctic regions even though we mainly focus on the CAA region. Finally, the linkages of daily sea ice retreat with the concurrent surface radiation balance are presented.

1.2 Statement of Objectives

The intention of this study is to provide an understanding of the sea ice spring and summer retreat processes for the CAA region. The main objectives and questions addressed in this study can be described as follows:

The first objective of this thesis is to provide an explicit description of the evolution of sea ice extent over a year from April to September using the sea ice concentration data of the recent 20 years. The purpose is to identify the general characteristics of sea ice retreat in the CAA region. Detailed sea ice retreat processes will be explored.

The second objective is to explore the possibility of using MODIS ice surface temperature data to improve the sea ice concentration estimation from passive microwave data

during the spring and summer sea ice retreat season.

The third objective is to understand how the sea ice retreat pattern in the CAA connects to other Arctic regions. The sea ice retreat pattern will be categorized as several types. The change of sea ice retreat pattern through the years will be understood.

The last objective is to provide an explicit description of the evolution of the surface radiation balance for the spring and summer sea ice retreat period using atmospheric reanalysis data. The characteristics of the radiation balance terms are analyzed for each of phases of sea ice spring and summer retreat. The relationships between the radiation terms and sea ice melt onset dates, total sea ice retreat amount in the entire melt season will be discussed.

1.3 Thesis Structure

This work is organized as follows: In chapter 2, we review the methods used to derive sea ice concentration information. Moreover, the change and variability of sea ice in the CAA region is summarized and the current understanding of sea ice melt processes in the CAA region is reviewed. In chapter 3, we provide a description of the datasets used in this study. In chapter 4, we focus on the sea ice retreat processes in the CAA Region. The physical processes that govern the sea ice retreat in the CAA is discussed. In chapter 5, we integrate MODIS ice surface temperature data with SSM/I passive microwave sea ice data to improve sea ice concentration estimation. In Chapter 6, we explore the connections of the sea ice retreat patterns in the CAA region with other Arctic regions. The changes in sea ice retreat pattern in different regions of the Arctic for recent years is examined. In chapter 7, we focus on the daily radiation profiles for the CAA region during spring and summer sea ice retreat. The connection between sea ice retreat and radiation in the CAA will be discussed. In chapter 8, we summarize the results from chapters 4 to 7 and outline direction for future research.

Chapter 2

Background and Literature Review

Arctic sea ice has undergone drastic changes in recent years. Satellite passive microwave sea ice monitoring has been conducted for more than thirty years. Numerous scientific papers have investigated the trend and variability of Arctic sea ice using passive microwave sea ice data. In this chapter, we first summarize the theories related to passive microwave sea ice remote sensing. The algorithms used for sea ice concentration estimation are briefly summarized. In the second section, we provide a comprehensive review of sea ice spatial and temporal variability in the CAA region at various scales. The mechanisms that govern the sea ice variability are presented, with special focus on the spring and summer seasons. The review is intended to provide background information for the analysis of daily sea ice spring and summer retreat process in the CAA region.

2.1 Passive Microwave Remote sensing of Sea Ice

2.1.1 Passive Microwave properties of Sea Ice

Microwave scattering and emission from sea ice are sensitive to the small variations in the composition and structure of sea ice (*Carsey*, 1992, *Lubin et al.*, 2006). Microwave signature of sea ice mainly depends on the dielectric and scattering properties of the ice

and its surface. Passive microwave radiometers measure the intensity of natural thermal emissions from the surface. The intensity of the emission is normally converted to an equivalent brightness temperature T_B. Assuming that atmospheric effects are negligible, there is a simple linear relationship between T_B and surface temperature T_S according to Rayleigh-Jeans approximation:

$$T_B(\lambda, pol, \theta_i) = \varepsilon(\lambda, pol, \theta_i) T_S \tag{2.1}$$

where *pol* is polarization (vertical or horizontal), i is the local incidence angle off-nadir, λ is the wavelength, and ε is the wavelength-, angular- and polarization-dependent emissivity.

Emissivity changes as the physical properties of sea ice and snow changes through dynamic and thermodynamic processes. The emissivities of first-year ice (FYI), multiyear ice (MYI), and the open ocean at different frequency and polarization have substantially difference as shown in Figure 2.1. These three surface types are most easily differentiated from each other at 20 GHz. For a given frequency and polarization, MYI has lower emissivities than FYI. As frequency increases from low to high, the emissivity of MYI drops greatly, while the emissivity of water increases as frequency increases. The emissivities of FYI only change a little bit from low to high frequencies. The above mentioned features can be used to developed algorithms to identify different surface types using multi-frequency and multi-polarization data.

Seasonal changes in Arctic sea ice and snow cover are illustrated schematically in Figure 2.2. As spring and summer melt period progress, the passive microwave emissivities of the surface change correspondingly at both 18 and 37 GHz. It can be seen that melt pond and ice-free ocean have similar emissivities. Therefore, the unambiguous distinction of actual open water from melt ponds/saturated snow is greatly affected.

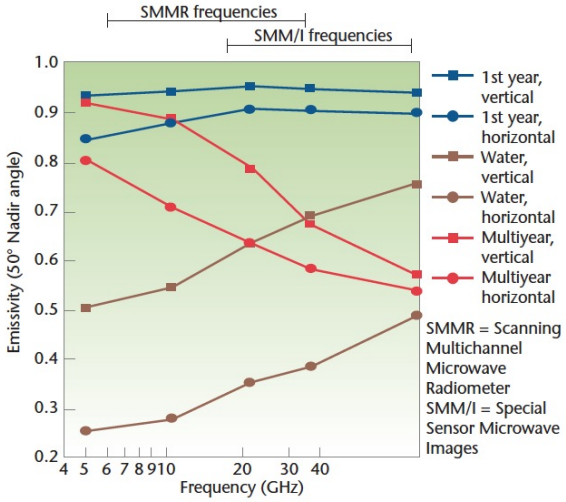

Figure 2.1: The emissivity of sea ice varies differently with microwave frequency depending on ice type and polarization. Adapted from *Lubin and Massom* (2007) and reproduced from *Svendsen et al.* (1983).

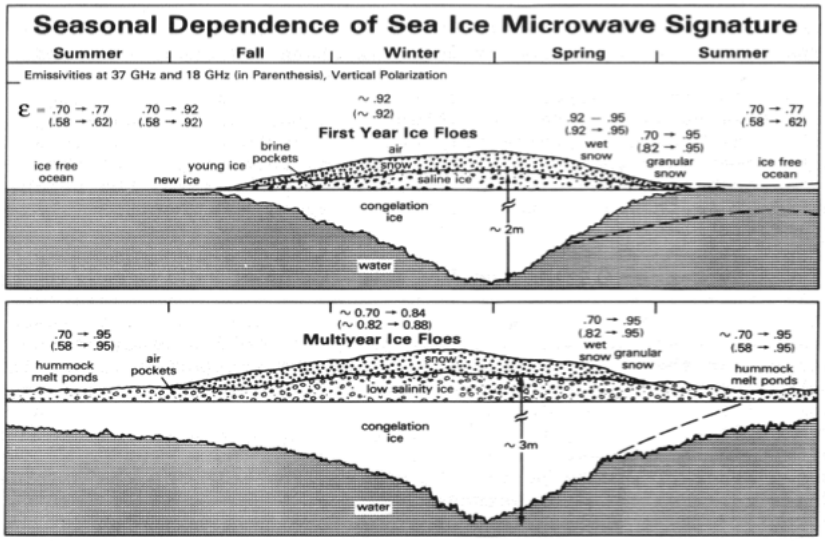

Figure 2.2: Schematic diagram of the seasonal dependence of physical and radiative characteristics of Arctic first-year and multiyear ice at 18 and 37GHz (vertical polarization) over an annual cycle. Adapted from *Lubin et al.* (2006).

2.1.2 Passive Microwave Sea Ice Concentration Data

Passive microwave remote sensing of sea ice is the most reliable long time source for monitoring the regional extent of Arctic sea ice. Systematic sea ice observation for the entire Arctic region are only available for the satellite era since 1972 since the launch of the Nimbus-5 Electrically Scanning Microwave Radiometer (ESMR). Following that, the passive microwave sensors are the Nimbus-7 Scanning Multichannel Microwave Radiometer (SMMR) (November 1978 through July 1987), and the Defense Meteorological Satellite Program (DMSP) -F8, -F11 and -F13 Special Sensor Microwave/Imager (SSM/I) (since August 1987), and the DMSP F-17 Special Sensor Microwave Imager/Sounder (SSMIS) (since April 2009). The SMMR SSM/I sea ice concentration (SIC) dataset is the most consistent long period dataset.

The physical characteristics of sea ice and snow cover can be extracted from the observed passive microwave brightness temperatures. A comprehensive review of algorithms developed to estimate SIC from passive microwave brightness temperatures can be found in *Andersen et al.* (2006). These algorithms use different sets of reference emissivities to represent different surface types. The set of references used are called tie points. Different algorithms make use of different frequencies and polarizations of the passive microwave data. Algorithms based solely on the 19 and 37 GHz vertically polarized channels display the smallest sensitivity to all three atmospheric attenuation parameters: total water vapour, wind speed, and cloud liquid water (*Andersen et al.*, 2006). Different algorithms have different error magnitude depending on the conditions of the ice surface and the atmosphere (*Andersen et al.*, 2007), but these algorithms generally agree with each other in estimating the long-term trend of sea ice. For the melt season, the uncertainties in the passive microwave sea ice data mainly include: the subpixel ambiguity due to the 25 km to 50 km pixel size, and the inability of passive microwave to distinguish melt ponds from open water. NASA Advanced Microwave Scanning Radiometer - Earth Observing System (AMSR-E), launched in 2002 and terminated in 2011 with higher spatial resolution than SSM/I, is another more recent sensor used for monitoring Arctic sea ice. AMSR-E sea ice concentration data are by far the highest spatial resolution for satellite microwave sea ice estimation (*Comiso and Nishio*, 2008).

Johannessen and Ivanova (2013) compared the sea ice extent and sea ice area calculated by several algorithms using Near-Real-Time DMSP SSM/I-SSMIS Daily Polar Gridded Brightness Temperatures, obtained from National Snow and Ice Data Center (NSIDC) for the period from 1979 to 2008. These algorithms include: NORSEX (*Svendsen et al.*, 1983), NASA Team (*Cavalieri et al.*, 1984), UMass-AES (*Swift et al.*, 1985), TUD (*T.*, 1998) and ASI (*Kaleschke et al.*, 2001), Bootstrap (*Comiso et al.*, 1997), Bristol (*Smith and Barrett*, 1994) and CalVal (*Ramseier*, 1991). Figure 2.3 compares the sea ice extent and sea ice concentration from these algorithms. It can be seen that discrepancies exist in the sea ice estimations from different algorithms, but they follow the same trend. Table 2.1 shows the publicly accessible daily SIC concentration data based on the above mentioned algorithms.

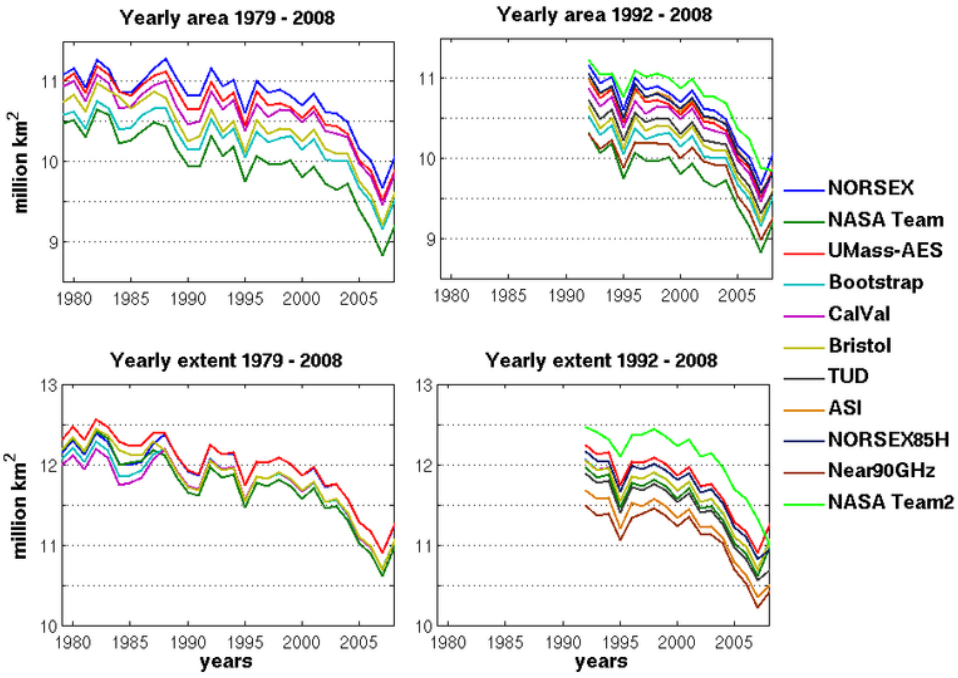

Figure 2.3: Comparison of sea ice extent and sea ice area calculated from several different algorithms using Near-Real-Time DMSP SSM/I-SSMIS Daily Polar Gridded Brightness Temperatures for the period from 1979 to 2008. Adapted from *Johannessen and Ivanova* (2013).

Table 2.1: Selected groups that provide publicly accessible daily Arctic Sea Ice Concentration using Near-Real-Time DMSP SSM/I-SSMIS Daily Polar Gridded Brightness Temperatures and their algorithms

Group	Algorithm	Channel
NASA Goddard Sea Ice Remote Sensing, USA	Bootstrap	19(V), 37(H,V)
	NASA Team	19(H,V), 37(V)
	Enhanced NASA Team	19(H,V), 85(H,V), 37(V)
Nansen Environmental and Remote Sensing Center, Norway	Norsex (Nansen Environmental and Remote Sensing Center Arctic ROOS)	19(V), 37(V)
EUMETSAT	OSI-SAF (A combined use of TUD, Bootstrap and Bristol)	19(V), 37(H,V), 85(H,V)

In addition to datasets that use SSM/I and AMSR-E satellite microwave sensors, other datasets are compiled from various sources, such as the sea ice extent data from NOAA Interactive Multisensor Snow and Ice Mapping System (IMS), and sea ice concentration and type information by Canadian Ice Service Digital Archive (CISDA). CISDA is a compilation of weekly ice charts covering Canadian Waters from the early 1960s to present (*Tivy et al.*, 2011). The CISDA are compiled using an integration of remotely sensed data, surface observations, airborne and ship reports, operational model results and the expertise of ice analysts through the years. The use of RADARSAT since 1996 is the most significant event for the CISDA dataset. RADARSAT C-band Synthetic Aperture Radar (SAR) provides relatively high resolution, all weather, day or night information on ice extent and concentration. The CISDA dataset has been used to investigate the ice dynamics (*Howell et al.*, 2009) and the multi-year sea ice (MYI) condition (*Howell et al.*, 2008b) in the CAA region for 1968 - 2006. The CISDA dataset is not used in this work because data is only available on a weekly basis and only for a selected period in summer.

2.1.3 Error Sources in Passive Microwave SIC

Errors in SIC retrieves from passive microwave sensors were summarized in *Lubin and Massom* (2007). Some errors are algorithm-specific. For example, the Bootstrap algorithm is sensitive to temperature variability. Other errors are common for all algorithms and they are summarized as the following:

1. Mixed pixel problem: As the sensor foot print becomes larger, several different ice types and/or open water may exist in the same grid. An averaged SIC is retrieved based on the mixed response from all the surface types in the foot print.

2. Unfiltered weather effects: Atmospheric contamination can pass through the weather filters and lead to erroneous SIC retrievals. For example, the wind-roughened open water or atmospheric water vapour can be misinterpreted as sea ice. Errors caused by weather effects are especially large at the ice edge and on thin ice.

3. Surface melt effects: In late spring and summer, because melt ponds are considered as a open water, SIC is underestimated.

4. Land contamination: In coastal areas, SIC retrieve may contain a contribution from land and ice sheet.

5. Emissivities vary spatially and temporally: Even at a given polarization and frequency, the emissivities of the same ice type vary greatly at different locations or at different times, as surface conditions changes.

   Thus, caution should be taken for trend analysis using data from different sources. Moreover, *Barber et al.* (2009) have reported much inconsistency between in situ observed sea ice condition and remotely sensed products based on the expedition in Southern Beaufort Sea in September 2009. Heavily decayed, very small remnant MYI and FYI floes were predicted as high ice concentrations by RADASAT because their near-surface radiometric and scattering characteristics were almost identical.

2.2 Review of Sea Ice Cover in Canadian Arctic

2.2.1 Geographic Settings of the Canadian Arctic Archipelago

The CAA region is comprised of a collection of islands and channels. The names of the islands and waterways of the CAA region are shown in Figure 2.4. The water areas in the CAA are almost entirely covered by landfast ice during the winter months and typically more than 50% of the ice is multi-year ice (MYI) (*Canadian Ice Service*, 2011). Summaries of the oceanography, sea ice, and climate conditions for the CAA region, especially the Sverdrup Basin, are detailed in *Melling et al.* (1984) and *Melling* (2002). The channels of the CAA provide pathways for the movement of sea ice between the Arctic and Atlantic Oceans. The total width that can allow for ice import to the CAA along the northwest margin of the Sverdrup Basin is 315 km. The principal openings are in Prince Gustaf Adolf Sea (95 km) and Peary Channel (90 km). Sea ice enters into Atlantic Ocean from the CAA region through Lancaster Sound and Jones Sound with a total channel width of 76 km. The small width for export contributes to the high summertime values of the ice concentration in the Sverdrup Basin.

There is a slow, broad southward current along the northwest shore of the CAA, and there is a clockwise current around each major island or island group within the Archipelago (*Canadian Ice Service*, 2011). A north-to-south waterway from Arctic Ocean through the Prince Gustaf Adolf Sea, Byam Martin Channel, Austin Channels, and Penny Strait towards Parry Channel across to M'Clintock Channel constantly exists when no ice is blocking, even in August when wind is directed to the north out of the M'Clintock Channel (*Marko*, 1977). There is a strong eastward flow on the south side of western Lancaster Sound and the flow is mainly barotropic. However, the current is weak on the north side of the Lancaster sound, and the flow is mainly baroclinic. The model study of *Wang et al.* (2012) found that the southward flow in M'Clintock Channel is driven by ageostrophic accelerations and is controlled by topography, while the circulation in eastern Lancaster Sound is influenced by both stratification and bathymetry.

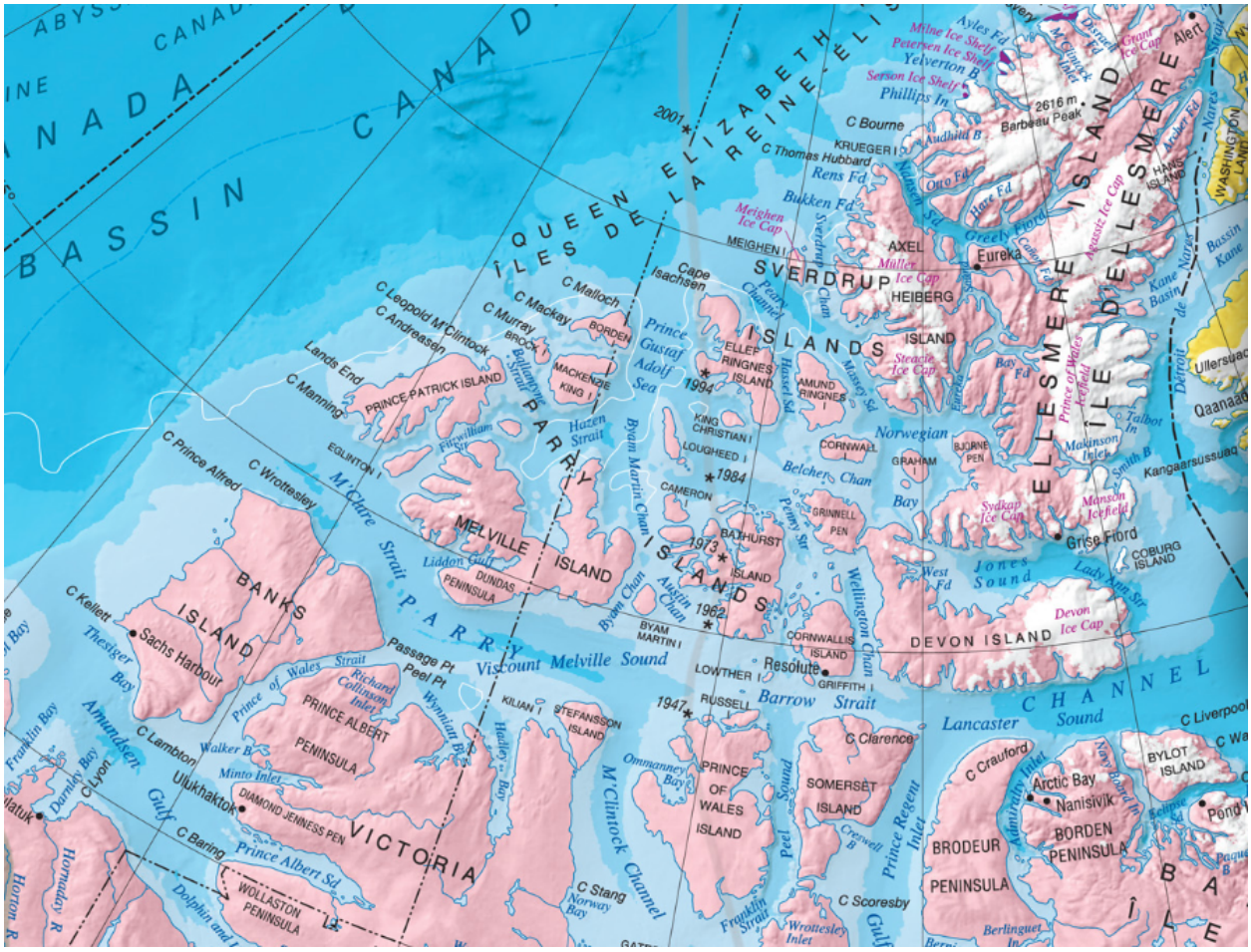

Figure 2.4: Map of Canadian Arctic Archipelago (CAA) region, from `http://atlas.nrcan.gc.ca/site/english/maps/reference/anniversary_maps/`

2.2.2 Sea Ice Extent, Area, Thickness in the CAA

Numerous studies have investigated the changes of Arctic sea ice extent, area, and concentration. The most up-to-date ones are *Parkinson and Cavalieri* (2008), *Perovich and Richter-Menge* (2009), and *Meier and Haas* (2011). Sea ice in the Canadian Arctic reaches maximum extent in March and minimum in September. Sea ice persists within the CAA throughout the year, although regions in the south and east of the CAA usually clear by

late summer. In late winter, undisturbed bare first year ice (FYI) can grow to a maximum thickness of about 2.4 m in northern portions of the CAA and 2 m of maximum thickness in the central and western Arctic, and up to 1.2 m farther south in James Bay and along the Labrador coast (*Canadian Ice Service*, 2011). MYI found in the Archipelago reaches a thickness of 3 to 4.50 m. The maximum end-of-winter snow thickness on sea ice was between 30 and 40 cm (*Brown and Cote*, 1992, *Flato and Brown*, 1996, *Melling*, 2002) in the CAA region.

Seasonally-averaged sea ice extents from 1979 to 2006 for each region in the Arctic are reported in *Parkinson and Cavalieri* (2008) using satellite passive microwave data. Negative trends of sea ice extent, but not statistically significant, were reported for the yearly averages and for each of the four seasons for the CAA region. When each of the 12 months is examined, October has the strongest negative slope, followed by September. The sea ice extent downward trend is normally more significant in the summer than in winter (Figure 2.5). However, if the sea ice extent is measured as the zonal mean sea ice edge latitude, an annually constant retreat rate of approximately 8 $km/year$ is reported, suggesting no asymmetries between winter and summer seasons (*Eisenman*, 2010). The Canadian Ice Service Digital Archive (CISDA) is another source of data that allow for the investigation of long-term variability of sea ice conditions within the Canadian Arctic (*Tivy et al.*, 2011). The CISDA dataset provides summer sea ice coverage for all Canadian Arctic regions since 1968. Based on the CISDA dataset, average summer sea ice cover in the CAA has decreased by $2.9\% \pm 1.2\%$ $decade^{-1}$ (Figure 2.6a) and the decreasing trends are approximately 3 to 17 % $decade^{-1}$ depending on the regions for 1968 to 2010 (*Derksen et al.*, 2012).

The sea ice extent time series for the CAA show considerable interannual variability and are unique compared to that of other regions in the Arctic. As of 2010, the record low sea ice extent for the Arctic Basin for the satellite era (since 1979) is year 2007 (*Stroeve et al.*, 2007), but that for the CAA is year 1998. Since the 1960s, sea ice depletion has also occurred in years 1962, 1971, 1976, and 1984, 1998, 2007 and 2008. 2007 is the first time in the satellite era for the clearing of the Northwest Passage route through the western Parry Channel. Subsequent low ice years also occurred in 2008 and 2010. Despite these low ice years, MYI continues to be transported southward from the Queen Elizabeth Islands

(QEI) into the Northwest Passage.

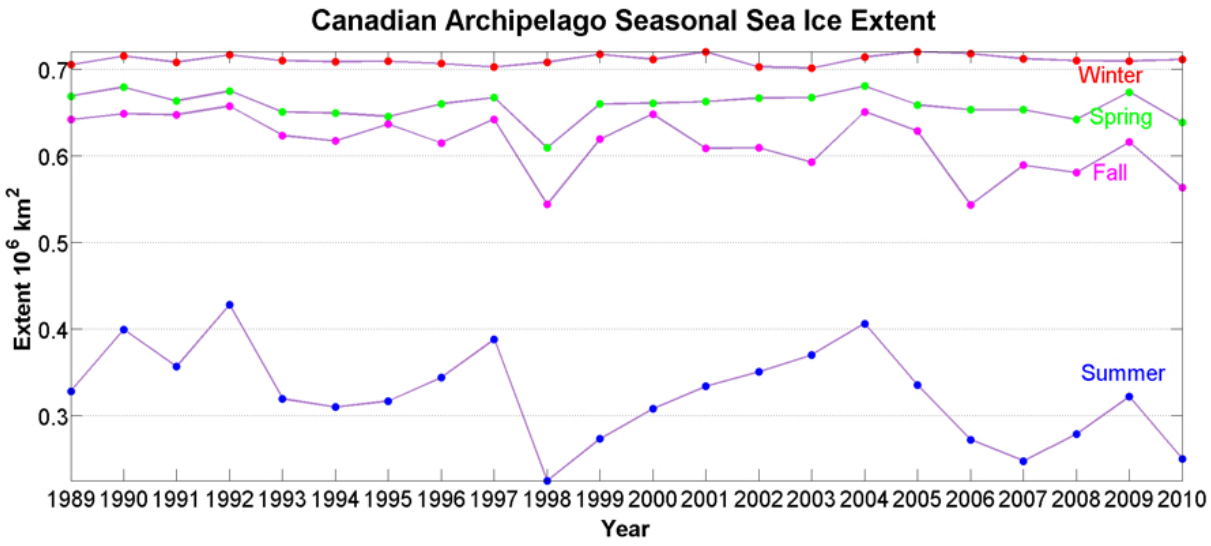

(a) Seasonal sea ice extent variation

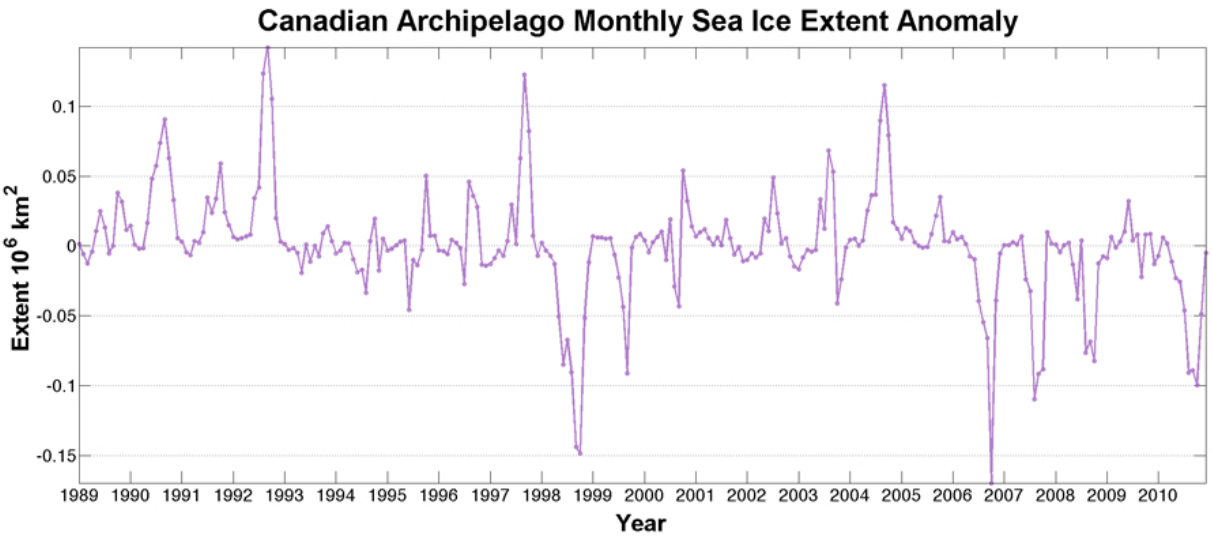

(b) Monthly sea ice extent anomaly

Figure 2.5: (a) Seasonal sea ice extent for the CAA in Winter(JFM), Spring(AMJ), Summer(JAS) and Fall(OND); (b) Monthly sea ice extent anomaly for CAA from 1989 to 2010. Passive microwave SIC data using NASA team algorithm is used in this figure.

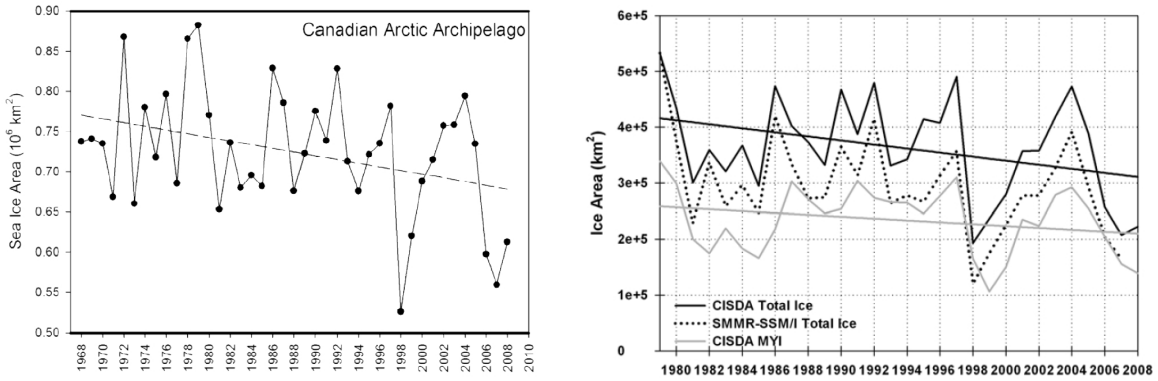

(a) (b)

Figure 2.6: (a) Time series of summer ice coverage for the CAA region from 1968 to 2008. The downward trend is 2.9% ± 1.2% $decade^{-1}$. Adapted from *Tivy et al.* (2011). (b) Time series of average monthly September total ice and multi-year ice area determined from the CISDA within the CAA region, 1979 - 2008. The time series of average monthly September total ice area determined from the SMMR-SSM/I sea ice dataset within the CAA region, 1979 - 2007 is also shown. Adapted from *Howell et al.* (2009).

Ice of the CAA region is a mix of MYI and FYI types and is mostly landfast ice during winter. *Howell et al.* (2008b) summarized the changing MYI conditions using Canadian Ice Services ice charts and concluded that MYI forms within the western and northern parts of the CAA and slowly migrates southeast. For summer MYI area in the CAA from 1968 to 2008, only the Foxe Basin exhibited significant decreases of 20% $decade^{-1}$ (*Tivy et al.*, 2011). Average September total sea ice area and MYI area are decreasing at 8.7% $decade^{-1}$ and 6.4% $decade^{-1}$ in the CAA from 1979 to 2008 (*Howell et al.*, 2009) (Figure 2.6b).

2.2.3 Sea Ice Drift between CAA and the Arctic Ocean, and Atlantic Ocean

Sea ice freezeup begins in October and ice consolidates by mid to late winter in the CAA (*Canadian Ice Service*, 2011). Ice plugs that connect the channels along the northwest

margin of the CAA form in October. Landfast ice occupies the Sverdrup Basin from October-November until late July in next summer. Pathways through the Sverdrup Basin are blocked by late November, and Parry Channel freezes up and is blocked by ice between mid-November and mid-January (*Melling*, 2012). These ice plugs block the further movement of ice to the south (*Marko*, 1977). In the summer, the ice plugs collapse progressively toward the interior of the basin and melt through the formation of shore leads (*Melling*, 2002). However, not all ice plugs disintegrate in summer. Ice in some areas remains landfast for many years in succession. The plug of multiyear fast ice in Sverdrup Channel is known to have cleared only in 1962, 1977, 1978 (probably), and 1998, and that in Nansen Sound only in 1962, 1971, and 1998. Thus, 1962 and 1998 are the only two years that both the Nansen Sound and Sverdrup Channel multi-year fast ice plugs fractured and became mobile based on the record from 1961 to 2010 (*Jeffers et al.*, 2001). The plug in Peary Channel clears more frequently, and Prince Gustaf Adolf Sea ice plug opens most frequently (*Melling*, 2002). Factors that control the opening of the ice plugs on an interannual scale are not understood.

Since all channels are blocked by landfast ice for several months each year, sea ice movement in the CAA region is seasonal. Ice becomes mobile in most areas in the CAA in late summer until mid-July and mid-August. The clearing of the ice plugs enables the southward movement of ice from the Sverdrup through Hell Gate, Cardigan Strait, Penny Strait and Byam Martin Channel to southern Viscount Melville Sound, M'Clintock Channel and Peel Sound and Lancaster Sound. These southeast movement of sea ice is generally attributed to a drop in sea level of 0.1-0.3 m across the Canadian Archipelago to Baffin Bay (*Muench*, 1971). The ice drift speed typically 5-30 cm/s depending on the geographic location and the strength of the currents in these channels.

Roughly 480 $km^3/year$ of ice volume moves through the Archipelago, which is about 20% of the ice volume that exports through Fram Strait from the Arctic Ocean (*Melling et al.*, 2012). At present, observations are too sparse to permit accurate estimation of ice fluxes through Canadian waters. Sea ice flux between the CAA and Arctic Ocean in winter months has been investigated by *Kwok* (2006) and *Agnew et al.* (2008), using RADARSAT and AMSR-E imagery, respectively. A net annual export of sea ice from the CAA into the Arctic Ocean based upon analysis of RADARSAT imagery for the period of 1997 to

2002 was confirmed by both studies. The months of study for *Agnew et al.* (2008) were September to June in the following year and no estimates for July and August was made due to atmospheric attenuation of the microwave signal in the bands used. Event-driven weather systems moving through the CAA cause daily fluxes between the CAA and Arctic Ocean as large as 2500 km^2 import or export (*Agnew et al.*, 2008).

Compared to the winter season, summer ice motion is much smaller and measurements have much larger uncertainty. *Alt et al.* (2006) documented the import and export of old ice through the Peary and Sverdrup Channels following the record low ice cover in 1998. The largest sea ice export from the Sverdrup Basin (SB) into the Arctic Ocean over the 1997 to 2002 period was September 1998 (*Kwok*, 2006). This ice export extreme explains about one-third of the observed ice-free area in the Sverdrup Basin region during that time period. Southward ice drifts through the Prince Gustaf Adolf Sea are approximately 1-2% of the wind speed in 2010 mobile-ice season (*Wohlleben et al.*, 2012). Using the Canadian Ice Services Automated Sea Ice Tracking System (CIS-ASITS) with RADARSAT imagery, Sea ice import/export between the Arctic Ocean and the CAA is quantified during the months of May to November for the period of 1997 to 2012 (*Howell et al.*, 2013). The M'Clure Strait had a mean flux of $+5\times\ 10^3\ km^2$ from May to September and a mean flux of $-7\times\ 10^3\ km^2$ from October to November (Positive and negative flux signs correspond to Arctic Ocean ice inflow and outflow, respectively). The QEI gates had a mean flux of $+4\times\ 10^3\ km^2$ from August to September with negligible ice exchange from May to July and October to November. The amount of MYI dynamically imported within the CAA in the summer was also estimated by taking the difference between MYI area on the last week of September from MYI area on April 1st using MYI area extracted from the CISDA (*Howell et al.*, 2009). MYI import calculated by this method can only be considered as the lower bound about how much MYI entered the CAA region, because during spring and summer, MYI within the CAA may melt or export through Amundsen, Jones Sound and/or Lancaster Sound. Due to the fact that different datasets and different methods were used in those two studies, sea ice area import/export calculated by *Howell et al.* (2009) and *Howell et al.* (2013) are quite inconsistent.

Because of the lower SIC and thinner sea ice in recent years, sea ice horizontal movement induced by winds and ocean currents is stronger than in previous periods (*Spreen*

et al., 2011, *Rampal et al.*, 2011). Increased sea ice mobility is in part responsible for the weaker decreasing trend of sea ice extent in the CAA relative to other Arctic regions. The replenishment of sea ice in the CAA from 1998 to 2004 is attributed to the import and through-flow of old ice through the Peary and Sverdrup Channels and through Gusttaf Adolf Sea (*Howell et al.*, 2008a).

2.2.4 Melt/Freeze Onset and Melt/Freezing Duration

Because of the difference in dielectric properties of snow, ice and water, surface emissivity changes drastically when liquid water forms between ice and snow. Passive microwave brightness temperature is a function of surface emissivity and several techniques have been developed to detect the melt season duration, melt onset, and freeze-up dates for the Arctic using passive microwave brightness temperature at different frequencies and polarizations (*Anderson and Drobot*, 2001, *Belchansky et al.*, 2004, *Stroeve et al.*, 2006). A most recent melt onset and freeze up dataset is the one by *Markus et al.* (2009) from 1979 to 2009. In order to provide melt onset data with better spatial resolution, *Howell et al.* (2006) developed a melt onset algorithm using SeaWinds/QuikSCAT data for the CAA region for the time period of 2000 to 2007. The timing of melt onset and pond onset was detected for a small study area of the CAA at daily to weekly time-scales and at a spatial scales that are on the order of hundreds of metres using synthetic aperture radar (SAR) images over the period of 1992 to 2002 (*Yackel et al.*, 2007).

Both the later start of freeze-up and the earlier start of melting led to longer melt period throughout the years and contributed to the severe sea ice loss in recent years. Based upon analysis of passive microwave data, *Markus et al.* (2009) showed that the average sea ice melt onset date in the CAA is year day (YD) 161.2, with standard deviation of 4.9 days and a 2.3 *days/year* trend toward earlier melt from 1979 to 2007. The melt season duration, which is the duration from melt onset to freeze onset, increased significantly at 7 *days/decade* (*Howell et al.*, 2009). Even though the end-of-summer sea ice extent are quite different for different regions of Arctic, the timing for melt onset for all regions inside the Arctic circle are quite close, as shown in Figure 6 of *Markus et al.* (2009).

2.2.5 Factors Controlling Sea Ice Extent in the CAA

Lesins et al. (2012) reported that the warming trend averaged over all the Canadian Arctic stations from 1971 to 2010 is 0.69 °C ± 0.13 °C $decade^{-1}$, using measurements from 22 Canadian radiosonde stations (Figure 2.7). The surface temperature trend in the CAA is an amplification ranged from 1.4 to 5.2 relative to the global average warming trend of 0.17 °C $decade^{-1}$. *Tivy et al.* (2011) concluded that the increases in spring air temperature explain up to 58% of the inter-annual variability of the the long-term summer sea ice decreases in the CAA, with air temperature leading by approximately 4 to 5 months. They further suggest that strong winter ENSO with positive Surface Air Temperature (SAT) anomalies cause decreasing FYI that allows for increased MYI import. *Polyakov et al.* (2012a) demonstrated that the Canadian Basin experienced an exceptional warming in the 2000s using Arctic Ocean temperature observations of the intermediate (depth range of 150 to 900 m) Atlantic Water (AW) of the Arctic Ocean collected from 1950 to 2011. The lack of significant decreases in MYI within the CAA has been attributed to increased dynamic MYI import from the Arctic Ocean that replaces ice lost due to melt (*Howell et al.*, 2009).

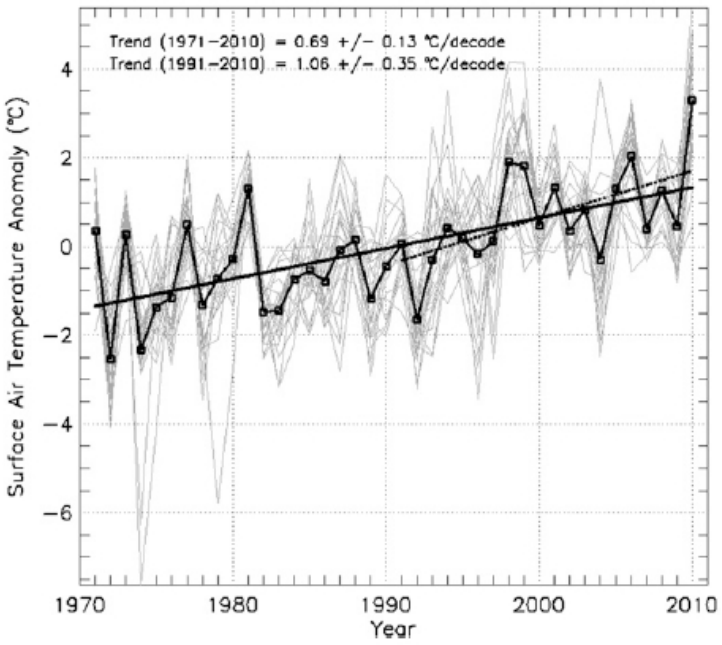

Figure 2.7: The annually averaged surface air temperature anomaly time series for each of the 22 Canadian radiosonde station is shown in gray from 1971 to 2010. The heavy black annual curve is the average over all 22 stations. The reference period for the anomaly calculation is 1971 2010. The thick black solid line is the linear fit from 1971 to 2010, while the thick black dotted line is the linear fit from 1991 to 2010. Adapted from *Lesins et al.* (2012).

The extreme anomaly year of 1998 has been investigated in several papers (*Jeffers et al.*, 2001, *Atkinson et al.*, 2006) and compared with year 2007 (*Howell et al.*, 2010). The 1998 minimum has been attributed partly to the warmer than normal summer air temperature (*Jeffers et al.*, 2001). However, *Melling* (2002) pointed out that, during the years of 1971, 1976, and 1984 with dramatically depleted MYI, the air temperature anomalies within the Canadian Arctic tundra zone were small. The long melt season along with unusual atmospheric circulation that prevented MYI replenishment was responsible for the anomalous low ice coverage in 1998. The mechanism responsible for the 2007 clearing of the Northwest Passage route was prior thinning of the MYI, followed by rapid melt, and most importantly, an atmospheric circulation pattern that prevented MYI from

the Queen Elizabeth Islands (QEI) from entering the Western Parry Channel (*Howell et al.*, 2009).

Based on the time series of MYI in the CAA region from 1968 to 2006, a low MYI year was always followed by a period of recovery that lasted up to six years. For example, the 1998 summer minimum was followed by a sea ice replenish went from 2000 to 2004. A MYI recovery mechanism was proposed by *Howell et al.* (2008b). There are three sources of MYI for the CAA: (1) the in situ FYI promoted to MYI after surviving at least one summer melt; (2) the import of MYI from the Arctic Ocean via M'clure strait; and (3) MYI southward flow from QEI. When seasonal FYI melts in the CAA region, ocean currents and wind transport MYI southeastward from the Western Parry Channel, with M'Clintock Channel and Franklin regions acting as a drain-trap for MYI (*Howell et al.*, 2008a). However, this ice movement can only occur when a route of ice-free water is available. When all of the routes are covered by MYI, little MYI can be further accumulated, preventing the transport of ice from the Arctic Ocean to the CAA. This drain-trap mechanism helped to recover the MYI in the CAA gradually over a five to six years period.

2.2.6 Sea Ice Melt Processes in the CAA

Fetterer and Untersteiner (1998) characterize the stages of Arctic sea ice spring and summer melt as early melt, melt onset, and advanced melt. The current understanding of these stages in the CAA region is summarized as follows:

1. In each spring, due to the decreasing wintertime continental polar air and reduced frequency of Arctic inversion, large scale synoptic conditions with frequent invasion of maritime polar air masses and increased cloud cover determine the timing of the early melt in the CAA (*Agnew and Silis*, 1995).

2. The next stage is melt onset, which is denoted by a rapid decrease of sea ice concentration. As free water content increases, the imaginary part of the dielectric constant becomes larger, leading to the rise of passive microwave emissivity (*Fetterer and Untersteiner*, 1998).

3. Pond onset or flooding on the sea ice surface from melting of the snow cover on the sea ice follows melt onset. The physical processes influencing the formation and evolution of melt ponds on sea ice during the Arctic summer is reviewed by *Fetterer and Untersteiner* (1998). The fractional extent of melt pond increases during early summer. As summer progresses, melt pond coverage begin to decrease in late July and this stage is pond drainage (*Perovich and Polashenski*, 2012). The mechanisms of sea ice melt pond formation and evolution on melting first year, landfast Arctic sea ice have been described in detail by *Polashenski et al.* (2012).

2.3 Summary and Future Directions

In this chapter, background knowledge about passive microwave remote sensing of sea ice has been reviewed. The current trend and variability of sea ice in the CAA region have been summarized. The sea ice extent decline trend in the CAA is not as significant as other Arctic regions. The MYI extent shows no significant trend. Ice dynamic import from the Arctic Ocean is one of the possible reasons for the less severe decline of sea ice in the CAA region. There seems to be a decadal cycle for the extreme ice loss in the CAA, but the mechanisms for this cycle are not fully understood. An important step in improving the understanding of sea ice thermodynamics and dynamics is to examine each spring and summer in detail. The knowledge of sea ice retreat processes in the CAA will benefit future sea ice prediction.

Chapter 3

Data Description

In this chapter, datasets used in this thesis are described. Three datasets are used: NASA Team daily sea ice concentration data from passive microwave sensors, MODIS ice surface temperature, and surface radiation data from ERA (ECMWF reanalysis)-interim project. Considering the fact that ERA-interim only starts from 1989, this study has been confined to the 22-year period from 1989 to 2010.

3.1 Sea Ice Concentration Data

A summary of the sea ice concentration datasets is given in the previous chapter. The NASA Team SIC dataset is the most widely used dataset for calculating the sea ice extent and sea ice area, because of its consistency through the years and between different generations of satellites (*Parkinson and Cavalieri*, 2008). The NASA Team dataset is also selected in this work. Daily and monthly Arctic SIC data have been archived by the National Snow and Ice Data Center (NSIDC) since October 1978. Ice concentrations are mapped to Equal-Area Scalable Earth Grid (EASE-Grid). The EASE-Grid is overlaid on a north polar stereographic projection with a grid cell size of 25 by 25 km^2 in Northern Hemisphere (NSIDC, 1992).

The NASA Team SIC algorithm is detailed in *Cavalieri et al.* (1984). A summary of

this algorithm is provided here. 19.4-GHz horizontally (H) and vertically (V) polarized channels and the vertically polarized 37.0-GHz channel, are used in the NASA Team SIC algorithm. Two independent variables, the polarization (PR) and spectral gradient ratios (GR), are defined using these three SSM/I channels:

$$PR = [TB(19V) - TB(19H)]/[TB(19V) + TB(19H)] \tag{3.1a}$$

$$GR = [TB(37V) - TB(19V)]/[TB(37V) + TB(19V)] \tag{3.1b}$$

where TB is the observed brightness temperature at the indicated frequency and polarization. From these two parameters, the first-year ice concentration (CF) and the multiyear ice concentration (CM) are calculated using the following equations:

$$CF = (a_0 + a_1 PR + a_2 GR + a_3 PR * GR)/D \tag{3.2a}$$

$$CM = (b_0 + b_1 PR + b_2 GR + b_3 PR * GR)/D \tag{3.2b}$$

$$where D = c_0 + c_1 PR + C_2 GR + c_3 PR * GR \tag{3.2c}$$

The total ice concentration (CT) is the sum of the first-year and multiyear concentrations

$$CT = CF + CM \tag{3.3}$$

The coefficients a_i, b_i, and c_i $(i = 0, 1, 2, 3)$ are calculated based on the TBs of nine tie points.

Considering that the accuracy of SIC in the summer when melt ponds are present is about $\pm 15\%$ (*Cavalieri*, 1992), the SIC data in the spring and summer seasons are not as reliable as they are in the winter season (*Cavalieri*, 1992). Compared to Canadian Ice Service digital charts, the sea ice data used here underestimate ice coverage between -7.1% and -32.6% during shoulder seasons (*Agnew and Howell*, 2003).

3.2 MODIS Ice Surface Temperature Data

Other than microwave sensors that are commonly used to map sea ice concentration and extent, multispectral radiometers can measure sea ice surface temperature in addition to

sea ice concentration/extent during clear sky conditions (*Hall et al.*, 2004). The Moderate-Resolution Imaging Spectroradiometer (MODIS) satellite data were used to derive SIC maps (*Drüe and Heinemann*, 2004). The algorithm firstly retrieves SIC from the satellite-sensed surface temperature, then the retrieves from multiple satellite overpasses within one day are combined. The accuracy of MODIS SIC data was evaluated in *Drüe and Heinemann* (2005) and found to have an error of approximately $\pm 10\%$.

MODIS reflectance data were originally considered for the current research, but several preprocessing steps are required to map the swath data into gridded products. The preprocessing steps include reprojection, mosaicing and cloud/land masking. This preprocessing is beyond the scope of the current study. Thus, MODIS Terra products (MOD29E) available at 4-km resolution are used to further understand the sea ice retreat process in the CAA. MOD29E1 is a daily global ice extent and ice surface temperature (IST) product at 4 km resolution. Before sea ice detection, clouds, land and inland water bodies are masked with the MODIS cloud and geolocation products. Sea ice detection is achieved if a pixel passes a grouped criterion test which include:

- normalized difference snow index (NDSI), (band 4 - band 6) / (band 4 + band 6) greater than 0.4;
- visible reflectance (band 2) greater than 0.11;
- near-infrared reflectance (band 1) greater than 0.10.

Ice surface temperature (IST) is calculated with a split-window technique using MODIS brightness temperatures at bands 31 and 32, which correspond to 11 and 12 um channels. Brightness temperatures are converted from radiance data. A detailed description of this product is provided in the MODIS Snow Products User Guide (*Riggs et al.*, 2006). The MODIS ice extent and IST data are downloaded from the NSIDC website (`http://nsidc.org/data/mod29e1d.html`).

To facilitate the visual interpretation of the IST data, we categorize the IST values from all cloud-free ocean pixels into several categories. The freezing point of fresh water is $273.15K$. Sea ice is saline and $271.5K$ is often used as the temperature for sea ice to

freeze (*Hall et al.*, 2004). These two temperature values are used to develop sea ice surface temperature maps. Several additional points are also introduced to differentiate very cold ice area, different level of ice melt, and open water area. Thus, six categories are used with the colors defined in Table 3.1:

1. Pixels with IST less than $270K$ representing cold ice.
2. Pixels with IST between $270K$ and $271.5K$ representing ice approaching melt.
3. Pixels with IST between $271.5K$ and $272.5K$ representing early melt.
4. Pixels with IST between $272.5K$ and $273.15K$ representing further melt.
5. Pixels with IST between $273.15K$ and $275K$ representing melt pond.
6. Pixels with IST larger than $275K$ representing open water.

Table 3.1: Color scheme for daily IST maps

feature	color	temperature (K)
land	light gray	
cloud	dark gray	
ice	white	<270
ice that close to melt	red	[270 271.5]
early melt	green	(271.5 272.5]
further melt	yellow	(272.5 273.15]
Ponding	cyan	(273.15 275]
open water	blue	>275

The accuracy of satellite derived IST algorithm has been assessed by several authors (*Key et al.*, 1994, *Scambos et al.*, 2006, *Hall et al.*, 2008, 2012) and generally has a bias of less than 1 K. However, none of these validations were done under spring and summer sea ice melt conditions.

3.3 Atmospheric Reanalysis Data and ERA-Interim

Observation data are quite scarce in the Arctic. Reanalysis data provide a coherent record of global atmospheric circulation. Reanalysis data are not only physically coherent, but they also incorporates observations using data assimilation. ERA-interim reanalysis project is a state of the art global atmospheric reanalysis produced by the European Centre for Medium-Range Weather Forecasts (ECMWF) (*Dee and Uppala*, 2009). This project is an improvement from ERA-40 reanalysis and the data are freely available for research. ERA-interim reanalysis covers the data-rich period since 1989 at a resolution of 0.75°. An automatic bias correction system is included in the data assimilation system to automatically handle changes in the observation system and the bias in models and observations (*Dee and Uppala*, 2009). ERA-interim not only provides superior spatial and temporal resolution in comparison to in situ observations alone, but also benefits from the assimilation of satellite data and the physical constraints of the model. ERA-Interim daily fields are freely available on the ECMWF Data Server at a 1.5° resolution and are used for this study.

The surface meteorological data, such as temperature, pressure, wind speed and direction are from analyses of the data assimilation scheme, but radiative flux data are produced through forecast. The shortwave radiation scheme takes into account boundary conditions provided by the surface scheme, such as albedo. For the albedo of oceanic grid-boxes, SIC is treated explicitly using SMMR-SSM/I passive microwave measurements, even though the ice concentration is simply set to 100% north of 82.5°N (*Simmons et al.*, 2007). The albedo of sea ice is assigned using monthly values based on *Ebert and Curry* (1993) that has a crude seasonal cycle and that is held constant from year-to-year (*Screen and Simmonds*, 2012). The longwave radiation scheme mainly depends on surface and air temperature (*Dee and Uppala*, 2009). The validation and evaluation of the ERA-interim is in its early stages. The ERA-40 surface downward shortwave radiation agrees well with observations in the Arctic and shows negligible long term bias (*Liu et al.*, 2005). There are no large differences between ERA-40 and ECMWF incident shortwave radiation (*Perovich et al.*, 2007b). Compared to flux tower observations, ERA-interim tends to overestimate the monthly variability of incoming shortwave radiation at the surface with a bias of approxi-

mately 25 w/m^2 and a root mean square error of 30 w/m^2 (*Decker et al.*, 2012).

Chapter 4

Sea Ice Retreat Processes in the CAA: 1989 to 2010

4.1 Introduction

Sea ice in the CAA has undergone significant changes in a variety of aspects in recent years. Compared to the period from 1998 to 2004, the longer melt season along with reduced ice import for the period of 2005 to 2010 drive the recent summer minimum sea ice extent in the CAA region (*Howell et al.*, 2010). However, the physical processes that explain how sea ice is changing on daily to weekly scales need more investigation. In this analysis, we make use of the passive microwave satellite record of daily Arctic sea ice concentration (SIC) data to investigate the sea ice retreat process in the CAA region in detail. In this study we (1) provide a detailed investigation into the sea ice retreat process for spring and summer; (2) discuss the possible mechanism for the sea ice retreat process.

4.2 Data and Methodology

In this study we are mainly interested in the processes that govern the sea ice retreat in the CAA region. The study area for this chapter is shown in Figure 4.1. Since the minimum

sea ice extent in the CAA occurs in late September and after that sea ice starts to grow, this study will focus on sea ice decay months (from April to September) because we are mostly interested in the ice retreat process that drives the September minimum. Daily SIC data are used to derive the sea ice spring and summer retreat pattern. MODIS ice surface temperature data are used to help identify the features described based on SIC data.

Daily SIC data from April 1 (YD91) to September 30 (YD273) for the 22-year period from 1989 to 2010 are used. April 1st is considered as YD91 even in leap years for simplicity. Daily sea ice extent (SIE) is the sum of the grid cells in the CAA region that each has an ice extent greater than 15%. Region definition follows that of *Parkinson and Cavalieri* (2008). The monthly sea ice extent is the mean sea ice extent for all the days in that month. The monthly (daily) sea ice extent anomaly is calculated by subtracting the monthly (daily) mean value for the 22-year from the monthly (daily) value of that month (day). Daily sea ice extent change (ΔSIE) is the SIE difference for two successive days. Thus, positive daily ΔSIE means that the SIE has increased from the day before, while negative daily ΔSIE means that the SIE has decreased from the day before. The climatology of the daily ΔSIE, defined as the average ΔSIE of that day for the 22-year period study (1989 - 2010), is also calculated.

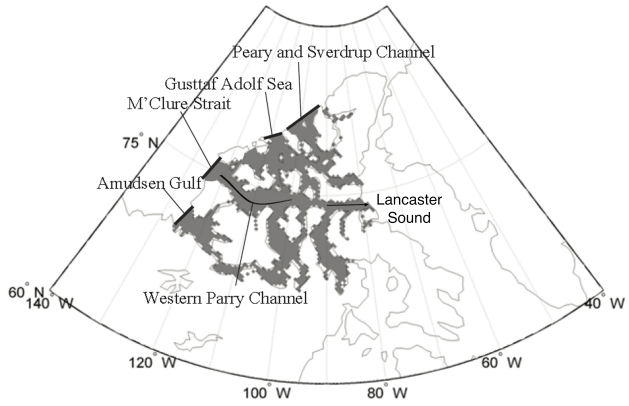

Figure 4.1: The study area (Canadian Arctic Archipelago) shown in grey on the map. Region definition follows that of *Parkinson and Cavalieri* (2008).

In this study, we are comparing the seasonal progression of the difference in sea ice extent on sequential days and between different years, while the absolute values of sea ice extent are not used. Though the accuracy of SIC data is relatively lower in Spring and Summer compared to in Winter, the use of daily sea ice change instead of the absolute value may eliminate the systematic bias in the SIC data to a large extent.

4.3 Results

4.3.1 Interannual Variation of Sea Ice Extent in CAA

The year-to-year changes in sea ice extent for the spring-summer season in the CAA region is shown from 1989 to 2010 in Figure 4.2a. Total sea ice extent gradually decreases from a maximum of a little more than 0.7×10^6 km^2 on April 1st in all the years to a smaller extent ranging from 0.10×10^6 km^2 in 1998 to 0.46×10^6 km^2 in 1992 on September 30th. Because of the land constraint, the CAA region is nearly fully ice covered at the start of the melt season and little interannual sea ice variability is observed at this time of the year. However, the SIE at end of melt season varies significantly for different years. Thus, the minimum SIE for each year depends mainly on how much the ice decreases in extent during the spring and summer months through dynamic and thermodynamic processes. The yearly sea ice loss for the six-month period (April to September) each year is shown in Figure 4.3, ranging from 0.25 to 0.62 $\times$ $10^6 km^2$. The monthly sea ice loss anomaly illustrates that the sea ice anomalies from April to September are most significant in recent years (Figure 4.2b). For the purposes of this study, we define the years with yearly ice loss one standard deviation from the mean as extreme years. On the basis of this criterion, the extreme years with large and small ice loss are reported in Table 4.1. The years with high summer SIE (small ice loss) are 1992, 1997 and 2004. The years with low summer SIE (large ice loss) are 1998, 1999, 2006 and 2010. These extreme years before 2008 are generally consistent with the yearly minimum SIE in the CAA region reported by *Parkinson and Cavalieri* (2008) using NASA Team monthly SIC data. The minimum summer SIE for the CAA in 2007 and 2008 are lower than that of 2006, but these two years are not listed as extreme years based on the current definition. This is likely the result of

large MYI import at the end of September after the summer minimum SIE in 2007 and 2008.

Table 4.1: Years from 1989 to 2010 with large ice loss and small ice loss

	Larger than 1 S.D. (Small ice years)	Smaller than 1 S.D. (Large ice years)
Total ice loss from April to August Year (extent: 10^3 km^2)	1998(625), 1999(533), 2006 (510), 2010 (518)	1992(255), 1997(266), 2004 (264)

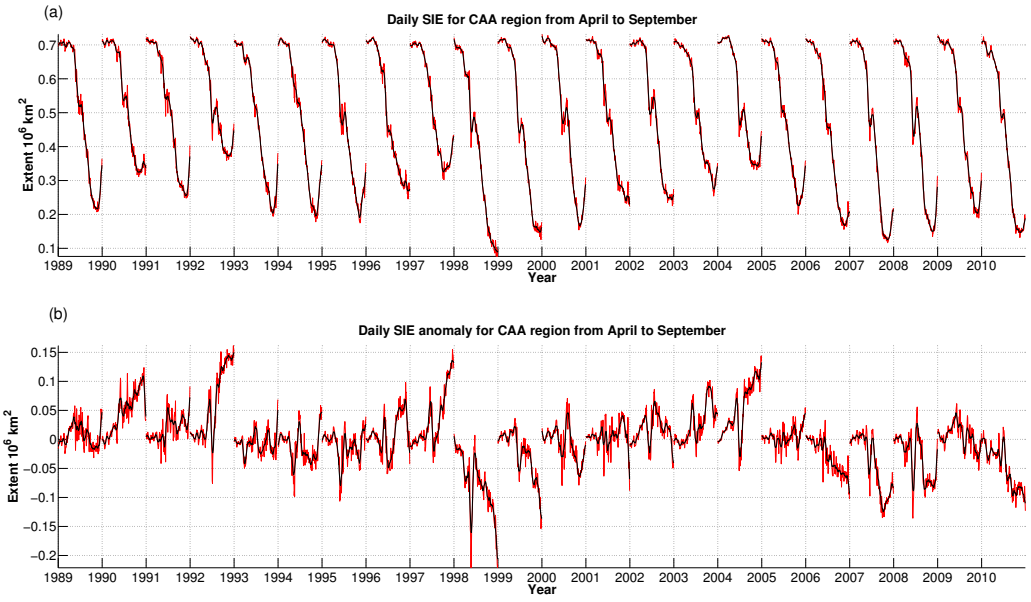

Figure 4.2: (a) Time series of daily sea ice extent from April to September for each year (1989 to 2010). The thick line is the 5-day running mean of the daily sea ice extent. (b) Monthly Sea Ice loss anomaly for each year.

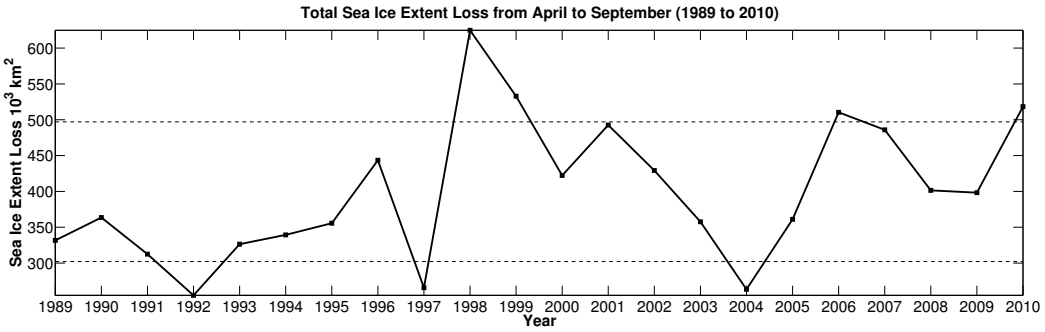

Figure 4.3: Time series of total ice loss from April to September for each year from 1989 to 2010, and the dashed line is the one standard deviation envelope. Years with large and small ice loss are listed in Table 4.1

4.3.2 Climatological Mean of Daily ΔSIE

Daily ΔSIE distribution exhibit large variations from day-to-day and from year-to-year, as shown in Figure 4.4a for each year. The mean and median daily ΔSIE are -3.1 $\times$ 10^3 km^2 and -1.6 $\times$ 10^3 km^2 for April to August for the 22-year period. Daily ΔSIE has large fluctuations with a range from -67 to 57 $\times$ 10^3 km^2 and a standard deviation of 11 $\times$ 10^3 km^2. The extreme cases with large daily ΔSIC are quite significant, with the daily change being close to 10% of the water area of CAA. The climatological means of daily ΔSIE time series for 1989 - 2010 also exhibit large day-to-day variations (Figure 4.4b). Thus, the 5-day running mean of the daily ΔSIE is calculated and used in the following analysis. The 5-day running mean not only eliminates the large fluctuations in daily sea ice extent change data but also retains the major daily ΔSIE patterns.

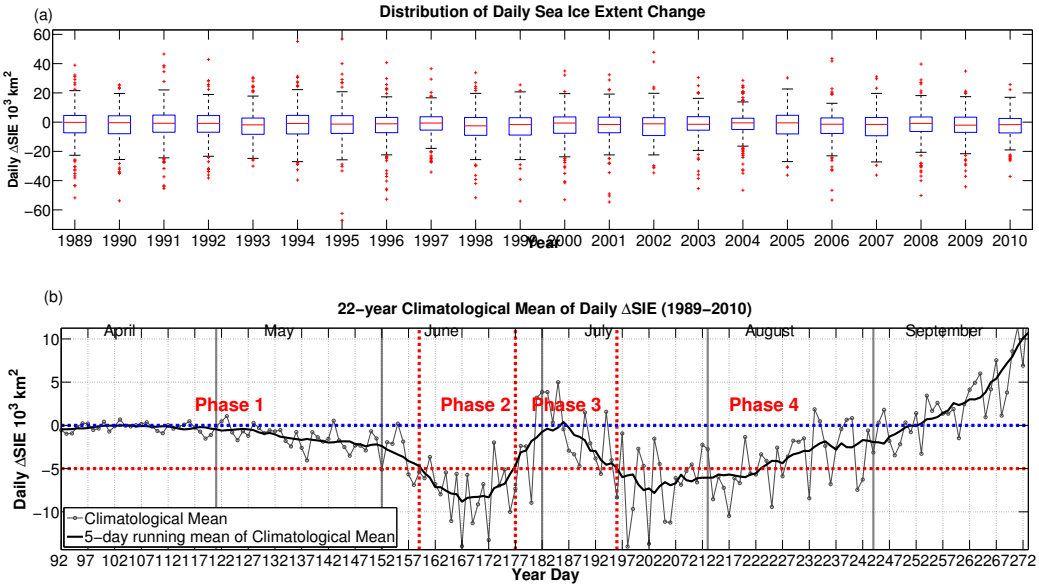

Figure 4.4: (a) Yearly box plots of daily ΔSIE from 1989 to 2010. Each box plot shows the 5th, 25th, 50th, 75th and 95th percentiles values. The outliers are plotted (red dots) individually. Thus, half of the values fall within the range indicated by the box, 90% of the values fall within the range indicated by the vertical lines, and the median value is the horizontal line near the middle of the box. (b) Climatological mean of the daily ΔSIE for 1989-2010. Solid gray and black lines represent the daily and 5-day running mean of ΔSIE, respectively. Dashed vertical lines indicate the division of phases, and solid vertical lines indicate different months. The dashed horizontal lines represent ice loss of 0 and 5000 km^2/day.

The ice retreat in the CAA starts from the Amundsen Gulf and Lancaster Sound, and then generally follows the latitudinal distribution from southern area to northern area. Ice advection in August and September also influences the ice retreat. Thus, the temporal evolution of the daily sea ice change pattern in the CAA is a combined result of several different factors, including geographic settings of the area, the ocean current, and the ice-albedo feedback. Based on the values of daily ΔSIE, we categorize the sea ice retreat

process in the CAA region into four sequential phases (Figure 4.4b): (1) Small daily sea ice variation before melt onset; (2) Large daily sea ice loss; (3) Very small daily sea ice loss or even some daily sea ice increase; (4) Steady sea ice loss until the end of summer with gradually decreasing sea ice loss rate. The criteria used to define each phase are as follows: Phase 1 lasts until the magnitude of the daily SIE loss is continuously larger than 5×10^3 km^2/day. Phase 2 includes the days after phase 1 having the magnitude of daily SIE loss continuously larger than 5×10^3 km^2/day. Phase 3 begins when the magnitude of daily SIE loss drops to less than 5×10^3 km^2/day until again the magnitude of daily SIE loss become larger than 5×10^3 km^2/day. The days after phase 3 are defined as phase 4.

The start of phase 1 is arbitrarily set as April 1st in this discussion. The climatological mean of the start day of other phases are reported in Table 4.2, and the corresponding mean SIC maps are shown in Figure 4.5. Daily ΔSIE features a slow loss in April, and then some days with accelerated loss speed, then a few days with slow decrease or even a small ice increase, and then large loss again. Phase 1 often lasts until late May or early June with daily SIE loss being less than 5×10^3 km^2 with small variance. From inspection of the climatological mean at the start of each phase (Figure 4.5b), it is evident that sea ice extent loss in phase 1 are mainly in Amundsen Gulf and Lancaster Sound. After phase 1, phase 2 begins and is characterized by increasing rates of ice loss with large daily SIE loss (the magnitude of daily ice loss larger than 5×10^3 km^2/day). This large daily loss persists for a few days and then ramps down. The ice loss in phase 2 are mainly due to melt in the inner channels of the CAA (Figure 4.5c). Phase 3 includes the days with small ice loss or even some ice increase (the magnitude of daily ice loss is less than 5×10^3 km^2/day). This phase lasts one to two weeks for the observational period. In the middle of summer when air temperature is above zero in the CAA (*Lindsay*, 1998), it is impossible for in situ ice growth. Two possible reasons might be responsible for the small daily SIE loss and even some periods of ice increase in phase 3, ice influx from the Arctic Ocean to the CAA by atmospheric and oceanographic forcing that cancels out the ice melt, or the artifact of microwave signature during ice melt. These factors will be examined further in the following sections.

Table 4.2: The end day and length of each sea ice change phase (see text for the meaning of offset and R)

Year	Phase1	Phase2	Phase3	Length of Phase 2	Length of Phase 3	Offset	R
1989	157	176	190	19	14	-3	0.33
1990	164	178	193	14	15	9	0.29
1991	160	169	188	9	19	4	0.32
1992	167	184	203	17	19	7	0.37
1993	157	174	186	17	12	-2	0.41
1994	140	156	167	16	11	-5	0.35
1995	152	169	188	17	19	-2	0.33
1996	167	183	194	16	11	7	0.27
1997	177	190	198	13	8	-4	0.32
1998	**152**	**164**	**182**	12	18	-9	0.32
1999	160	178	194	18	16	4	0.43
2000	154	177	196	23	19	3	0.44
2001	159	181	196	22	15	-4	0.27
2002	156	175	195	19	20	-1	0.41
2003	167	181	194	14	13	2	0.33
2004	**167**	**183**	**203**	15	20	8	0.39
2005	159	174	199	15	25	-6	0.36
2006	154	180	193	16	13	3	0.33
2007	159	174	189	15	15	-3	0.49
2008	159	174	191	15	17	-2	0.52
2009	159	178	192	19	14	1	0.41
2010	160	173	186	13	13	-3	0.47
Climatological mean	159	177	196	18	19		
Yearly ΔSIE>S.D.	158	175	192	17	17		
Yearly ΔSIE<S.D.	167	184	202	17	18		

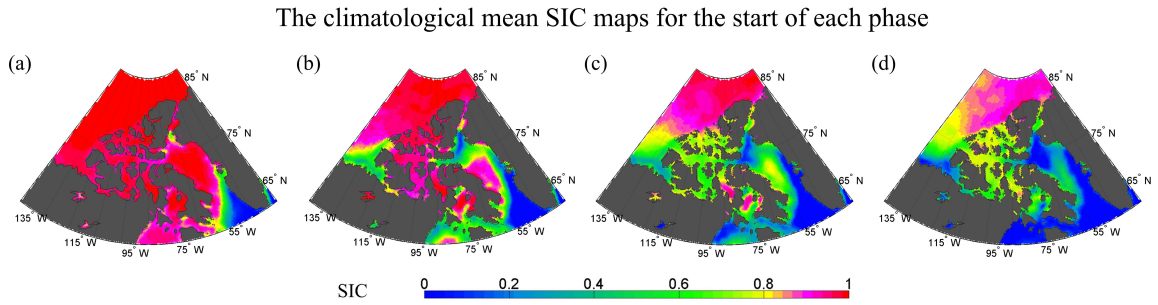

Figure 4.5: The climatological mean SIC maps for the start of (a) phase 1, (b) phase 2, (c) phase 3 and (d) phase 4.

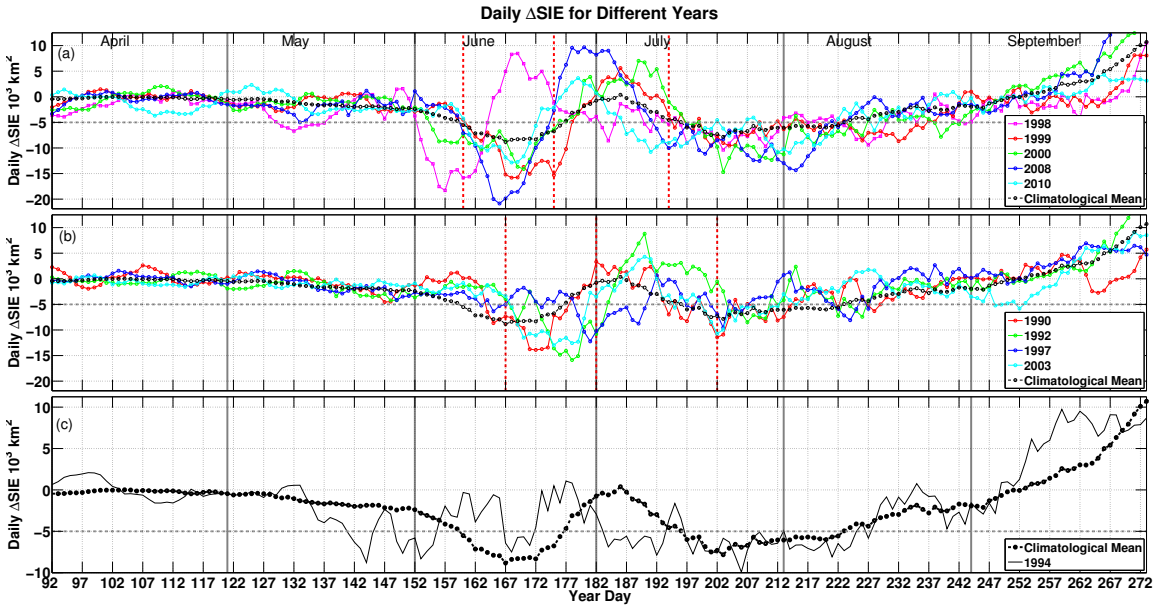

Figure 4.6: The amount of daily ΔSIE for CAA (a) for high ice extent years, (b) for low ice extent years, (c) for 1994. The climatological mean shown in black is used as a reference line in each panel for comparison. Red dashed horizontal line (5000 km^2/day ice loss) is the threshold used to divide different phases. Grey vertical lines demonstrate different months.

4.3.3 Interannual Variations of Daily ΔSIE

In this section we analyze the daily ΔSIE time series for different years, focusing particularly on the high ice years and low ice years in Table 4.1. The four-phase pattern is obvious for most of the years from 1989 to 2010 (Figure 4.6). The climatological mean, shown in black in each panel, serves as the reference for comparison between different years. The proposed pattern is also evident upon close inspection of Figure 4.2a for most years. Year 1994 is a notable exception to the proposed four-phase pattern with several ice decrease and increase phases, but none of the ice loss periods lasted long enough to cause large areas of melt (Figure 4.6c). Thus, year 1994 is an outlier in the scatterplots of Figure 4.8 and is not considered in the following discussion of the early/late start of phase 2. However, the day with the first large sea ice decrease is used as the start of phase 2 in 1994 in Table 4.2. The daily ΔSIE time series for different years have several common features:

1. Daily ΔSIE time series in different years follow the same pattern with less than two weeks offset between different years (Figure 4.6).

2. Years with large sea ice loss (Figure 4.6a) begin phase 2 earlier than those in years with small sea ice loss (Figure 4.6b). The start day of each phase is reported in Table 4.2 and plotted in Figure 4.7, ranging from YD152 to YD167 with a two-week variation. For the observed time period discussed in this chapter, year 1998 that has the largest ice loss in the CAA region is the earliest to start phase 2, 3 and 4, while year 2004 that has the smallest ice loss is the latest to start phase 2, 3 and 4, as shown in bold in Table 4.2.

3. The climatological length of phase 2 and 3 are both close to 18 days. Years that begin phase 2 early transit to phase 3 early, and vice versa. This indicates that the early start of the quick melt phase (phase 2) does not lead to the lengthening of that phase. Phase 2 typically lasts close to two weeks, and phase 3 lasts approximately another two weeks.

4. Years with large daily sea ice loss in phase 2 are generally followed by large sea ice increase in phase 3. We could see this symmetric pattern in both large ice loss years,

such as 1998, 2007 and 2008 (-18 to -8$\times$ 10^3 km^2/day), and in small ice loss years, such as year 1992, 1996 and 2004 (-8 to -3 $\times$ 10^3 km^2/day).

To quantify the offset for each year's ΔSIE from the climatological mean, the cross correlation coefficient between each year's daily ΔSIE time series and the climatological mean is calculated for lags from -15 days to 15 days. The lag at which the cross correlation coefficient is largest is considered as the offset between that year and the climatological mean. For each year, both the offset and the corresponding largest correlation are reported as the last two columns in Table 4.2. Negative offset means an earlier start of phase 2 compared to the climatological mean, while positive offset means later start of phase 2 compared to the climatological mean. The correlation coefficient between the lags time series and the start day of phase 2 time series is 0.43 at 95% confidence intervals. Considering the large day-to-day fluctuations of the sea ice extent change time series of six months each year, these moderate correlations suggest that there might be related but as yet undetermined physical processes.

To examine the effect of yearly sea ice loss and the timing of each phase, we plot the yearly sea ice loss and the start days of phase 2 and 3 (Figure 4.8a and 4.8b). The years with large sea ice loss are in the lower right corner of the plot, indicating earlier inception of phase 2 and phase 3 in these years; while years with small sea ice loss are in the upper left corner, indicating later inception of phase 2 and phase 3 in these years. This pattern leads to the significant observation that the start date of phase 2 can be used as a key factor to determine the amount of ice melt for a season.

To test whether the daily ΔSIE is significantly different between different phases for all the years, the nonparametric Kolmogorov-Smirnov (K-S) test is used (*Gregory*, 1963). This test is suitable for an ordinal sample with a non-normal distribution, which is the case for the daily ΔSIE data. Based on the definition of the four phases, all daily ΔSIE are divided into four groups. The K-S test is then used to test if the daily ΔSIE from any of the two phases (i.e., phase 2 and phase 3) are significantly different. The null hypotheses are that the daily ΔSIE from two different phases are from the same distribution. The null hypotheses are all rejected at the 0.99 level for any combination of the two phases (Table 4.3). The rejection of the hypothesis means that there are significant differences for

daily ΔSIE between any of the two phases from the four phase group, which confirms that our criteria used to define different phases are reasonable. The cumulative distribution functions of different phase groups are shown in Figure 4.9. The daily ΔSIE in phase 3 is generally smaller than that of phase 2.

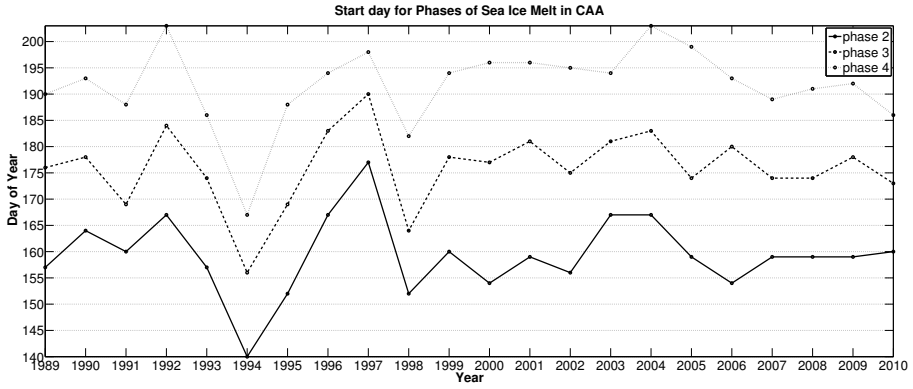

Figure 4.7: (a) Time series of the dates of the start day of phase 2, 3 and 4.

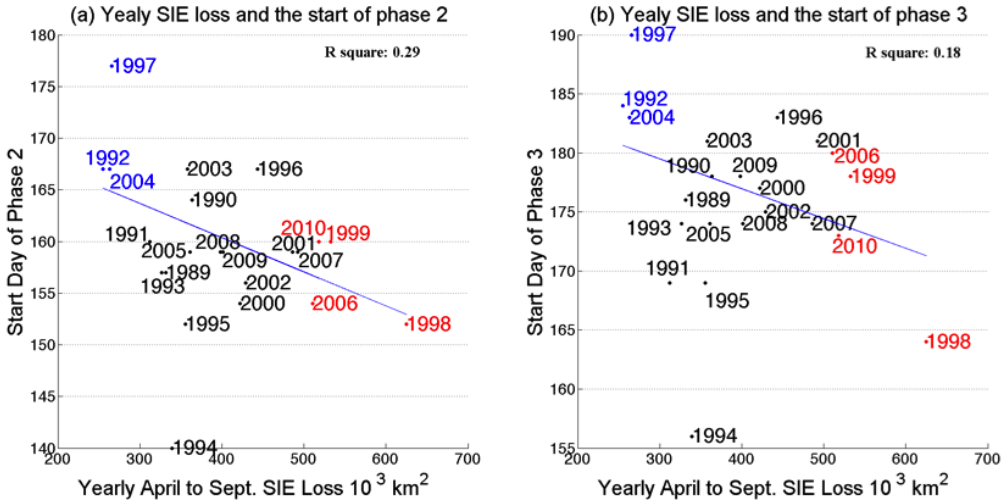

Figure 4.8: Scatterplots of (a) the start day of phase 2, (b) the start day of phase 3 versus yearly sea ice extent loss from 1989 to 2010. Years with large and small ice loss identified in Table 4.1 are shown in different colors, respectively.

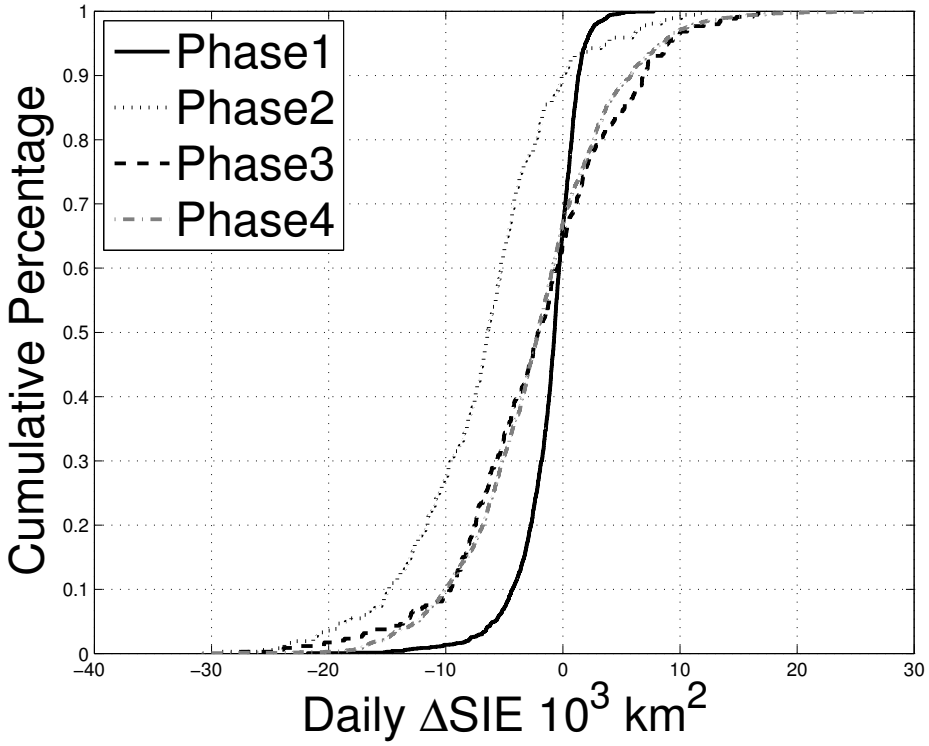

Figure 4.9: Cumulative distribution function of daily ΔSIE for different phases.

Table 4.3: Two sample Kolmogorov-Smirnov statistic for daily ΔSIE between two phases are from different distributions.

	Phase 2	Phase 3	Phase 4
Phase 1	0.61	0.28	0.45
Phase 2		0.34	0.19
Phase 3			0.22

4.3.4 Physical Processes for Sea Ice Retreat in CAA

We take a close look at three extreme years, 1998, 2004 and 2007, to examine the details of the four phase ice retreat process in the CAA. These three years had remarkably different ice coverages. The daily sea ice extent and daily sea ice extent change time series for these three years are shown in Figure 4.10. The climatological mean for the 1989 to 2010 interval is also plotted as a reference. Year 1998 has daily ΔSIE larger than that for any other years, with the result being that the total areal extent is well below the climatological mean from early April. The start days of phase 2 are YD152 and YD159 for 1998 and 2007, and YD158 for the 1989 - 2010 climatological mean. The start days of phase 2 as defined here are similar to the melt onset dates reported by *Howell et al.* (2010). They report that the average date of melt onset from 1979 to 1996 within the CAA occurred on YD153. Melt onset for 1998 was YD146, whereas for 2007 it was YD155. Both results indicate that the start of melt in 1998 is a week earlier than that of the climatological mean.

The SIC maps for the start day of phase 2, 3 and 4 are shown in Figure 4.11 for these three years. At the start of phase 2, the CAA region is generally fully ice covered, as shown as red areas on the maps (Figure 4.11a, d, g). At the start of phase 3, the large areas appear as green in the CAA, indicating the decrease of sea ice concentration in phase 2. (Figure 4.11b, e, h). Moreover, the gate of M'Clure Strait facing the Arctic Ocean is open. At the start of phase 4, quite large areas in the Western Parry Channel and the area south of it appear as a mixture of red and green, indicating a sea ice concentration increase in these areas based on the sea ice concentration data we used (Figure 4.11c, f, i).

Based on the characteristics of daily ΔSIE time series described in the previous section, physical processes that govern the sea ice retreat in the CAA are discussed. In April and May, the ice in the CAA is quite stable (Figure 4.4b), and the melt is slow. Since net radiation turns positive in early April (*Lindsay*, 1998), considerable energy begins to accumulate. The melt accelerates at some point in early June, and becomes quite dramatic due to the enhanced ice-albedo feedback as the sea ice is broken into small pieces (*Perovich*, 2005). In phase 3, there are consistent sea ice increases for most of the years used in this study. Since continuous in situ ice growth for a few days is not likely to occur in the middle of summer each year, we suspect that there are two possible reasons for the increase of SIC

in phase 3, one is ice import from other regions, the other is related to passive microwave signature of sea ice during melt. According to Canadian Ice Service weekly ice charts, the ice in the channels of the CAA is still landfast during the proposed phase 2 and phase 3 in the three years discussed here. For example, phase 3 begins from June 13th in 1998, but ice in the Western Parry Channel is still landfast at that time and cannot allow for ice import. Thus, the ice increase in phase 3 cannot be ice import from other regions. The ice only becomes mobile in late summer based on the ice chart. Thus, the ice increase in phase 3 needs further investigation.

To understand the nature of the artifact, we note that at the end of phase 2, SIC for a large part of the CAA drops close to 0.5 (Figure 4.11), which means each pixel is composed by 50% sea ice and 50% open water. Considering the fact that passive microwave cannot differentiate melt pond from open water, the open water that appears in phase 2 is more likely to be melt ponds on sea ice. Figure 4.12 and Figure 4.13 show the 8-day-composite melt pond fraction maps during the proposed phase 2 and 3. These maps were produced by *Rösel et al.* (2012) for the period from 2000 to 2011 and no melt pond fraction map is available for 1998. The largest pond coverage occurred on June 30 composite for 2004, and on June 23 composite for 2007. Based on our analysis, the start of phase 3 was July 2nd in 2004 and June 24 in 2007. Thus, the start of phase 3 occurred at same time when the melt pond coverage was at the maximum. Moreover, the maximum pond coverage was about 50% in each pixel based on the melt pond coverage maps. Thus, we infer that the quick decrease of sea ice in phase 2 is not real. Because melt ponds appear radiometrically similar to open water (*Fetterer and Untersteiner*, 1998), melt ponds are treated as open water in the retrieve of sea ice concentration from the passive microwave data. Thus, sea ice concentration is underestimated in phase 2. At the end of phase 2, the melt pond coverage has reached its maximum. In phase 3, the ice extent appears to be increasing based on the passive microwave sea ice product. This is caused by pond drainage. Once the melt ponds drain, sea ice is re-exposed from the cover of melt pond, leading to slow ice decrease or even some ice increase in phase 3. Since phase 2 and phase 3 each last up to 18 days and the earlier start of phase 2 does not prolong the length of phase 2, we can infer that it takes close to two weeks from melt onset to the largest melt pond fraction, and another two weeks for melt pond drainage. After that, the ice melt rate is stable until

the end of summer.

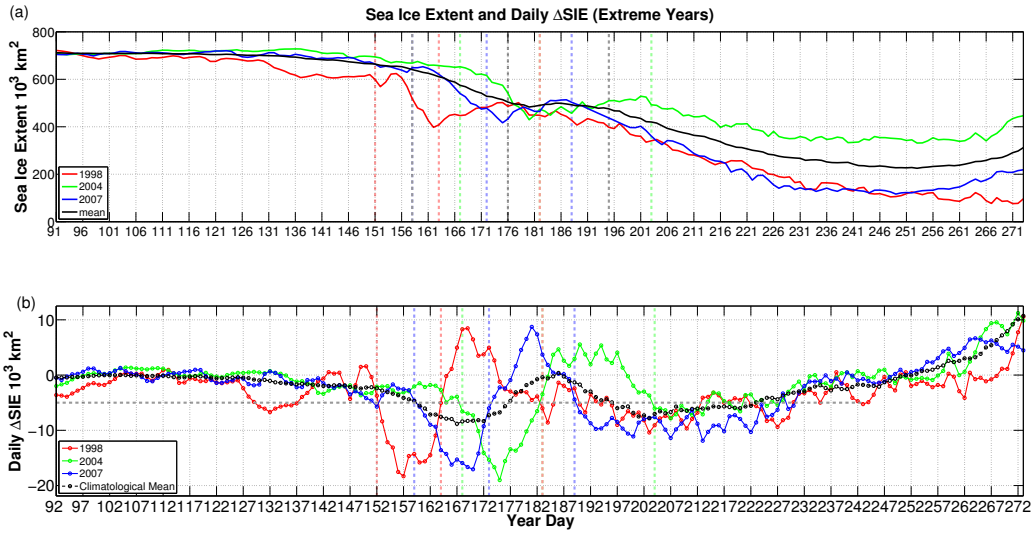

Figure 4.10: Time series of (a) sea ice extent and (b) daily ΔSIE for CAA in recent extreme years, from April 1 (YD 91) to September 30 (YD272) for the climatological mean of 1989-2010 (black), 1998 (red), 2004 (green) and 2007 (blue). Vertical dashed lines are the divisions for different phases for the years in the corresponding color.

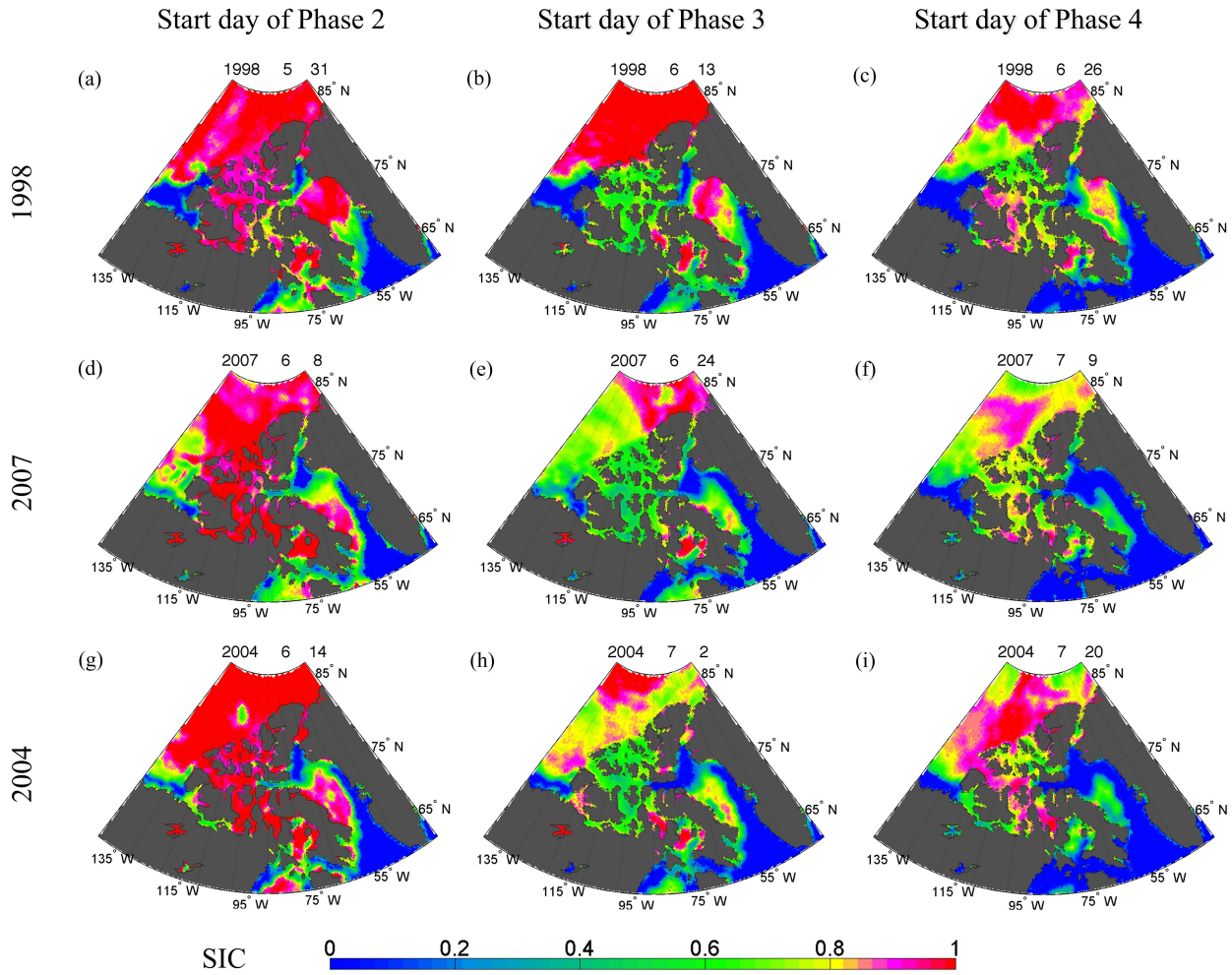

Figure 4.11: Maps showing sea ice concentration (SIC) for year 1998 (row 1), 2007 (row 2) and 2004 (row 3) at the end day of Phase 1 (column 1), Phase 2 (column 2) and Phase 3 (column 3), respectively.

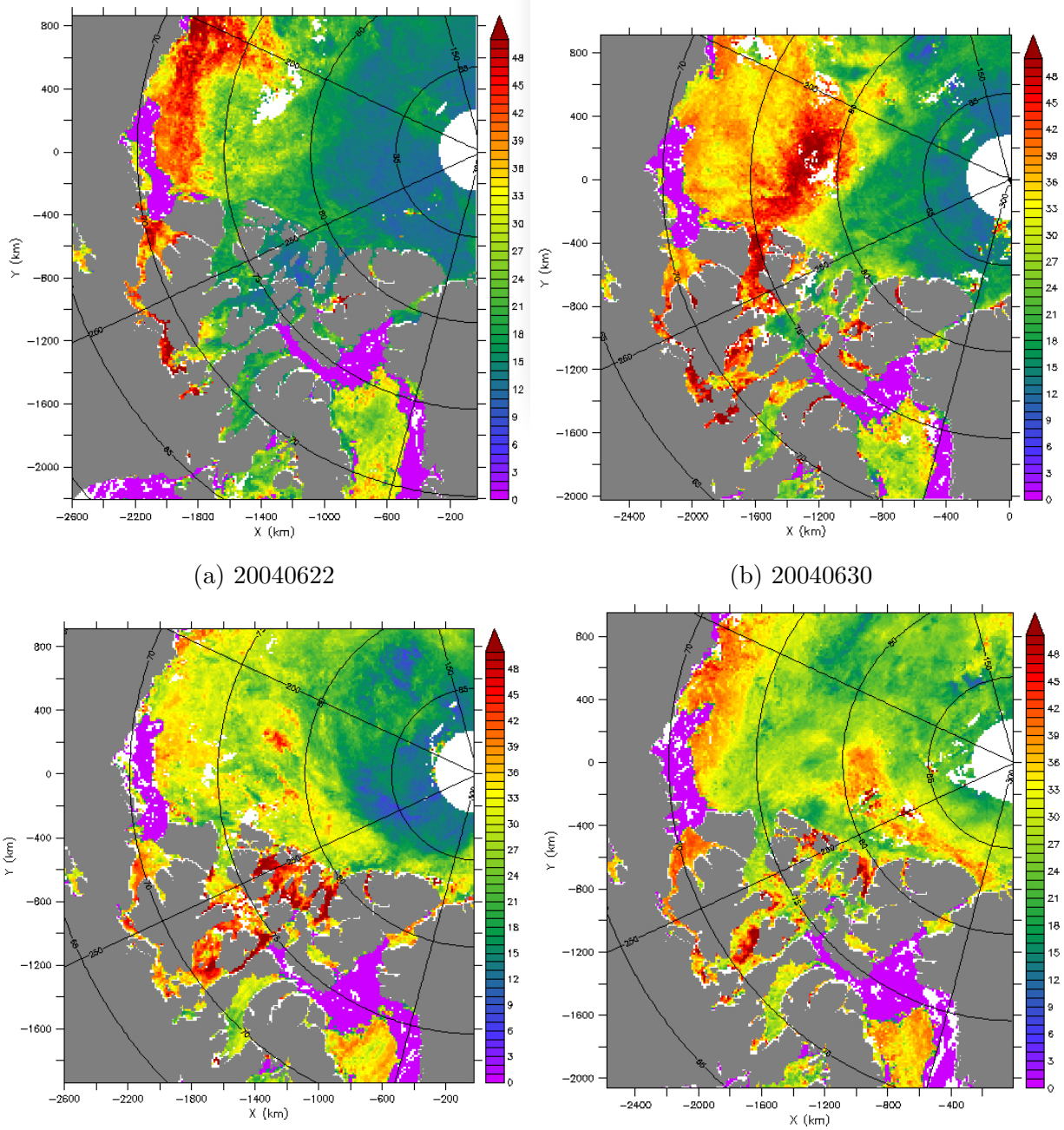

(a) 20040622

(b) 20040630

(c) 20040708

(d) 20040716

Figure 4.12: 8-day composite melt pond fraction maps calculated using MODIS data for selected days in summer 2004, with the largest pond coverage occurred on the June 30 composite (*Rösel et al.*, 2012).

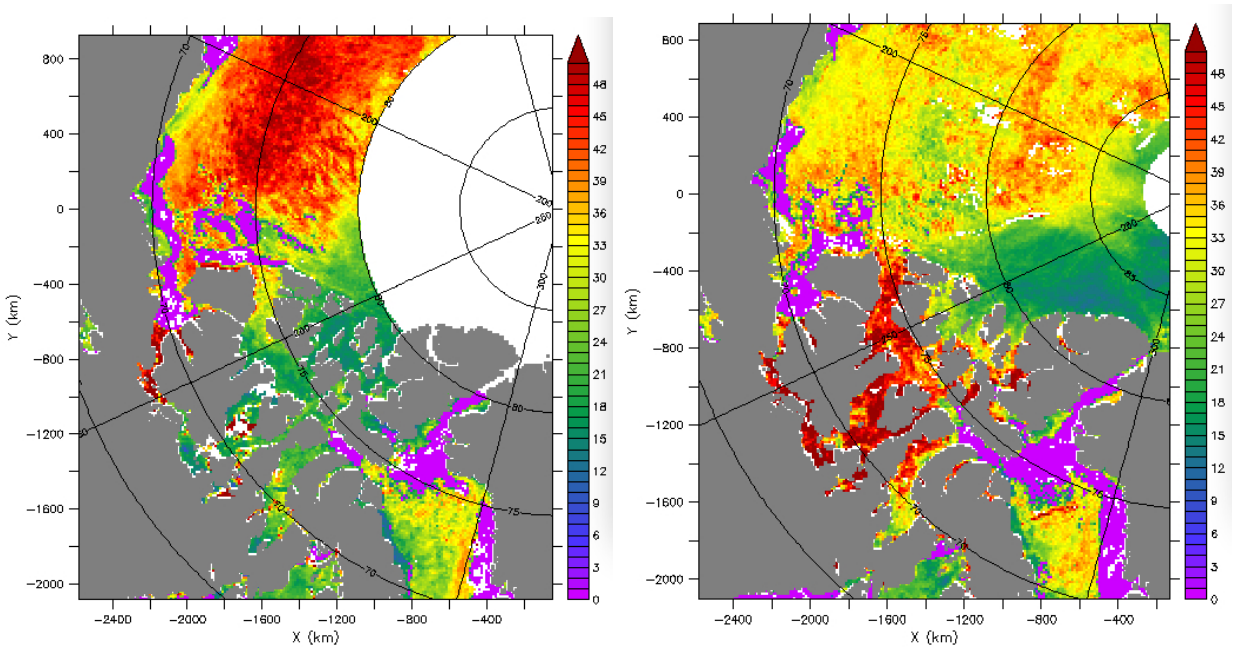

(a) 20070615

(b) 20070623

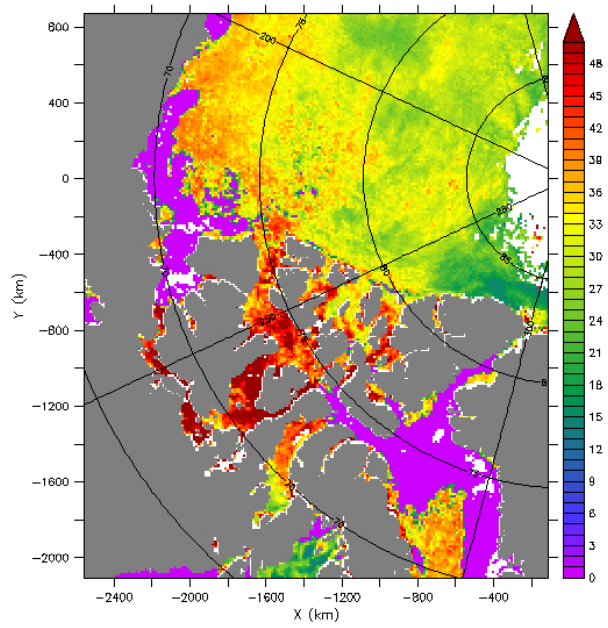

(c) 20070701

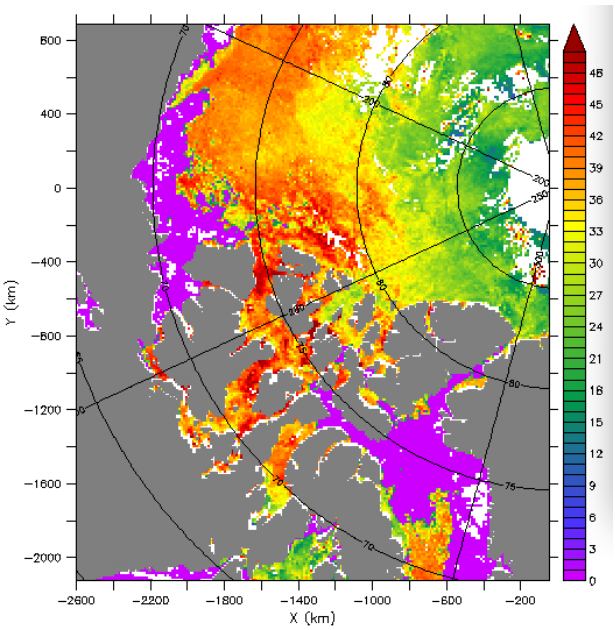

(d) 20070709

Figure 4.13: 8-day composite melt pond fraction maps calculated using MODIS data for selected days in summer 2007, with the largest pond coverage occurred on the June 23 composite (*Rösel et al.*, 2012).

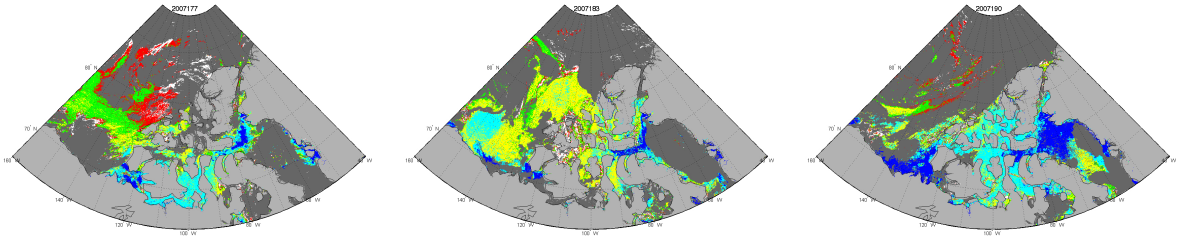

(a) June 26 (b) July 2 (c) July 9

Figure 4.14: Terra MODIS ice surface temperature maps for three days in 2007. Different colors represent different IST values as defined in Table 3.1.

4.4 Validation with MODIS Daily Sea Ice Surface Temperature Data

The MODIS sea ice surface temperature (IST) is used to explain what is actually happening in the CAA region during phase 2 and phase 3 of the sea ice retreat. However, MODIS products are greatly affected by cloud cover. Only ocean pixels without cloud cover have valid ice surface temperature values. The summer of year 2007 was characterized as having unusually clear skies in the Arctic due to the persistent high atmospheric pressures over the central Arctic Ocean (*Kay et al.*, 2008). Thus, summer 2007 is selected in this study as relatively more valid IST data is available. Three daily IST maps from early, middle and late intervals of phase 3 are shown in Figure 4.14. These three days are selected because the CAA is largely cloud-free in these days. On June 26, 2007, which is the end of phase 2 and the beginning of phase 3 in the sea ice retreat, most of the pixels in the CAA region have IST values larger than 273.15 K (shown as cyan), representing melt pond. However, the IST values of these pixels are smaller than 273.15 K on July 2, shown as yellow and a few mixture of red and white, representing a mixture of ice and melt ponds. The CAA region turned into cyan again on July 9, meaning that extensive melt began in the region. These maps demonstrate that the melt pond coverage at the beginning of phase 3 is likely

high, but the melt pond coverage decreases as phase 3 progresses because of pond drainage. At the end of phase 3 and the beginning of phase 4, the ice melts more rapidly due to the high ice surface temperature.

4.5 Summary

Using daily SIC data from SSM/I for April to September each year from 1989 to 2010, we took a novel approach to the analysis of the sea ice retreat process in the spring and summer seasons in the CAA region on a daily scale by looking at daily change in sea ice cover. Previously, seasonal change often only has been inspected in the summer at monthly and yearly scales. Based on the total sea ice extent loss for the six-month period, large ice loss years and small ice loss years are defined. We analyzed the daily sea ice extent change (ΔSIE) for each individual year and found that the sea ice melt in the CAA can be defined as a four phase process: a slow ice melt phase that usually lasts until early June; a quick ice melt phase with large daily ΔSIE which lasts about half-a-month; a slow sea ice melt or even a small ice increase phase which lasts another half-a-month; and a steady ice decrease phase. The daily ΔSIE for different phases from all years are significantly different based on Kolmogorov-Smirnov (K-S) test, which confirmed that the proposed criteria to identify different phases are reasonable. The ice concentration maps also confirmed the proposed process. The four phase pattern occurred for most of the years from 1989 to 2010 and have several common characteristics:

1. Years with large sea ice loss begin phase 2 earlier than for years with small sea ice loss;

2. Years that begin an early phase 2 transit early to phase 3, and vise versa;

3. The length of phase 2 and phase 3 for different ice loss years are close to 18 days with little variation and are independent of the beginning date of phase 2;

4. Years with large daily sea ice loss in phase 2 are generally followed by large sea ice increase in phase 3.

The offset of each year's ΔSIE time series from the climatological mean is quantified by lagged correlation analysis. For a year, the offset indicates the number of days that phase 2 is advanced or postponed compared to the climatological mean. The start day of phase 2 is a good indicator of how much ice melts during that melt season. However, year 1994 is an exception with no obvious large ice decrease or increase phases.

Based on the common characteristics of the daily ΔSIE time series in different years, and with the assistance of MODIS melt pond fraction and ice surface temperature products, we conclude that the four-phase sea ice melt pattern is actually a ice slow-melt phase, a melt ponding phase, followed by a pond-drainage phase, and then breakup and further melt. The melt in April is slow but large amounts of net radiation are absorbed by the surface. Subsequently, melts accelerate at some point, with increased coverage of melt pond. The area of melt pond increases as ice continues to melt. In phase 2, the passive microwave sea ice concentration is underestimated because melt pond has been falsely identified as open water. In phase 3, melt ponds start to drain. The slow ice decrease and sometimes even some ice increase in phase 3 are mainly caused by melt pond drainage. This ice increase is not a physical mechanism but a result of the difficulty of passive microwave during ice melt. In phase 4, further melt of sea ice continues, with ice import from the Arctic Ocean in August and September.

In this chapter, we shed light on the sea ice retreat processes in the CAA. The proposed processes have been confirmed with MODIS melt pond fraction data and MODIS ice surface temperature data. Our findings could be of value for modelling sea ice-climate feedback on a regional level on daily and weekly scales. Understanding the detailed sea ice melt processes in the CAA region could also help the prediction of future clearing events, as ice information is important for navigation purposes. A logical extension of this work is to examine the types of synoptic patterns that trigger the early start of ice melt. Another avenue is to examine how MODIS products can be used to correct sea ice estimation during the melt season.

Chapter 5

Enhanced Arctic Sea Ice Concentration Estimation using MODIS Ice Surface Temperature and SSM/I Sea Ice Concentration

5.1 Introduction

Passive microwave sea ice concentration derived from the special sensor microwave/imager (SSM/I) is known to be of relatively low quality during the melt season, mainly because the emissivity and brightness temperature of the mixture of ice and melt pond are more similar to water than ice (*Cavalieri et al.*, 1990, *Eppler et al.*, 1992). In addition to ambiguities caused by the presence of melt ponds, during melt first year ice undergoes desalination and transforms to second-year ice. These two factors lead ice concentration retrieval algorithms to significantly underestimate the ice concentration during melt. For example, the NASA Team algorithm, which is used to calculate the sea ice concentration from passive microwave data, underestimates the total ice-covered area by 20.4% to 33.5% during ice melt in the summer when compared to the Canadian regional ice charts (*Agnew and Howell*, 2003).

Sea ice concentration estimates from passive microwave sensors can be improved by combining the passive microwave data with active microwave or radar data or other sources of information. Examples include, tuning the SSM/I ice concentration algorithm to ice concentration information from U.S. National Ice Center (NIC) ice charts (*Partington*, 2000), constraining SSM/I ice concentrations using Synthetic Aperture Radar (SAR) data (*Beaven and Gogineni*, 1998), and combining active and passive microwave imagery using a physical model for improved melt detection (*Ashcraft and Long*, 2006).

Sea ice concentration estimates from passive microwave data can also be improved upon by using data assimilation. Different techniques have been used to assimilate sea ice concentration (SIC) into numerical ice-ocean models, including the ensemble Kalman filter (EnKF) (*Lisæter et al.*, 2003), nudging (*Lindsay and Zhang*, 2006, *Wang et al.*, 2013), optimal interpolation (*Stark et al.*, 2008), and three-dimensional variational (3D-var) data assimilation (*Caya et al.*, 2010, *Buehner et al.*, 2013). These methods are found to lead to improved ice concentration analysis as compared with either the model or observations alone, but typically their performance is degraded during the melt season. The assimilation of passive microwave ice concentrations retrievals with static tie points cannot overcome the bias of the data during melt. Some improvement has been achieved during melt when brightness temperatures are assimilated directly using seasonally varying emissivity (*Scott et al.*, 2012). However, that method has not been extended to include multiyear ice. Reflectance data from the Moderate-Resolution Imaging Spectroradiometer (MODIS) have been found effective to retrieve the melt pond fraction during clear sky conditions (*Rösel et al.*, 2012, *Tschudi et al.*, 2008). A method to assimilate data from another visual infrared sensor, the Advanced Very High Resolution Radiometer (AVHRR) has been developed by *Scott et al.* (2013). The method was found to improve the representation of small scale details in the ice cover, but was not rigorously tested during melt.

The purpose of the present study is to investigate the potential improvement in SIC estimates from SSM/I through the assimilation of MODIS Terra ice surface temperature (IST) data. The IST measurement from MODIS represents the temperature at the ice/snow surface and has been used to infer melt conditions in previous studies (*Hall et al.*, 2009, 2013). The objective is that the proposed method could be used as a routine procedure to improve ice concentration estimation during the ice retreat season. The outline of this chapter is

as follows. The data used in the assimilation system are described and analyzed in Section 5.2. The data assimilation system is described in Section 5.3. Results are shown in Section 5.4, and in Section 5.5 conclusions and directions for future work are given.

5.2 Data and Study Area

The study area shown as the colored area in Figure 5.1a, includes the Canadian Arctic Archipelago (green), part of the Arctic Ocean (red) and part of Baffin Bay (blue). The daily sea ice concentration (SIC) data and MODIS ice surface temperature are used. MODIS products are greatly affected by cloud cover and only ocean pixels without cloud cover have valid ice surface temperature values. The summer of year 2007 was characterized as having unusually clear skies in the Arctic due to the persistent high atmospheric pressure over the central Arctic Ocean (*Kay et al.*, 2008). Thus, summer of 2007 is selected for this study because less cloud cover ensures more usable IST data. Based on the 8-day melt pond fraction maps, the composite of July 2nd has maximum melt pond coverage (*Rösel et al.*, 2012). Thus, data for July 2nd 2007 are shown here as an example. The SSM/I ice concentration map is shown in Figure 5.1b. The ice concentration map indicates that a large area in the central CAA is covered by ice of concentration 0.6. However, according to the weekly ice chart for July 2nd 2007 from Canadian Ice Service, most of the area in the CAA are still covered by landfast ice with ice concentration greater than 0.9. Thus, the ice concentration in the CAA is greatly underestimated by passive microwave data.

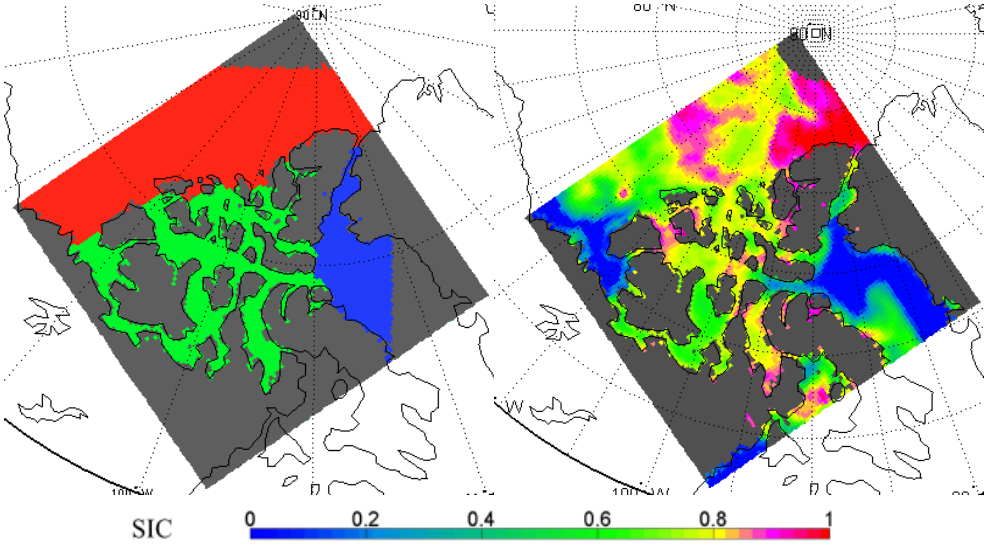

Figure 5.1: (a) Study area (b)Example of the SSM/I ice concentration (IC) map used in the assimilation, shown here is the IC map for July 2nd 2007.

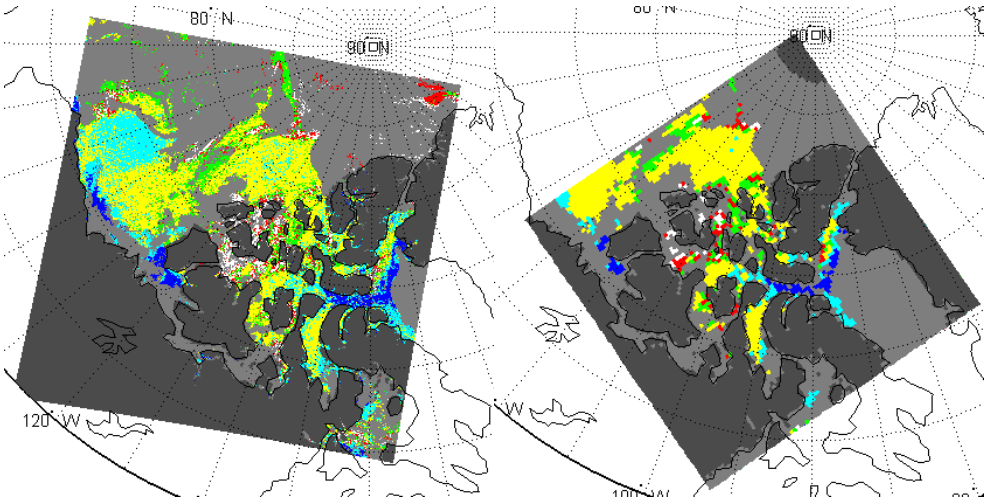

(a) IST in 4 km grid (b) IST in 25 km grid

Figure 5.2: Comparison between IST from (a) MODIS MOD29E1 and (b) IST on SSM/I grid with footprint operator applied. Data for July 2nd 2007 are shown as an example. Different colors represent different IST values as defined in Table 3.1.

The IST map for July 2nd 2007 is shown in Figure 5.2b. The color scheme used in the map is defined in Table 3.1. On this day, a large area of the Canadian Arctic was relatively cloud free. To facilitate the data assimilation, spatial resampling is used to represent the IST data on the same grid as the sea ice concentration data (Figure 5.2b). The footprint size of the SIC data (625 km^2) is significantly larger than the grid size of the IST data (16 km^2). A footprint operator is used to aggregate the IST to the SSM/I grid. This footprint operator averages the gridded IST over all grid points within a distance from the observation location equal to the footprint of the SIC data to simulate the spatial averaging effect of the actual satellite measurement. To calculate the IST for a grid point in SSM/I grid, the nearest grid point in the IST grid is found. All IST grid points that fall within a certain window centred on this nearest grid point are considered in the aggregation. According to the spatial resolution of both datasets, the area covered by 40 IST grid points approximately equals the area covered by one SSM/I grid point. As a window size of 5 by 5 is too small to cover the area of a SSM/I grid, it was decided to use to window size of 7 by 7. When at least 40 grid points in this window have valid IST values, meaning that at least 40 grid points are not land and not covered by cloud, the mean of all valid IST values in the window is used as the IST for the SSM/I grid point. Otherwise, the IST for the SSM/I grid point will be marked as cloud-covered. By comparing the IST map before and after spatial resampling, we can see that the spatial footprint works well to preserve the spatial distribution of IST (Figure 5.2).

5.3 Method

5.3.1 Data Assimilation System

Data assimilation is used in this study to combine MODIS ice surface temperature data with passive microwave sea ice concentration data to provide an optimal estimation of sea ice concentration. The data assimilation method used here is based on the variational data assimilation approach. A detailed description of this method is given in *Lorenc* (1986). Variational data assimilation methods seek to minimize a cost functional which measures the misfit between the model forecast and the observations. The cost function is defined

as,

$$J(\mathbf{x}) = \frac{1}{2}(\mathbf{x} - \mathbf{x_b})^T \mathbf{B^{-1}} (\mathbf{x} - \mathbf{x_b}) + \frac{1}{2}(\mathbf{y} - H(\mathbf{x}))^T \mathbf{R^{-1}} (\mathbf{y} - H(\mathbf{x})), \tag{5.1}$$

where $\mathbf{x}$ is the analysis state, which is the ice concentration will be determined, $\mathbf{x_b}$ is the background state of ice concentration (IC), $\mathbf{y}$ is the vector of observations that include ice surface temperature (IST) and passive microwave sea ice concentration, and H is the observation operator that maps the background ice concentration to the observation space. The background error covariance matrix is denoted as $\mathbf{B}$ and the observation error covariance matrix is denoted as $\mathbf{R}$.

The above cost function consists of two terms, one measures the difference between the analysis state $\mathbf{x}$ and the background state $\mathbf{x_b}$, weighted by the background error covariance matrix $\mathbf{B}$. The other measures the difference between the observation vector $\mathbf{y}$ and the model state mapped to the observation space $H(\mathbf{x})$, weighted by the observation error covariance matrix $\mathbf{R}$. The optimum state is referred to as the analysis and is denoted as $\boldsymbol{x_a}$. In this study, $\mathbf{B}$ is assumed to be diagonal, meaning that spatial correlations between neighbouring grid points are not considered. When $\mathbf{B}$ is diagonal, the analysis calculated by solving equation (5.1) is equal to that from the best linear unbiased estimator (BLUE) and leads to the following analysis equation,

$$\boldsymbol{x_a} = \boldsymbol{x_b} + \mathbf{K}(\boldsymbol{y} - H(\boldsymbol{x_b})) \tag{5.2}$$

Clearly, $\boldsymbol{x_a}$ is a weighted combination of the background state and the difference between the observation and the background state projected into the observation space, which is $\boldsymbol{y} - H(\boldsymbol{x_b})$. The weight given to each of these two terms is determined by the Kalman gain matrix $\mathbf{K}$,

$$\mathbf{K} = \mathbf{B}\mathbf{H}^T(\mathbf{H}\mathbf{B}\mathbf{H}^T + \mathbf{R})^{-1} \tag{5.3}$$

where $\mathbf{H}$ is the linearized observation operator, $\mathbf{H} = \partial\mathbf{H}/\partial\boldsymbol{x}$.

In this study, the estimated ice concentration state (analysis state) is a combination of the background sea ice state and two observations, passive microwave sea ice concentration and MODIS IST. The relative weights of the background state and the observations are determined by the relative errors in each of them, which are represented by $\mathbf{B}$ and $\mathbf{R}$. Usually a model is used to provide the background state for the data assimilation, but

in the current study the analysis from the previous day is used as the background state. A similarmethod was used in (*Buehner et al.*, 2013, *Scott et al.*, 2013). The background combines information from SSM/I ice concentration and MODIS IST, thus it has smaller error than the original SSM/I data. As SSM/I ice concentration data have uncertainties lager than 0.15 in the summer, the background ice concentration error standard deviation for each grid point is set as 0.15.

5.3.2 Forward Model and Observation Error

Both SSM/I ice concentration (IC) and MODIS IST are assimilated as observations. For the SSM/I IC, the forward model is a linear interpolation operator. For the MODIS IST, an empirical forward model has been developed to compute a predicted value of the observed ice surface temperature from the state vector, which is ice concentration. The model is based on the assumption that the observation within the satellite footprint can be expressed as a sum of contributions associated with the two classes: ice and water, weighted by their relative proportions visible to the sensor. The forward model is written as,

$$H(IC) = (1 - IC)y_{water} + ICy_{ice} \tag{5.4}$$

where y_{ice} and y_{water} are characteristic mean values of the ice surface temperature for ice and water. The mean and variance used for ice and water are estimated using all the cloud free ice pixels from June to August (Figure 5.3).

The distribution of IST for all grid points from June to August 2007 is shown in Figure 5.4a. The mean IST is 273 K and the standard deviation is 6.3 K. For pixels with a SIC larger than 0.5, IST is normally less than 273 K, while the IST for pixels having SIC smaller than 0.5 are generally larger than 273 K (Figure 5.4b). The mean and variance of IST for ice are set as the mean and variance of the IST for all ice pixels that have ice concentrations larger than 0.95. The mean and variance of IST for water are set as the mean and variance of the IST for all ice pixels that have ice concentrations smaller than 0.1. These values are reported in Table 5.1. The mean IST for ice is 271.3 K based on the IST data used in this study, which is close to the freezing point of sea water (-1.8$^{\circ}C$).

Compared to Canadian Ice Service ice concentration estimates, SIC estimation based on SSM/I data using the enhanced NASA Team algorithm underestimates total SIC by an average of 18% concentration percentage difference with a standard deviation of 17% (*Shokr and Markus*, 2006). Considering the large uncertainties of SIC with the SSM/I data during the melt season, the standard deviation of each IC observation is set as 0.3. The observation error variance for a given IST observation is a combination of the variances associated with the variances of the two classes,

$$var(IST) = 0.5var_{water} + 0.5var_{ice} \tag{5.5}$$

where var_{water} and var_{ice} are the variance of the IST for water and ice, respectively. An alternative definition of the variance was tested, in which

$$var(IST) = (1 - IC)^2 var_{water} + IC^2 var_{ice}, \tag{5.6}$$

but this did not have a significant impact on the assimilation results.

Table 5.1: Mean and variance of IST for ice and water estimated from IST data for June to August 2007.

class	mean (K)	variance (K)
ice	271.3	3.7
water	277	8

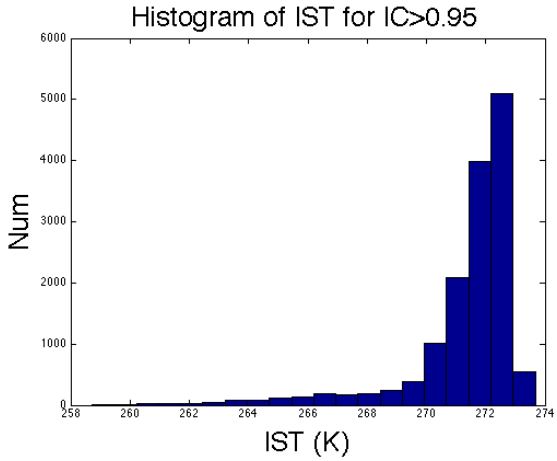

(a) Histogram for IC >0.95

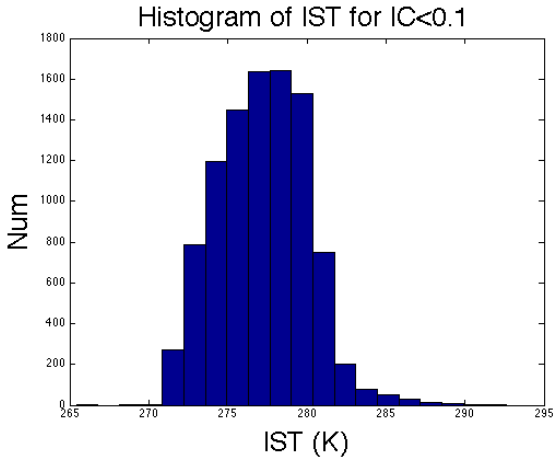

(b) Histogram for IC <0.1

Figure 5.3: Histogram of IST for (a) ocean grid points with IC >0.95 (b) ocean grid points with IC <0.1.

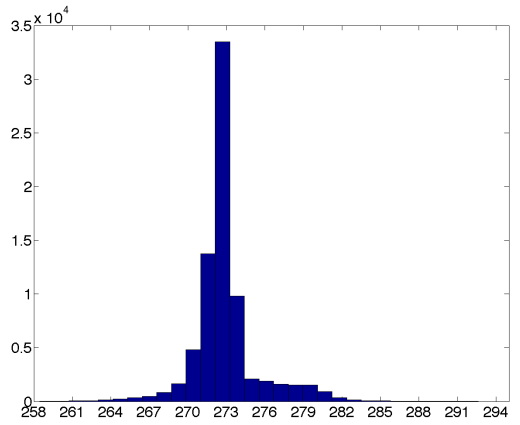

(a)

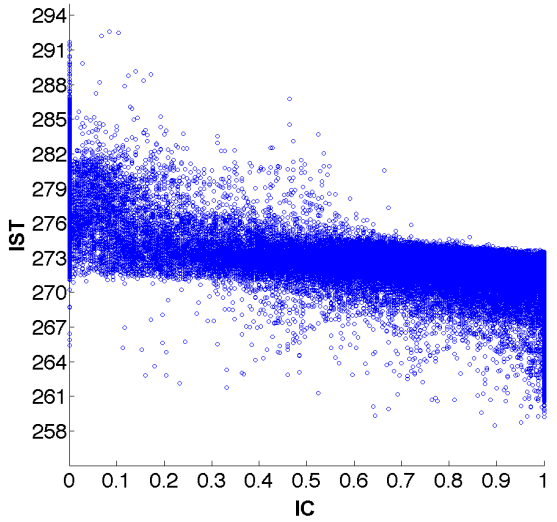

(b)

Figure 5.4: Statistics of the IST and IC for all data from June 1st to August 31th. (a) Histogram of the IST (b) Scatter plot of the ice concentration and IST.

5.3.3 Experimental Set-Up

The experiments were carried out assimilating SSM/I ice concentration and MODIS ice surface temperature data from June 1st 2007 to August 31th 2007. The ice concentration data from SSM/I are assimilated daily over the entire domain, while the MODIS IST are assimilated for cloud free ocean grid points each day. The background ice concentration is initialized using SSM/I ice concentration of June 1st, 2007. A flowchart showing the assimilation process is shown in Figure 5.5.

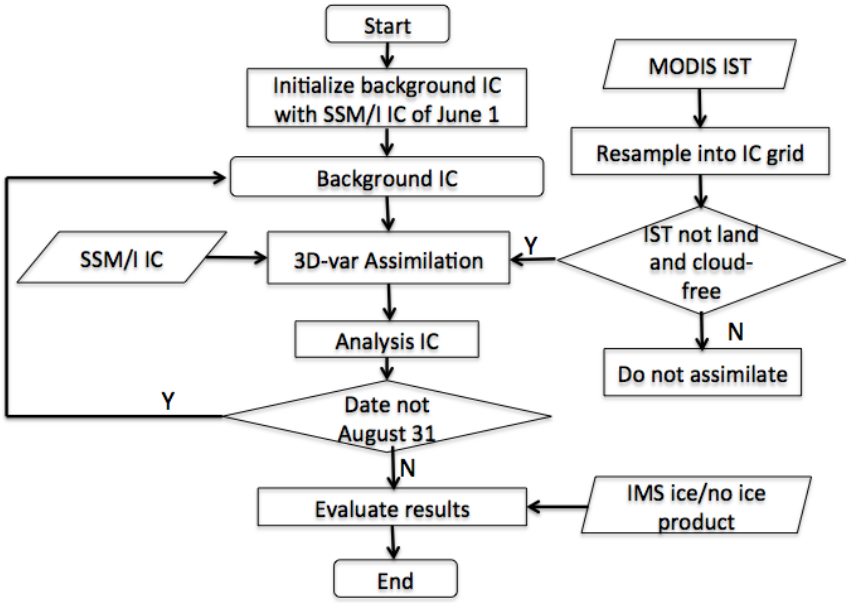

Figure 5.5: Flowchart describing the assimilation of the SSM/I ice concentration (IC) and MODIS ice surface temperature (IST) data.

5.4 Results

5.4.1 Verification Against Ice Extent from NOAA

The ice concentration analysis is compared with the sea ice extent from NOAA Interactive Multisensor Snow and Ice Mapping System(IMS) (*Chen et al.*, 2012). The ice/no ice based IMS product is manually created by trained analysts using available satellite imagery, several automated snow mapping algorithms, and other ancillary data. The spatial resolution of the IMS data is 16 km^2. The IMS product is resampled into the SSM/I grid. The validation using IMS data follows *Scott et al.* (2013), *Buehner et al.* (2013) and uses a threshold of 40% to transform the ice analysis and the SSM/I ice concentration into ice/no ice. 40% is used because IMS ice extent product uses 40% to correlate with National Ice Center (NIC) ice chart. The total proportion correct (PC) is defined as the percentage of pixels that are correctly labeled as ice or water compared to the IMS product. The proportion correct for ice is defined as the number of pixels that are correctly labeled as ice compared to the IMS product divided by the total number of ice pixels in the IMS product. The proportion correct for water is defined as the number of pixels that are correctly labeled as water compared to the IMS product divided by the total number of water pixels in the IMS product.

The verification is done over three subregions: the CAA, the Arctic Ocean and Baffin Bay. Verification scores for these three regions are plotted in Figure 5.6 for each day of the experiment from June 1 to August 31. Note that IMS data for July 23 is missing and not included in the verification. For the CAA region, the ice extent calculated using the IC from SSM/I agrees with the IMS product very well until mid July. After that, the SSM/I data quality degrades greatly, which corresponds to the ice melt period in the CAA. The assimilation of MODIS data is shown to improve the total proportion correct by 5% to 10% in the CAA region during the melt. For the Arctic Ocean and Baffin Bay, the differences between the analysis and SSM/I ice concentration were largest in late August and middle July, respectively. These periods correspond to the timing of sea ice melt in these regions.

The proportion correct for ice and water for each day in the CAA are shown in Figure 5.7. It can be seen that more ice has been correctly identified in the analysis than

when the original SSM/I data is used. However, it also seems less water has been correctly identified in the analysis than when the original SSM/I data is used. To understand this, the number of pixels that are correctly and falsely classified for both analysis and SSM/I for water and ice, respectively, are shown in Figure 5.8. The number of pixels that are correctly identified as ice in the analysis is larger than that of the SSM/I, with the number of pixels that are falsely identified as ice smaller than the SSM/I during the melt. Meanwhile, the number of pixels that are correctly/falsely identified as water does not change much between the analysis and the SSM/I. Thus, it can be concluded that the analysis improves the ice estimation by identifying more ice pixels during melt, while the estimation of water does not change much.

The background ice concentration state used by the assimilation is the analysis from the previous day projected forward in time. The analysis increment is defined as the difference between ice concentration analysis and background ice concentration. The ice concentration (IC) data increment is defined here as the difference between the ice concentration analysis and the original SSM/I data. The distribution of analysis increments and IC data increments for all the days in the study period are shown in Figure 5.9a. It can be seen that the analysis increments generally follow the normal distribution. The IC data increments are also of interest to known how the data assimilation results improve the original SSM/I sea ice concentration data. The distribution of the IC data increments for the study period is shown in Figure 5.9b. The distribution of IC data increments has a positive bias. This agrees with the fact that SSM/I sea ice concentration tends to underestimate the ice concentration. Thus, the analysis has improved the overall accuracy of the original ice concentration data by increasing the ice concentration.

For the CAA region, the daily sea ice extent and daily sea ice extent change based on the SSM/I ice concentration and the ice analysis for the three month study period in 2007 were calculated (Figure 5.10). It can be seen that both the daily sea ice extent and daily sea ice extent change are smoother for the ice analysis than when using only SSM/I data. Based on the daily ice extent change curve, it can be seen that the ice retreat in the CAA region follows a pattern, with a large daily sea ice loss phase in late June, then a daily ice increase phase in early July, and then gradual daily ice loss until the end of August.

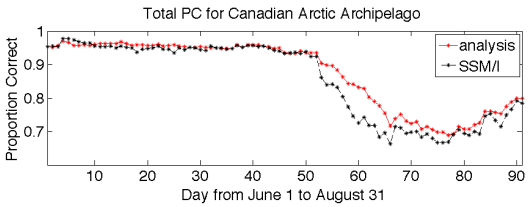

(a) Canadian Arctic Archipelago

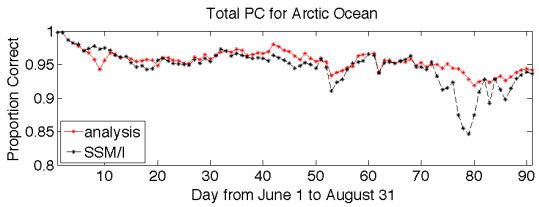

(b) Arctic Ocean (AO)

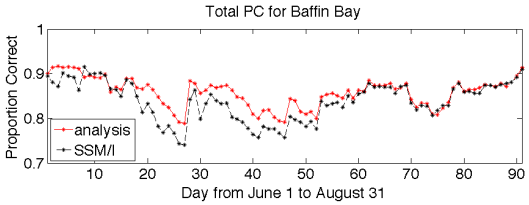

(c) Baffin Bay (BB)

Figure 5.6: Total proportion correct for each day from June 1 to August 31 2007 for (a) Canadian Arctic Archipelago (CAA), (b) the Arctic Ocean (AO) and (c) Baffin Bay (BB).

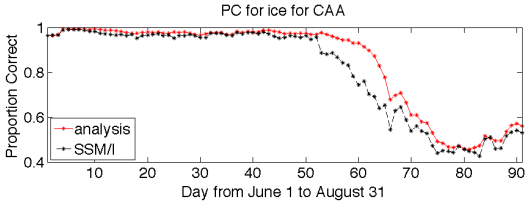

(a) Proportion correct for Ice

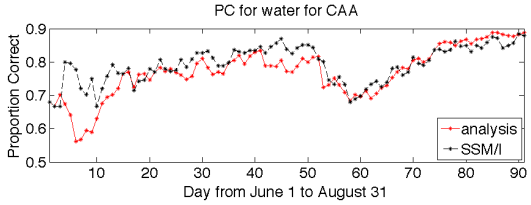

(b) Proportion correct for Ice

Figure 5.7: Proportion correct for (a) Ice and (b) water, for each day from June 1 to August 31 2007 for the CAA.

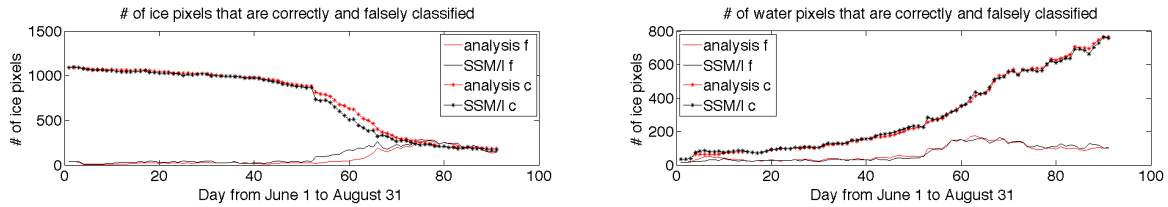

(a) # of ice pixels correctly/falsely classified (b) # of water pixel correctly/falsely classified

Figure 5.8: Number of pixel correctly/falsely classified for (a) Ice and (b) water, for each day from June 1 to August 31 2007 for the CAA.

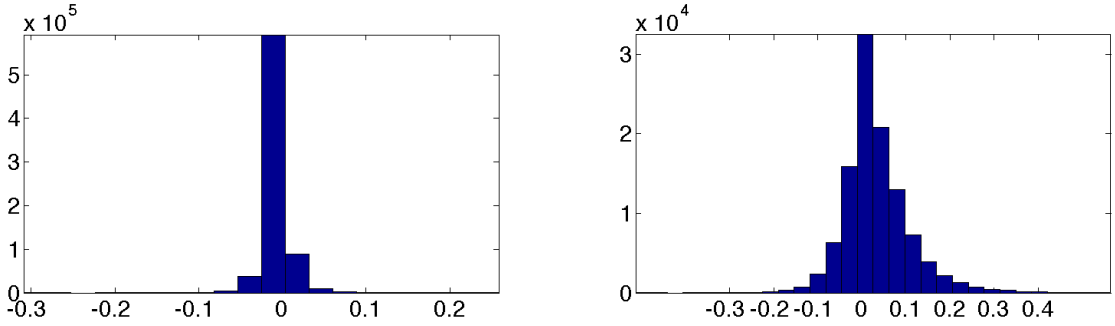

(a) Model increment (b) Ice data increment

Figure 5.9: Distribution of the increments (a) Model increment and (b) IC data increment.

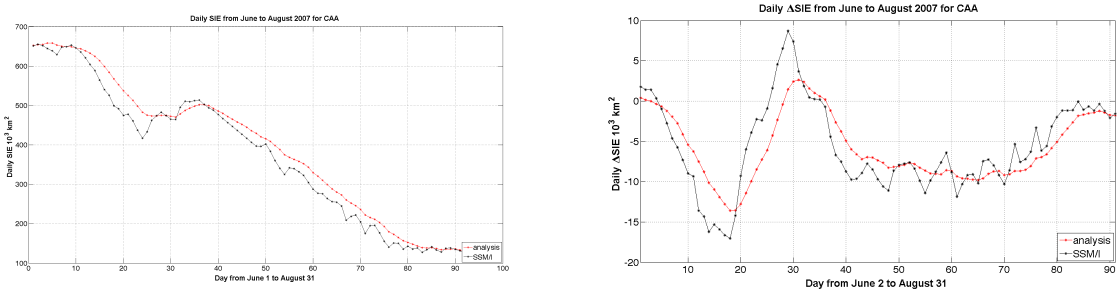

(a) (b)

Figure 5.10: (a) the daily ice extent and (b) the daily ice extent change for the CAA from June 1st to August 31th.

5.4.2 Selected Case Study

The data assimilation results are shown for three selected days from the sea ice retreat phase 2, 3 and 4. (Figure 5.11, 5.12, 5.13). The selected days all have relatively little cloud cover in the CAA region. Six maps are shown for each day. These maps are ice concentration background, ice concentration analysis, the analysis increment, the original SSM/I, the IST and IC data increment. On June 26th, the IC data increment map show positive incremental in most of the CAA (Figure 5.11f). These positive increments mean that the ice concentration of the analysis is larger than the original SSM/I SIC data. On July 2nd, ice concentrations in the analysis are smaller than the original SSM/I SIC data in most of the CAA region, as negative increments are shown on the IC data increment map (Figure 5.12f). On July 27th, ice concentrations in the analysis is again larger than SSM/I SIC in most of the CAA, as large area of positive increments is shown on the CAA IC increment map (Figure 5.13f).

In late June (phase 2), SSM/I SIC is underestimated during phase 2 when melt ponds form. The ice concentration analysis corrects this underestimation by increasing the original sea ice concentration. In early July (phase 3), the SIC analysis is smaller than original SSM/I SIC data. In late July (phase 4), the ice concentration analysis is larger than the original SSM/I SIC data. By examining Figure 5.10, it is also clear that the ice concentration analysis is larger than the original SSM/I SIC data in phase 2 and smaller than the original SSM/I SIC data in phase 3. Based on our quantitative comparison, the overall accuracy of ice concentration has been improved. However, further information is needed to investigate whether the decrease of SIC by the analysis in phase 3 is valid.

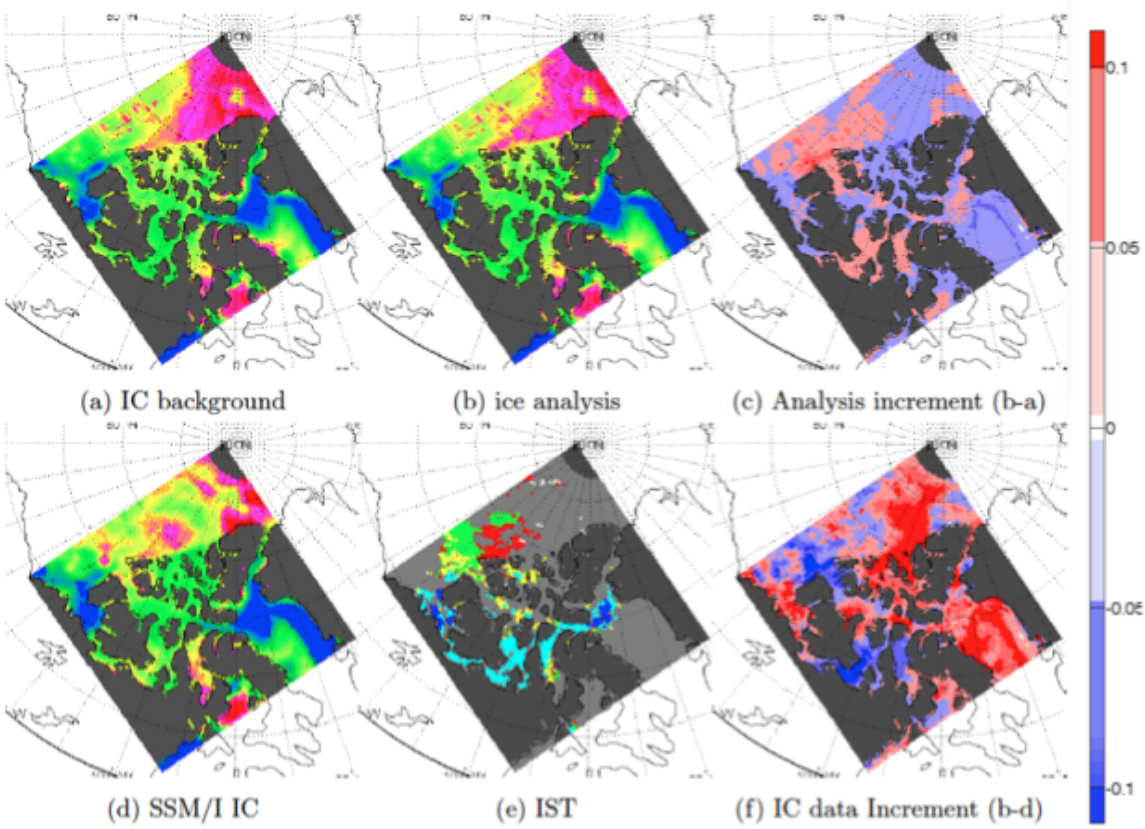

Figure 5.11: Results for June 26th 2007. The color map for model increment (c) and ice data increment (f) are shown here, with positive increments shown in red and negative increments shown in blue. The color map for ice concentration can be found in Figure 5.1, while the colors used for IST are defined in Table 3.1.

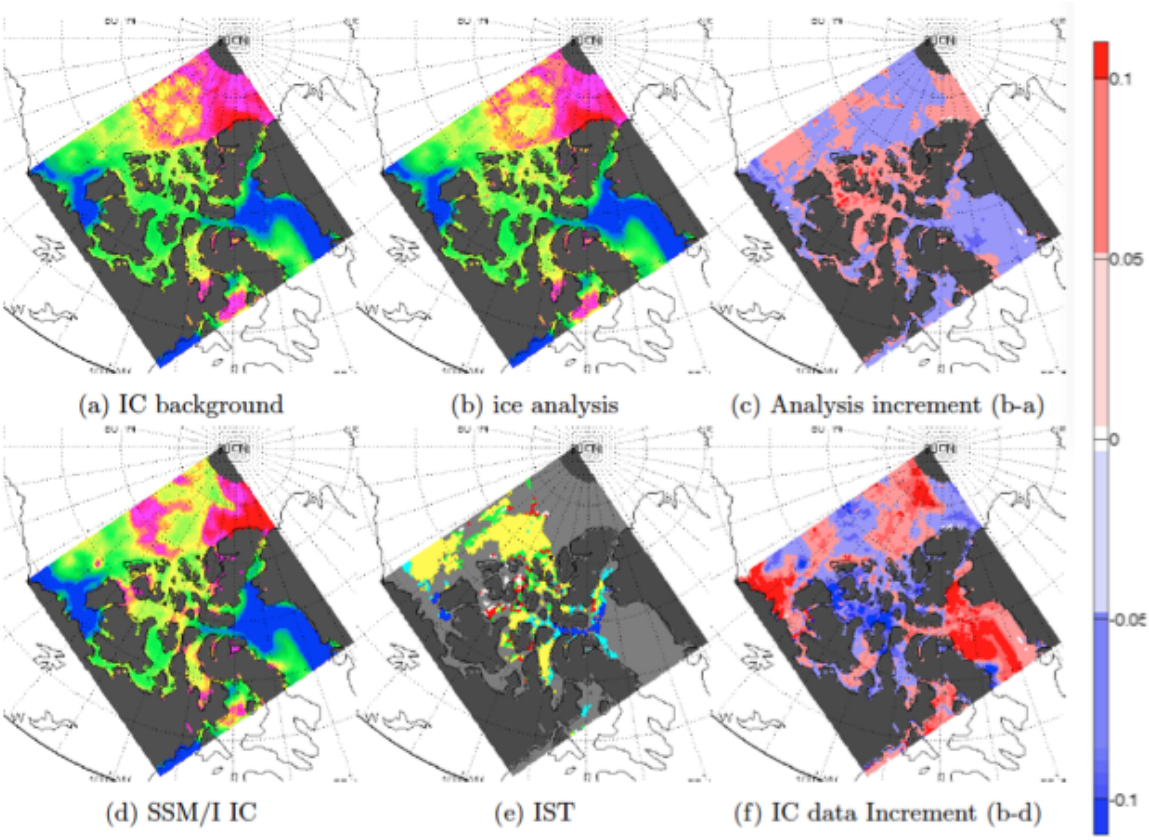

Figure 5.12: The same as in figure 5.11 but for July 2nd 2007.

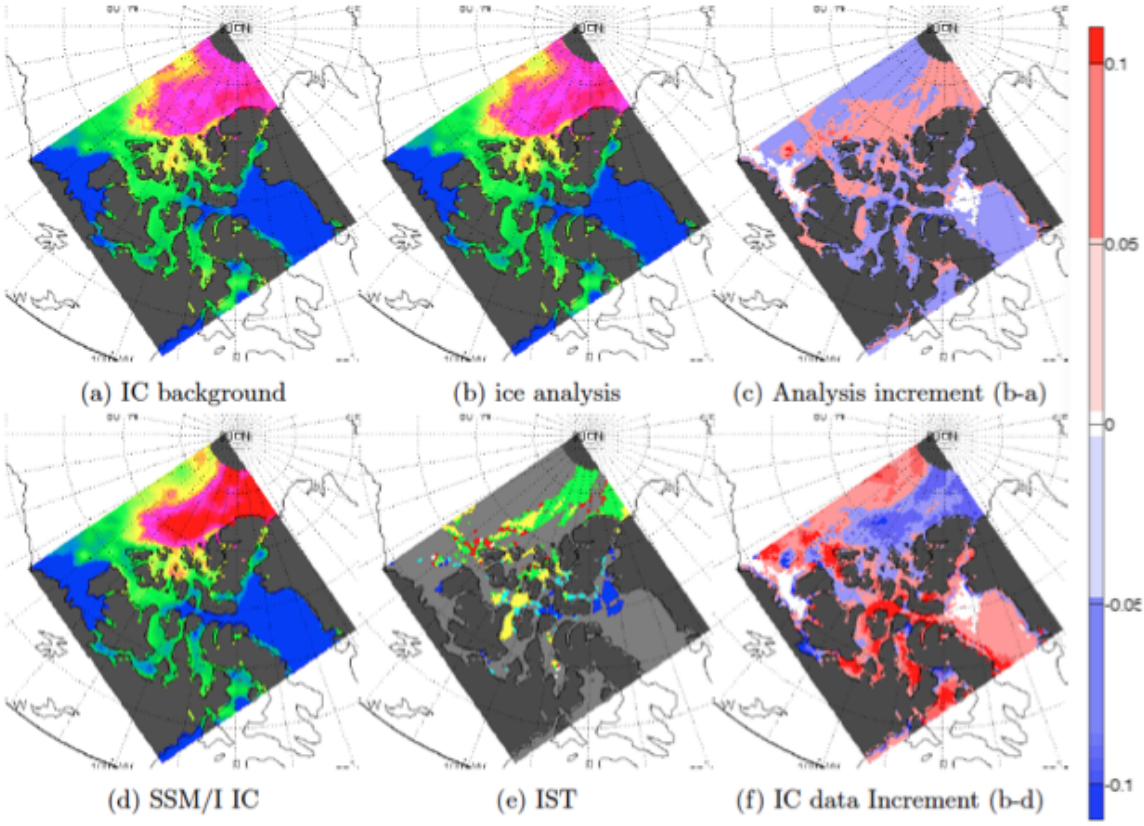

Figure 5.13: The same as in figure 5.11 but for July 27th 2007.

5.5 Summary

The SSM/I derived ice concentration is known to have large uncertainties during the ice melt season. In this chapter, the MODIS ice surface temperature (IST) product is assimilated with the SSM/I ice concentration data with the goal of producing an improved estimation of ice concentration. To assimilate MODIS IST, a simple linear model is defined as the forward model that maps the background sea ice concentration to the observation IST space, where ice surface temperature is modeled as a function of ice concentration and open water fraction. The background error covariance matrix is modeled as spatially and temporally homogeneous. The data assimilation method has been tested over the

Canadian Arctic region for three months from June to August in 2007. Results from the assimilation are verified against NOAA IMS ice extent data. It has been found that the analysis from the assimilation is in better agreement with the data from the IMS during sea ice melt, as compared to using only ice concentration calculated from SSM/I data. The improvement seen here is significant when it is considered that only cloud-free pixels with valid IST values can be assimilated. Future work will focus on the development of a method to assimilate reflectance data in addition to surface temperature data.

Chapter 6

Interannual Sea Ice Change Detection

6.1 Introduction

Arctic sea ice area has undergone a significant decline in recent years. The change and variability of time series of Arctic sea ice concentration has been studied in numerous scientific papers. Many studies show that the decline of Arctic sea ice has accelerated since the inception of the satellite era (1979 to present). *Parkinson and Cavalieri* (2008), *Comiso and Nishio* (2008), and *Perovich and Richter-Menge* (2009) all report a declining trend for September sea ice extent. Ice phenology defines the ice growth and decay cycle of a year. Ice phenology change deserves special attention because it is a direct indicator of climate change. Notably, a warming Arctic has led to ice phenological timing shifts toward later start of freeze-up and the earlier start of melting, leading to the lengthening of the melt season (*Markus et al.*, 2009). This contributes to the severe sea ice loss (*Serreze et al.*, 2007b).

When measuring the interannual trend in sea ice change and variability, the ice extent for specific dates or the monthly and seasonal means are sampled from high resolution time series (e.g. daily sea ice maps). The selection of a few isolated dates for change detection

is appropriate only when it can be assumed that there is no significant seasonal variation in the spatial pattern of the icescape. Moreover, sea ice extent trends are often calculated on a regional scale and the spatial patterns at pixel level are generally lost. However, the geographic location of the areas with phenological timing shifts are changing from year to year, with some years being more severe than other years. For example, the Western Arctic, including the Beaufort Sea, Chukchi Sea, Eastern Siberian Sea, Laptev Sea and Kara Sea suffered the most significant summer sea ice loss compared to that of the other regions of the Arctic in summer 2007 (*Serreze et al.*, 2007b). Thus, the identification of the geographic locations where the yearly sea ice phenological changes most often occur is important for improved understanding of the processes of sea ice change.

Im and Jensen (2005) noted that remote sensing change detection generally has three goals, namely, detect the location of the change, identify the types of change, and quantify the amount of change. Change detection from multi-temporal remote sensing images has long been studied for various applications. *Lu et al.* (2004) illustrated a comprehensive review of the change detection techniques using remotely sensed data. Principal component analysis is often used to find the sea ice distribution patterns that explain most of the variance in the data for the analysis period (*Piwowar and LeDrew*, 1996), but the derived principle components are aggregated patterns and statistically meaningful, but without any guarantee that the patterns are physically meaningful unless there is extensive visual validation. Temporal mixture analysis was proposed for sea ice change detection (*Piwowar et al.*, 1998). Three to four end members are defined as the purest pixels and each pixel is assigned a percentage of purity. Ice change can be captured by each end member's percentage of change in a pixel. However, the identification and interpretation of the end members are not always straightforward. *Small* (2012) proposed a new method to characterize multitemporal imagery by the combined use of principal component analysis and spectral mixture analysis. The above methods do not have sufficient involvement of high temporal resolution data for continuous monitoring of change, however. Temporal trajectory analysis has been commonly used to monitor vegetation change based on land surface phenology at regional, continental, and global scales (*Coppin et al.*, 2004, *de Beurs and Henebry*, 2006, *Hargrove et al.*, 2009). Temporal mixture analysis results in a fusion of temporal information at different times, but phenology based clustering regions of the tem-

poral trajectory analysis provide direct and easy to interpret maps of the subject studied. When the clustering regions of different years are compared, the location where changes have occurred is directly available.

In our sea ice change detection domain, both the spatial and temporal downward trends of Arctic sea ice are undeniable, but the changes are not coherent when different regions and different months of year are examined. Arctic sea ice change occurs over a wide range of temporal and spatial scales. Temporal variations occur from days, weeks, and months to periods of years, decades and longer. Spatial variations occur at regional to synoptic and hemispheric scales. Sea ice phenology provides information about the sea ice annual cycle, such as the maximum/minimum sea ice extent (SIE) of a region, the timing of the maximum/minimum, the timing of melt/freezeup onset, and the length of melt season. Because of the sea ice phenological change, including the reductions in stable old ice, increases in unconsolidated ice, and lengthening of the melt season, Alaskan polar bear denning has been shifted landward and eastward (*Fischbach et al.*, 2007), while the sea bird hatch dates also advanced in the high-Arctic (*Moe et al.*, 2009).

We need to identify where sea ice phenological change has occurred, what is the nature of the phenological change, as well as the degree of change. The daily passive microwave sea ice concentration (SIC) data accumulated for the past three decades provide a hyper-temporal dataset for change analysis. In this analysis, we will make use of the sea ice phenological information to investigate the sea ice spatial and temporal changes in the Arctic in two steps. First, we generate a phenoregion map for each year in the study period based on decision tree classification of the temporal SIC profile. A phenoregion map integrates the sea ice melt information of a year for an interval we have defined as the active period from April to August. Secondly, the spatial and temporal characteristics of the phenoregion maps are analyzed. In the following section, the phenoregion maps of different years are compared, and the location and degree of change of the phenological classification map are identified. Thus, the spatial and temporal details about the timing and the locations where the changes occur are answered at the pixel level.

Within the context of this discussion, it is important to highlight that the ice edge is not a symmetric ring around the pole in either summer or winter. The controls of the sea ice edge position have been poorly understood. The wintertime ice edge depends primarily

on coastline geometry, ice motion, and the melt rate at the ice-ocean interface, driven by absorbed solar radiation and the convergence of heat transported by ocean currents (*Bitz et al.*, 2005). *Melling* (2012) proposed that the ice edge is the location where the rate of ice loss through melting equals that of delivery via drift. Ocean bathymetry influences the distribution and mixing of warm and cold waters, and plays a profound role in controlling the location of sea ice edges by influencing the Arctic sea ice formation and seasonal evolution (*Nghiem et al.*, 2012).

6.2 Exploratory Data Analysis

6.2.1 Annual Daily ΔSIC Profiles

The annual SIC profile of a pixel is defined as the time series of its daily SIC of a year, which shows the pixels sea ice decay process during that year. The annual SIC profile contains all the information about the pixel's SIC evolution. The 22-year mean of a pixel is used to explore the mean cycle of SIC for that pixel in a year. Phenological metrics, such as melt/freeze onset and the length of the melting season can be used to characterize the sea ice annual profile (Table 6.1). Changes in any of these factors, such as an earlier melt onset or a longer melting season, lead to changes in the SIC profile. The SIC profile captures detailed information about the time-trajectory of the sea ice annual evolving patterns compared to methods that only use one value at a particular time period to represent a year.

Table 6.1: Representative attributes of sea ice melt phenology

Representative attributes of sea ice melt phenology
1. Time for the melt onset
2. Maximum rate of ice loss
3. Time of minimum sea ice concentration
4. Amplitude of minimum sea ice concentration

The annual SIC profile and the annual daily ΔSIC of several selected pixels are shown in Figure 6.1 for three different years (1998, 2004 and 2007). The black lines show the mean annual cycle for the same pixel for the entire 1989 to 2010 observational interval. Figure 6.1a shows a pixel close to Resolute Bay. For the selected pixel located in Resolute, the annual cycle profiles for 1998 and 2007 years are below the mean annual cycle and 2004 is well above the mean annual cycle. Moreover, the ice-free length varied greatly, with 2007 has the longest ice-free duration.

For the selected pixel located in Lancaster Sound, the timing of the ice-free date varied by up to a month due to the different timing of melt onset (Figure 6.1b). It can be seen that the selected pixel in Lancaster Sound had a significantly different sea ice retreat pattern in 2004 compared to 1998 and 2007. Based on the inspection of weekly SIC maps from the Canadian Ice Service Archive, the breakup of ice in Lancaster Sound was middle May in 1998 and late May in 2007. At that time, the area connecting the Baffin Bay and Lancaster Sound still has some ice coverage (Figure 6.2). Therefore the ice can move into Lancaster Sound from the east from Baffin Bay. However, the opening of the Lancaster Sound was in late June in 2004, and all ice in the area that connected Lancaster Sound and Baffin Bay had melted away (Figure 6.3). Thus, no ice could intrude into Lancaster Sound from the east, and the temporal decrease in concentration was much more rapid than in the other case study years.

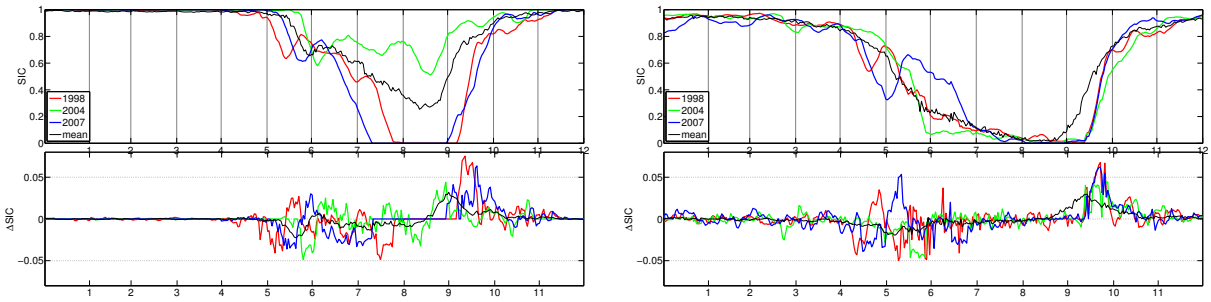

(a) a pixel in Resolute

(b) a pixel in Lancaster Sound

Figure 6.1: Annual SIC and SIC change time series for (a) a pixel in Resolute (b) a pixel in Lancaster Sound.

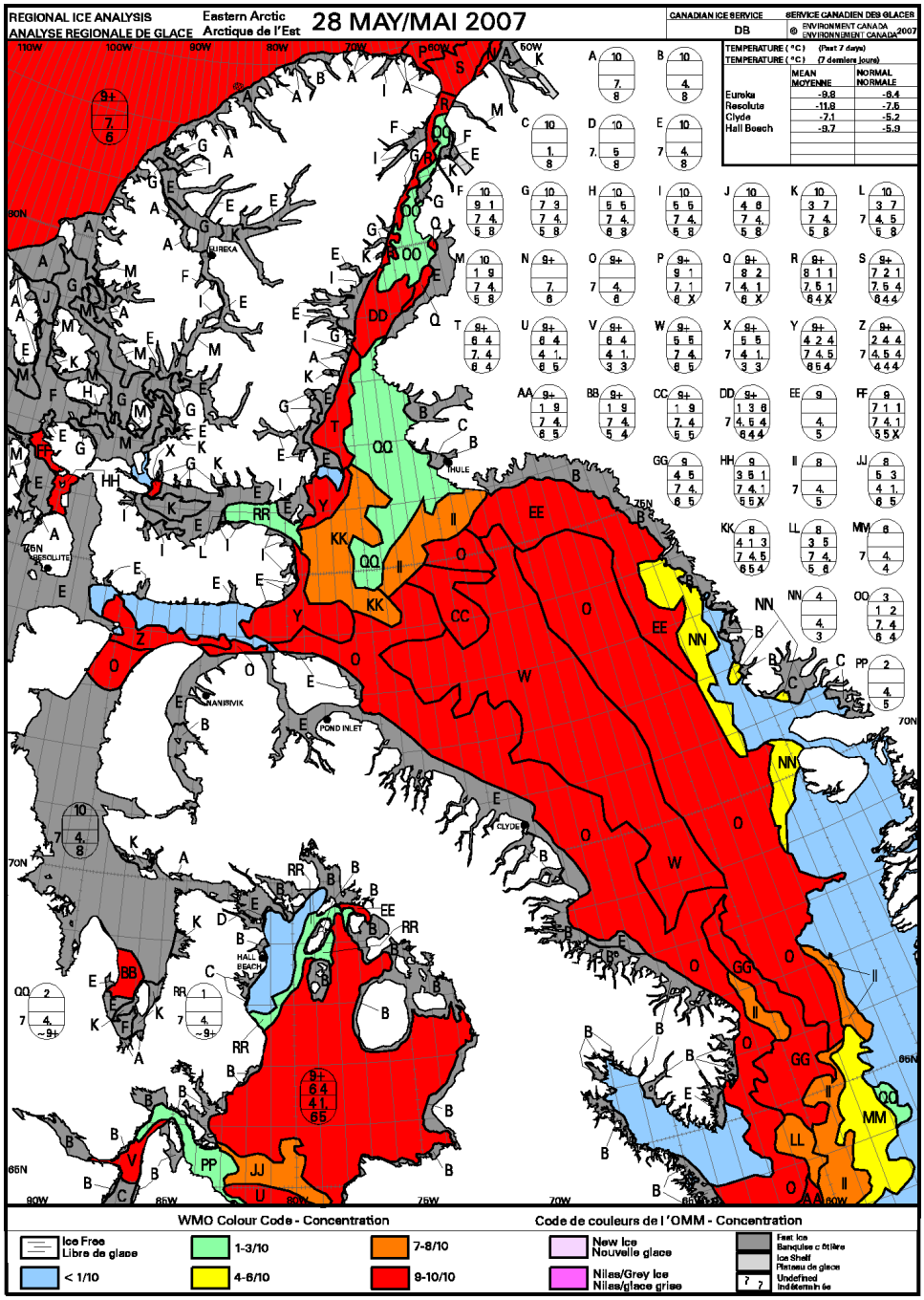

Figure 6.2: Weekly SIC chart for Eastern Arctic on May 28, 2007 from Environment Canada

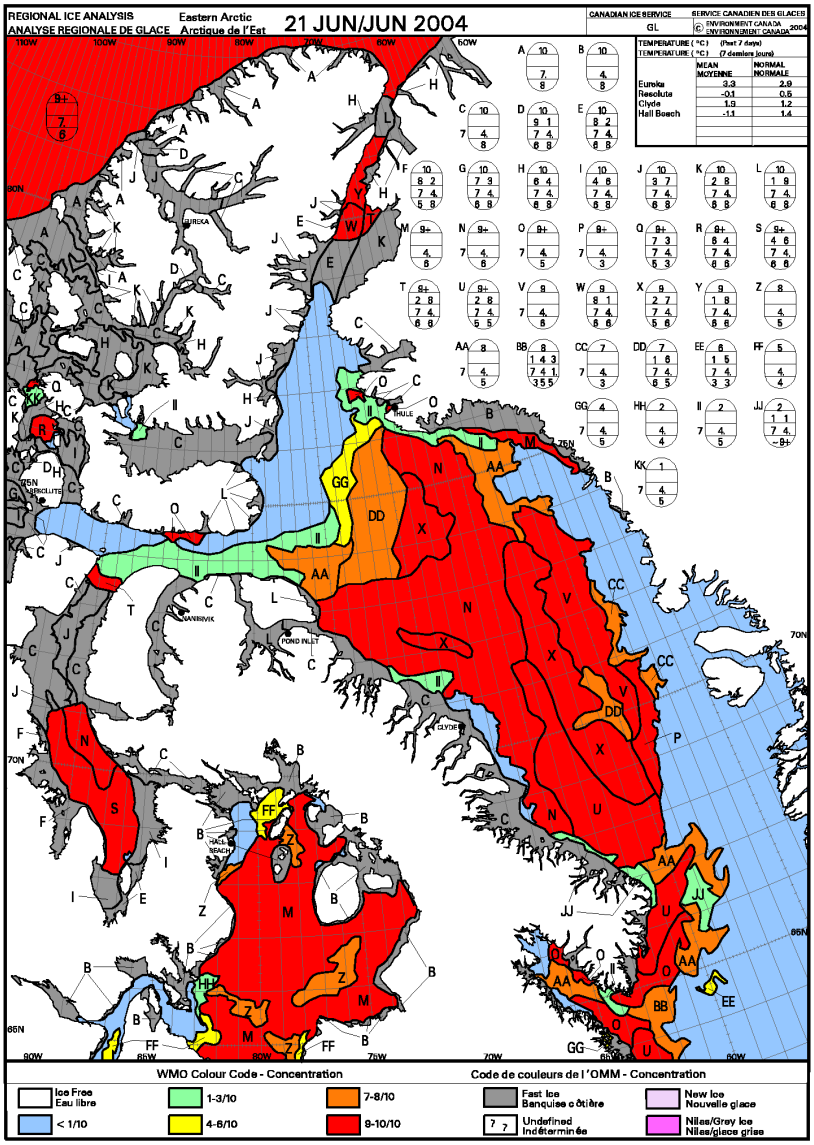

Figure 6.3: Weekly SIC chart for Eastern Arctic on June 21, 2004 from Environment Canada

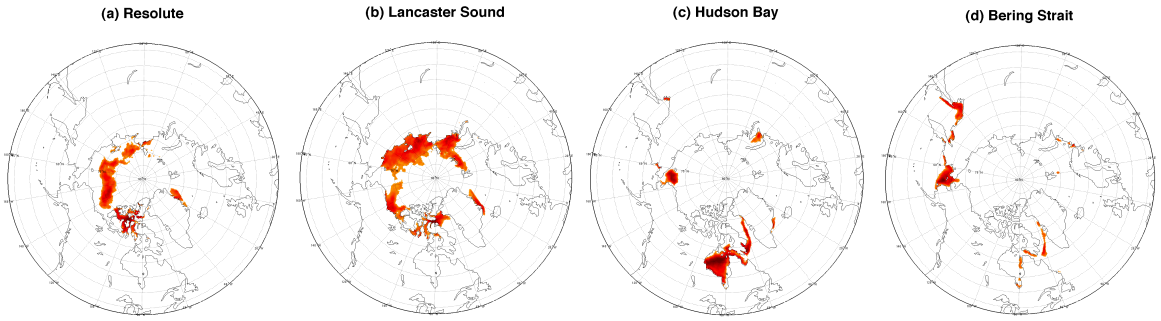

Figure 6.4: The correlation coefficients between the annual SIC profile of a selected pixel in an area and all other Arctic pixels with a R>0.7.

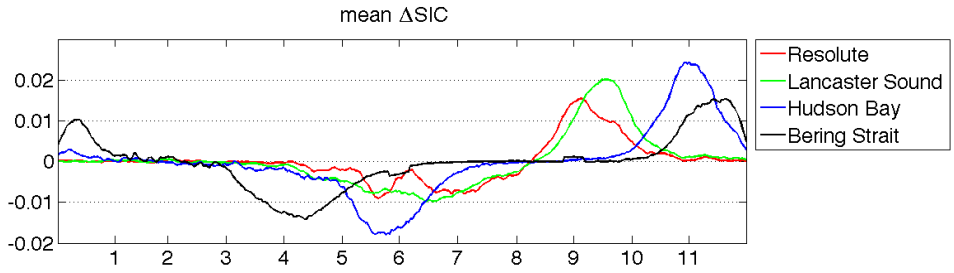

Figure 6.5: The mean annual SIC profile for all pixels in each of the maps shown in Figure 6.4

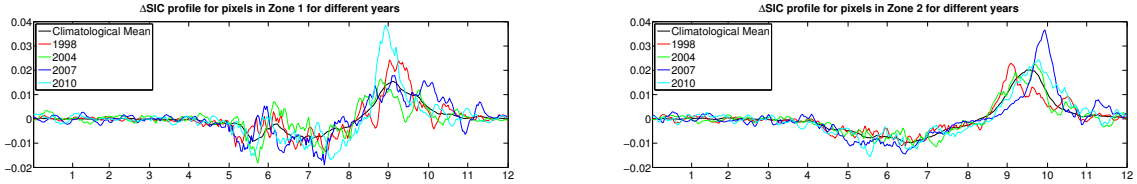

(a) (b)

Figure 6.6: (a) ΔSIC profile for pixels that have high correlation with Resolute in different years and (b) ΔSIC profile for pixels that have high correlation with Lancaster Sound in different years

6.2.2 One-Point Correlation Map based on Daily ΔSIC Profiles

To understand if there is any correlation between the annual cycle of sea ice in areas of large geographic distance, e.g., between different regions of the Arctic, the one-point correlation map is used here. One-point correlation maps have been used in *Wallace and Gutzler* (1981) to define the North Atlantic Oscillation (NAO) index, which defines the correlation of pressure changes between different parts of the northern hemisphere. For the same location, its annual cycle of sea ice profile changed greatly from year to year. Considering these large variations in sea ice annual profile in different years for the same location, the 22-year climatological mean is used in this section. For a pixel, its annual ΔSIC profile is based on the 22-year mean of the daily ΔSIC of that pixel. A correlation map is constructed by correlating the annual ΔSIC profile at a reference point with the corresponding time series at all pixels in the Arctic. Pixels that have high correlations with the reference point are shown on the correlation maps.

To explore how the sea ice annual cycles in the CAA region are connected with other Arctic regions, two reference points are selected in the CAA. One is located close to Resolute, and the other is located in Lancaster Sound. These two locations are selected because they represent the general sea ice cycle of most parts of the CAA. Lancaster Sound starts to melt first for the region, followed by the inner part of the CAA channels. Two more reference points are selected to represent other sea ice annual cycle patterns in the Arctic. One is located in Hudson Bay, and the other is located in Bering Strait. The constructed correlation maps are shown in Figure 6.4. These maps quantify the similarity of the annual ΔSIC profiles of the reference points with all other pixels in the Arctic.

Based on these four correlation maps, we selected the mean daily ΔSIC for the pixels shown in red on each map (Figure 6.5). For all the pixels on each map, we calculate their annual cycle for each year as shown in Figure 6.6. For the three years shown, the same group of pixels have very different annual cycles, even though these pixels' annual cycles are highly correlated based on the climatological mean. Thus, a pixel that has one annual sea ice retreat pattern may have a different pattern in another year.

6.3 Sea Ice Annual Profile Classification

6.3.1 Design of the Classification Scheme

The annual SIC profile of a pixel contains information about sea ice annual evolution. Two phenological metrics are selected here to define a pixel's yearly sea ice retreat pattern, the minimum SIC for the year and the day of year when that minimum SIC occurs. All annual SIC profiles for all pixels from the 22-year study period are examined based on the two selected phenological metrics. The histogram for the general distribution of the minimum SIC is shown in Figure 6.7a. Here, ice-free pixels are defined as having a SIC less than 0.15. The minimum SIC exhibits a bipolar distribution with 41% of the pixels having some ice cover all year round and 59% of the pixels having a minimum SIC of less than 0.15, which is considered ice-free. However, 14% of the study area is ice-free all year round. Thus, 45% of the study area has seasonal ice cover, some ice cover at the beginning of the melt and gets ice-free in the summer. For seasonal ice covered pixels, the day of year when ice-free occur are explored. The distribution of the day of year when the ice-free conditions occur is shown in Figure 6.7b.

We designed a classification scheme that uses the two phenological metrics and classifies the yearly SIC profiles into several classes (Figure 6.8). The number of classes is set to seven to ensure each class has some physical meaning about ice phenology. One class is reserved for pixels that are ice-free all year round. Three classes are used to define areas with seasonal ice cover, and three classes are used for areas having ice-cover all year round. Another consideration for the selection of seven classes and the corresponding thresholds is to ensure the number of pixels in each class is evenly distributed based on all pixels in 22 years. Thus, a decision tree classifier with seven classes is defined and shown in Table 6.2. The order of operations in the decision tree is not important. Ice in the areas covered by classes 1 to 3 survives the summer melt and becomes MYI in the following year. However, areas in these three different classes have different summer minimum sea ice concentrations. Classes 4 to 6 cover areas that become ice-free in the middle of summer. These three classes are defined based on the timing of the ice-free condition. Class 7 contains areas with no ice cover all year round. The percentage of pixels in each category is evenly distributed

except for class 1, considering the large area of the central Arctic.

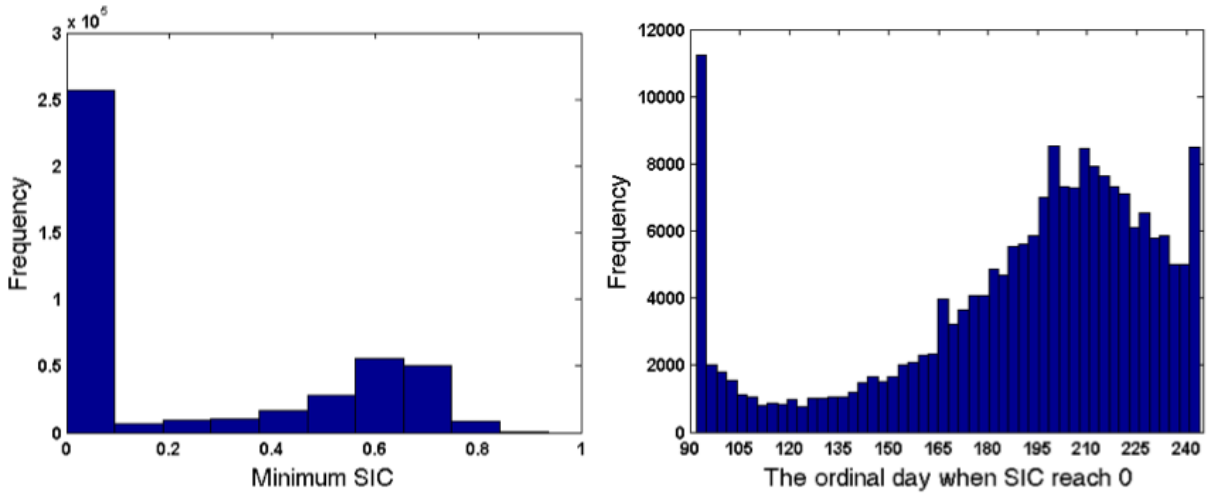

(a) (b)

Figure 6.7: (a) The distribution of minimum SIC for all pixels from all years and (b) the distribution of the ordinal day when ice-free occur for all pixels that is not ice-free at the beginning of melt (April 1st).

Table 6.2: Decision tree classifier

Criteria				Type	Ice Condition	Percentage
Min SIC	[0.6,1]			1	High SIC all year	22%
	[0.5,0.6)			2	Medium SIC all year	9%
	[0.15,0.5)			3	Some ice all year	10%
	<0.15	DOY of the Min	>213	4	Ice-free after Aug. 1st	15%
			[182, 212]	5	Ice-free in July	16%
			<182	6	Ice-free in April and May	14%
Max SIC	<0.15			7	Ice-free before April 1st	14%

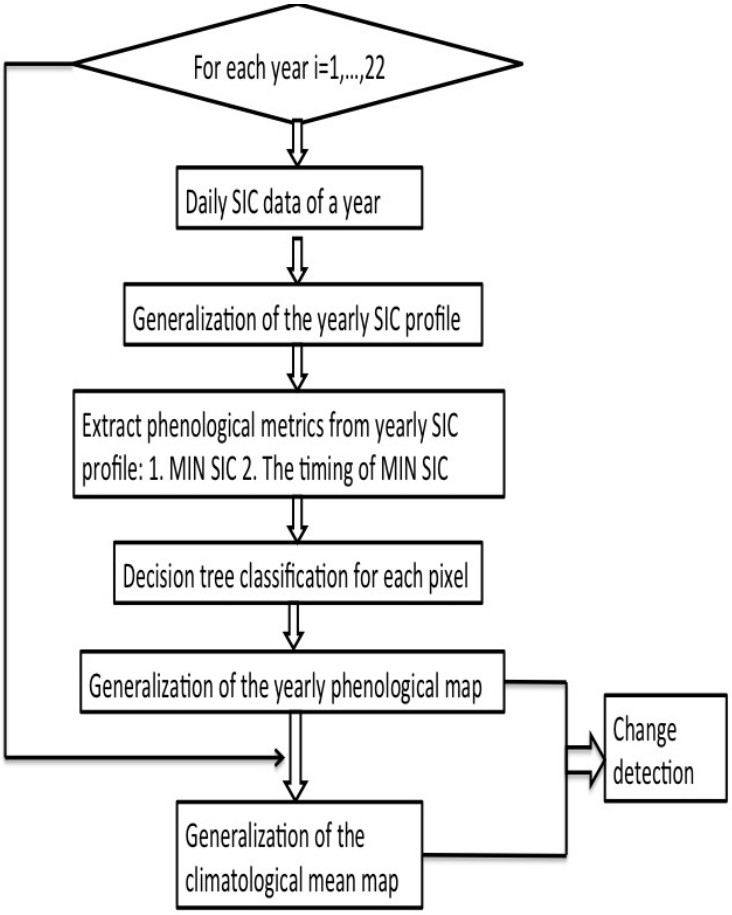

Figure 6.8: Flow chart of the generalization of yearly phenological map for change detection.

6.3.2 Generalization of the Yearly Phenoregion Map

For each year, a classification map is generated using the yearly SIC profiles of all pixels from that given year. The classification procedure is unsupervised as long as the classification scheme has been designed. Firstly, the two proposed phenological metrics, the minimum SIC for the year and the day of year when that minimum SIC occurs, are extracted from each yearly SIC profiles. Secondly, all yearly SIC profiles are classified into seven classes using these two phenological metrics based on the classification scheme. Thus,

each pixel gets a class number, ranging from 1 to 7. Thirdly, a classification map is generated for each year using the class number of all pixels from that year. Classification maps are named as phenoregion maps. The area covered by each class is defined as a phenoregion. Each pixel belongs to one of the seven phenoregions. A phenoregion map generates an instant history of sea ice melt phenology of a particular year. Since we have data for 22 years, 22 phenoregion maps are formed using the same criteria. The phenoregion maps of different year can be compared for change detection.

6.3.3 Sea Ice Phenological Change Detection

The yearly phenoregion maps provide a basis for change detection because all maps are generated using the same criteria. A pixel belongs to one phenoregion in one year may belong to another phenoregion in another year due to ice phenology change, such as the earlier melt onset. A 22-year climatological mean phenoregion map is generated by defining the phenoregion number of each pixel as the median phenoregion number of the 22-year period. The phenoregion map of each year is then compared with this climatological mean map. Pixels that have different sea ice phenology profiles compared to their normal conditions are identified.

6.4 Results

6.4.1 Spatial Variability of the Phenoregion Maps

Based on the decision tree classifier, a phenoregion map is generated for each year (Figure 6.9). Each year, each pixel has a unique phenoregion number. The climatological phenoregion map depicts the average sea ice retreat process for the study period from 1989 to 2010 (Figure 6.10a). A large part of the central Arctic Ocean is classified as phenoregion 1, and represents pixels that have SIC higher than 60% by the end of August. The pixels classified as phenoregion 2 to 3 have high SIC at the beginning of the ice retreat, and SIC decrease to a relatively low level at the end of summer. Phenoregion 4 to 6 represent

pixels that have some ice cover at the beginning of the melt season and turn completely ice-free in the summer. The timing when these pixels get to ice-free varies greatly, ranging from early June to late August, as shown by the mean SIC profile for each phenoregion in Figure 6.10c. From the standard deviation map of the phenoregion number for the 22-year (Figure 6.10b), we can see that western Arctic has the biggest variation in phenoregion number, indicating that sea ice retreat in this region follow quite different patterns in different years.

Based on our definition of ice phenoregions, ice in phenoregions 1 to 3 survives the summer melt and become MYI in the following year, while ice in phenoregions 4 to 6 totally melt away during the summer months. Generally speaking, the boundaries of the phenoregions follows a distribution, with areas in lower latitude becoming ice-free earlier than higher latitude regions, even though we do not take the spatial location of the pixels into account in the decision tree classifier. Moreover, the spatial boundaries of each phenoregion on the mean map generally follows the oceanographic features of the Arctic. The detailed descriptions of each phenoregion are as follows:

1. Phenoregion 1 (shown in brown): Highly ice covered throughout the year, which includes the central part of the Arctic Ocean, the Northern CAA and a small tip along the northeast corner of Greenland. The spatial distribution of phenoregion 1 is highly influenced by the clockwise Beaufort Gyre and Transpolar Drift, which move sea ice to the Canadian side of the Arctic Ocean and through the Fram Strait to the Atlantic Ocean (Brandon et al., 2010).

2. Phenoregion 2 and 3 (shown in pink and orange): This region has high ice cover at the beginning of April and SIC drops to relatively low values at the end of August. These areas are transitional regions between fully ice-covered regions and ice-free regions. The transition region between high ice areas and ice-free areas is quite narrow. Once the ice is broken into pieces, it melts away fairly quick and cannot stay as partially ice covered due to the ice albedo feedback.

3. Phenoregion 4 (shown in yellow): This region has high ice cover at the beginning of April and become ice-free after August 1st. In the Atlantic side of Arctic, the

boundaries of this phenoregion generally resemble the farthest north that the warm Atlantic Water can reach to the central Arctic Ocean.

4. Phenoregion 5 (shown in green): This region has high ice cover at the beginning of April and ice melts away in July.

5. Phenoregion 6 (shown in blue): This region has low sea ice cover at the beginning of April and ice melts away in May and June. This includes peripheral seas and several areas where major polynyas in the northern hemisphere are located, such as the North Water Polynya, Cape Bathurst polynya and Northwest Water polynya (Smith and Barber, 2007). The polynyas are the areas that maintain very low SIC to ice-free conditions all year round.

6. Phenoregion 7 (shown in cyan): This region is ice-free before April 1st, and generally has no ice cover all year round.

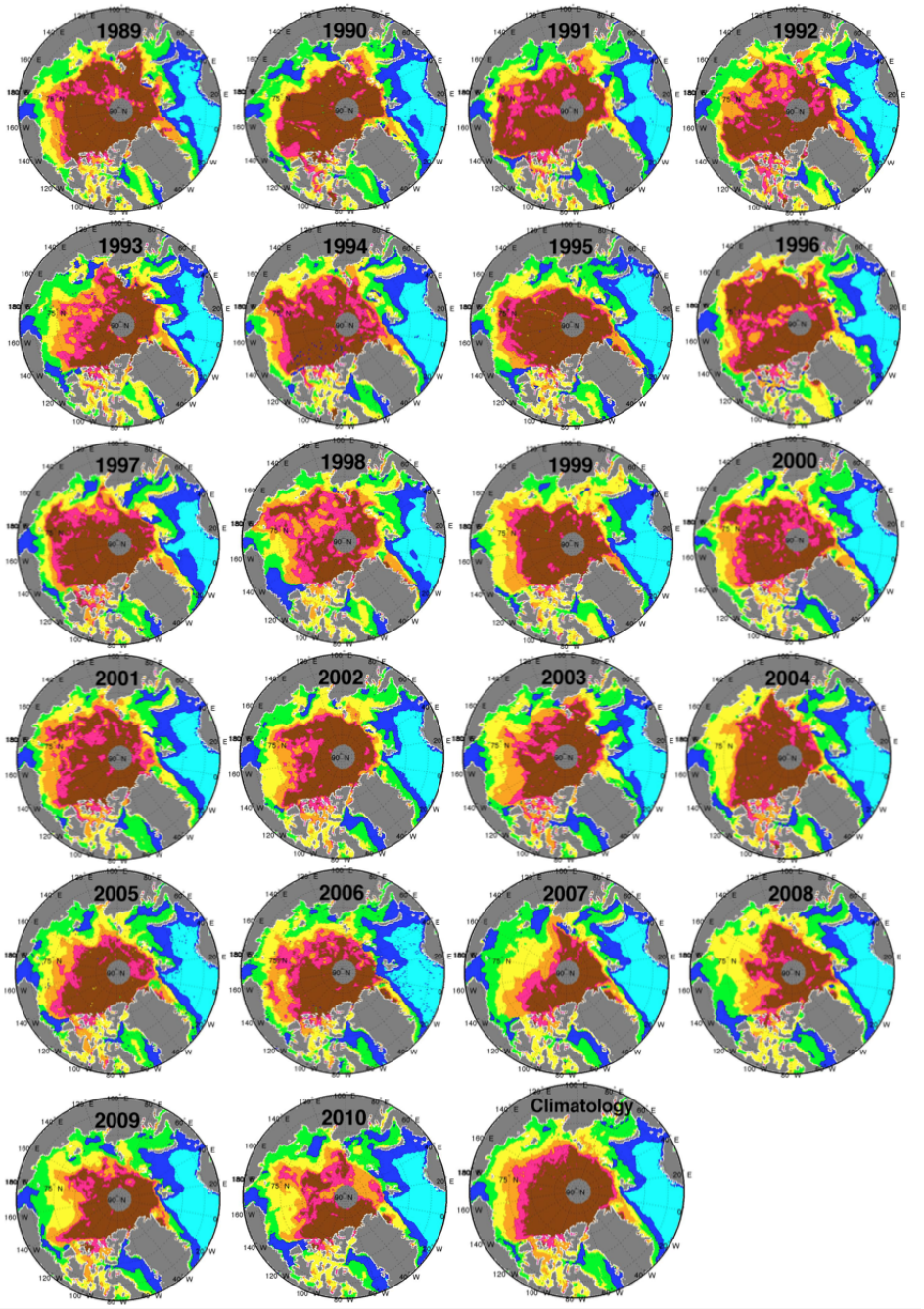

Figure 6.9: Phenoregion map for each year from 1989 to 2010, the last map is the climatological mean classification map based on the mean daily SIC for the 22-year. Phenoregion number 1 to 7 are color coded as brown, pink, orange, yellow, green, blue and cyan, respectively.

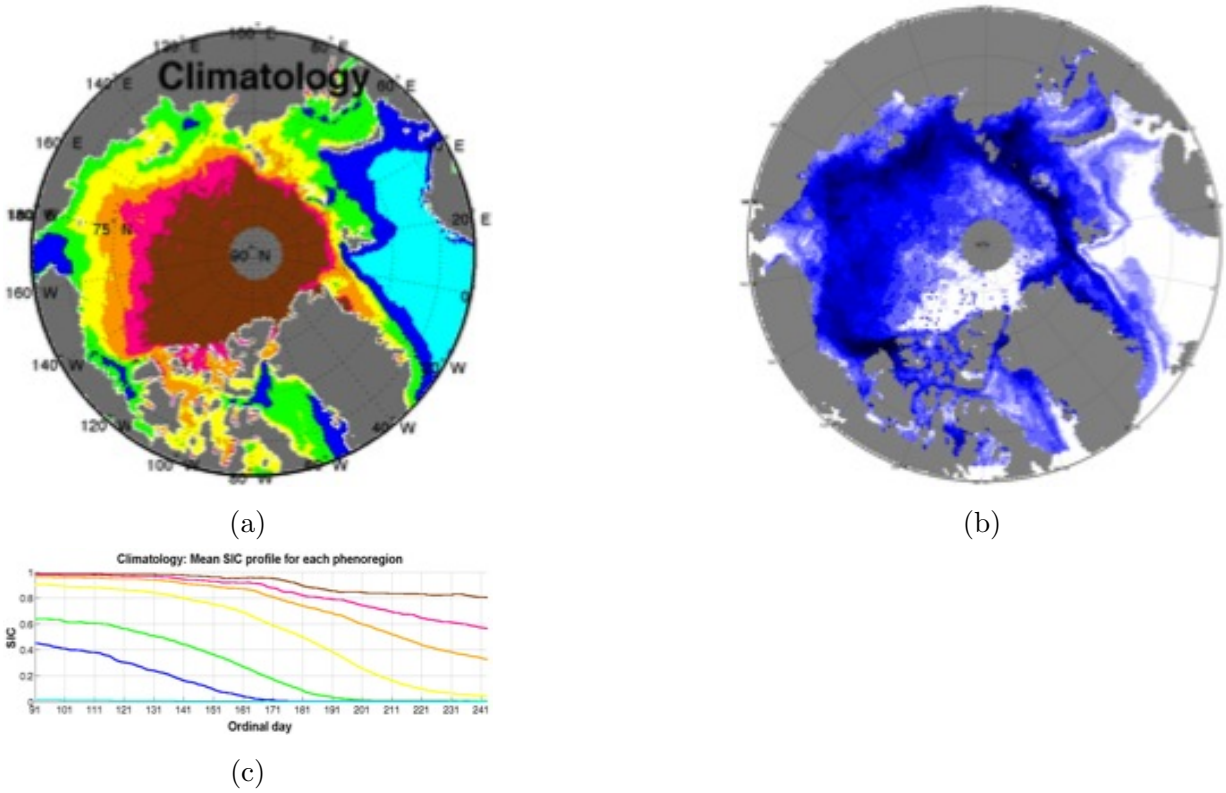

(a) (b)

(c)

Figure 6.10: (a) Mean SIC phenoregions, (b) The standard deviation map of the phenoregion number for the 22-year period with darker blue represent larger standard deviation for the phenoregion number, and (c) Mean SIC profile for each class based on the mean SIC phenoregions. The color-coding is the same as Figure 6.9.

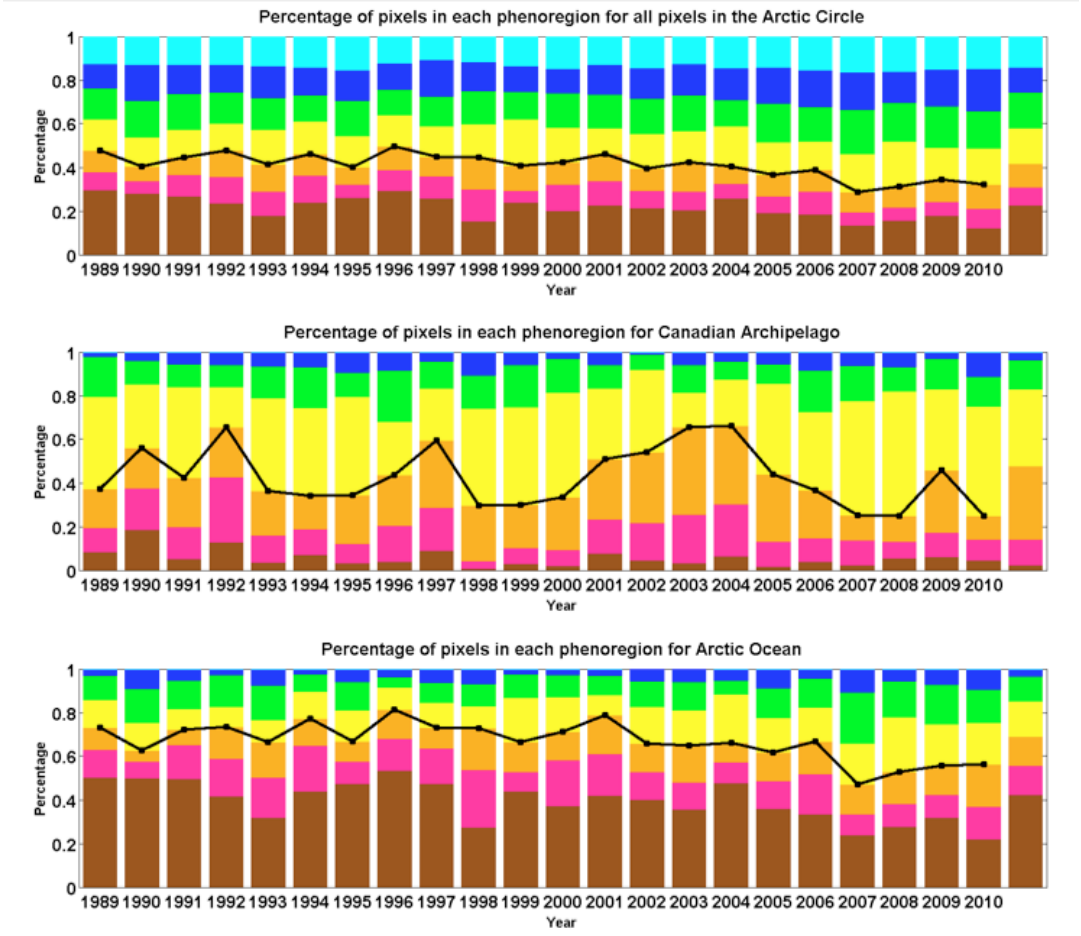

Figure 6.11: Time series of the percentage of area classified into each phenoregion from 1989 to 2010 for (a) all ocean pixels inside the Arctic Circle, (b) the CAA, and (c) Arctic Ocean. The last stack in each time series is the percentage of area for each phenoregion calculated based on the climatological mean map. The black lines on each time series are the yearly sum of percentage of class 1 to 3.

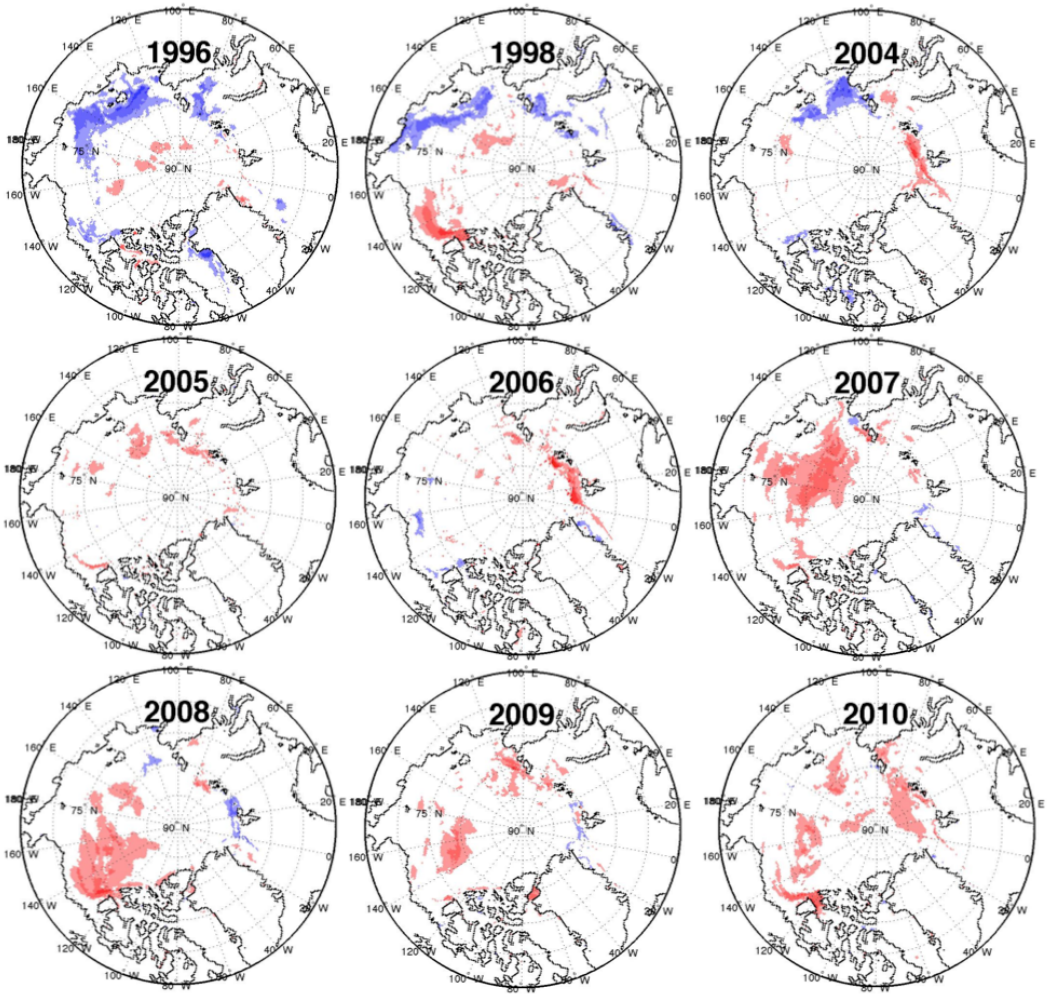

Figure 6.12: Sea ice retreat anomaly maps for selected years.

6.4.2 Temporal Variability of the Phenoregion Maps

The phenoregion maps provide information about the SIC melt pattern, as shown in Figure 6.9. Phenoregion 1 was a large region in the 1980s. However, phenoregion 1 was divided into two sectors in 1996, with some areas close to the North Pole classified as phenoregion 2 and 3. In 1998, the areas classified as phenoregion 1 to 3 were highly mixed with each other, indicating that ice was broken into pieces, probably due to ice motion. In

2010, phenoregion 1 almost disappeared from the eastern part of the Arctic Ocean. Due to the high-index of Arctic Oscillation (AO) from 1989 to 1994, anomalies wind caused increasing drift of old ice out through Fram Strait (*Rigor and Wallace*, 2004), and the area of phenoregion one has decreased precipitously. However, AO has been neutral since 1995, and it turned strongly negative during winter 2009/2010 (*Stroeve et al.*, 2011).

Year 1998 marks the lowest sea ice extent for CAA since 1979 (*Howell et al.*, 2008a). Large areas in the southern Beaufort Sea were classified as phenoregion 6 shown in blue (Figure 6.9), indicating that this area became ice-free as early as April. However, this blue area almost disappeared from the Beaufort Sea region in 1999 and 2000, implying that the ice loss was not as large as that in 1998. In the CAA, sea ice cover has recovered from 1998 to 2004 after the record low in 1998, indicated by the growing area of phenoregion 2 (shown in pink). From north to south and from west to east, more and more ice has survived the summer melt with eventual higher SIC at the end of summer.

The percentage of the total area covered by each phenoregion varies greatly from year to year (Figure 6.11). The sum of the area covered by phenoregion 1 to 3 for the study area has decreased significantly since 2007 (Figure 6.11a), from nearly 50% of the area inside the Arctic Circle to about 30% for 2007 to 2010. The numbers of pixels classified as each phenoregion for the CAA region and the Arctic Ocean are also shown. The region is delineated following *Parkinson and Cavalieri* (2008). The black line on each panel shows the variation of the sum of percentages for phenoregion 1 to 3. The correlation coefficient between the sum of pixels labeled as 1 to 3 and the minimum sea ice extent for September all exceed 0.9 for the three regions considered, which is reasonable because phenoregion 1 to 3 are the area where ice survives the summer melt and generally represents the September monthly mean. Sea ice in the central Arctic is increasingly dominated by thin first year ice *Stroeve et al.* (2012). This can be demonstrated from our result. The percentages for phenoregion 4, 5 and 6 are increasing greatly for the 2007 to 2010 period for the Arctic Ocean (Figure 6.11b).

6.4.3 Phenoregion Anomaly Maps and Phenoregion Changes in Recent Years

The phenoregion maps of different years can be used for change detection. Due to the changes in the SIC melt profiles, an individual pixel belonging to one phenoregion in one year may belong to another phenoregion in another year. By comparing the class label of the same pixel from one year to another, we know whether a pixel changed its ice melt pattern. Thus, the geographic location and the degree of change can be mapped. Based on our definition of phenoregions, a pixels increasing classification label from one year to another year implies earlier melt, while a decreasing label indicates later melt. Here, all years are compared with the climatological mean and the anomaly maps are generated, shown in Figure 6.12 for selected years. Considering that the differences between two neighboring classes are quite small, pixels with a change of label of 0, -1 and 1 are shown in white, which means no change. Pixels with a change of class label of 2 or more are shown in red, indicating a sea ice trend toward earlier melt; while pixels with a change of class label smaller than -1 are shown in blue, indicating sea ice trend toward later melt. The darkness of the red/blue defines the magnitude of the change. Thus, areas shown in color are pixels with significant changes of ice melt pattern. From the anomaly maps, we find that the most striking declines occur in marginal ice zones and coastal regions. Moreover, ice in western Arctic melts much earlier than before, replacing perennial ice with annual sea ice types.

6.5 Discussion

Since the criteria used to define the phenoregions are subjective, it is impossible to evaluate the classification results using objective measures. Our classification results are evaluated by close visual inspection of the classification maps. First, phenoregions are homogeneous and the boundaries of the phenoregions are smooth and mainly follow the longitudinal zonation. Second, several locations stand out as earlier or later melt compared to other regions with the same latitude. This is influenced by local oceanographic conditions. For example, phenoregions in Baffin Bay area are developed around the north water polynya

and are influenced by the ocean currents. For the northern CAA, land blocking helps preserve the old ice. However, the warm Baffin Current makes ice in eastern Lancaster Sound melt much earlier than western Lancaster Sound. Third, adjacent regions on each side of Novaya Zemlya belong to totally different phenoregions because warm Atlantic Water can only arrive at the Barents Sea but not the Kara Sea. All of this evidence illustrates that the proposed clustering criteria are reasonable, and the classification results are logical.

Though each phenoregion is well defined, the thresholds used to separate the phenoregions in the decision tree classifier are subjectively selected. Thus, the boundaries of the phenoregions are not precise. Despite the limitations described above, this pilot study presents several previously undocumented findings. By advancing a decision tree classification that divides sea ice pixels into different phenoregions based on sea ice melt profile, we have established a framework to integrate high temporal resolution sea ice data for change detection at spatiotemporal information of the original data. Our results are also comparable to the ice age distribution of *Maslanik et al.* (2011). However, the ice age algorithm is developed for the Arctic Ocean (*Fowler et al.*, 2004).

6.6 Summary

Arctic sea ice cover has been shifting from MYI to seasonal ice in recent years. Direct measurement of ice age or ice thickness, which is typically required for an assessment of multi-year versus seasonal ice, is only available for selected areas in recent years. In this chapter, we present an innovative way of classifying the Arctic into seven classes using the ice phenology information inferred from the long time series of daily SIC data. Ice phenology in the Arctic region during melt season has different characteristics, including different timing of start of melt date and different duration of the melt. Based on these ice phenology profiles, a phenoregion map is developed by decision tree classification for each year in the study period. The yearly phenoregion maps exhibit significant variations from year to year, which set the foundation for change detection. By comparing the yearly phenoregion maps with the climatological mean map, yearly anomaly maps are

formed. The anomaly maps clearly show the areas where ice melts vary most dramatically. Compared to most of the studies that utilize one value to represent the entire sea ice region, the current analysis at the pixel scale provides detailed spatial information of Arctic sea ice change. This analysis also provides a new way of visualizing the daily sea ice data. By integrating key sea ice retreat information of a year into a single map, these yearly phenoregion maps present the spatial and temporal distribution of sea ice retreat patterns. The understanding of sea ice retreat is much more comprehensive when compared to analysis only using a monthly or seasonal means of SIC.

Chapter 7

Relationship between Surface Radiation and Sea Ice Spring and Summer Retreat

7.1 Introduction

A positive Arctic Oscillation (AO) during the late 1980s and early 1990s (Figure 7.1) is believed to be the main driver of increasing sea ice loss during that period, but the continuing decline of sea ice during a near-neutral phase of AO after the mid-1990s suggests that anomalies in the surface energy balance, rather than wind stress anomalies, may now have an increasing influence on ice extent (*Perovich et al.*, 2007b). Even though the AO turned strongly negative in winter of 2009/2010, the summer of 2010 was a low ice year and this has been attributed to the pronounced differences in atmospheric circulation during winter 2009/2010 compared to the mean anomaly pattern based on past negative AO events (*Stroeve et al.*, 2011). Roughly only 50% of the sea level pressure (SLP) variability can be explaineded by AO (*Rigor et al.*, 2002). The role of SLP in the low sea ice year of 2007 for the CAA region has been examined in *Howell et al.* (2009) and they found that anomalously high SLP over the Beaufort Sea in August and September 2007 prevented MYI into the CAA channels. The loss of Arctic sea ice in recent years has been attributed

to the changing atmospheric circulation patterns (*Overland et al.*, 2012) and to the increase of solar heat input to the Arctic ice-ocean system due to albedo feedback (*Perovich et al.*, 2011a). Currently, there is no consensus that exists as to the primary causes.

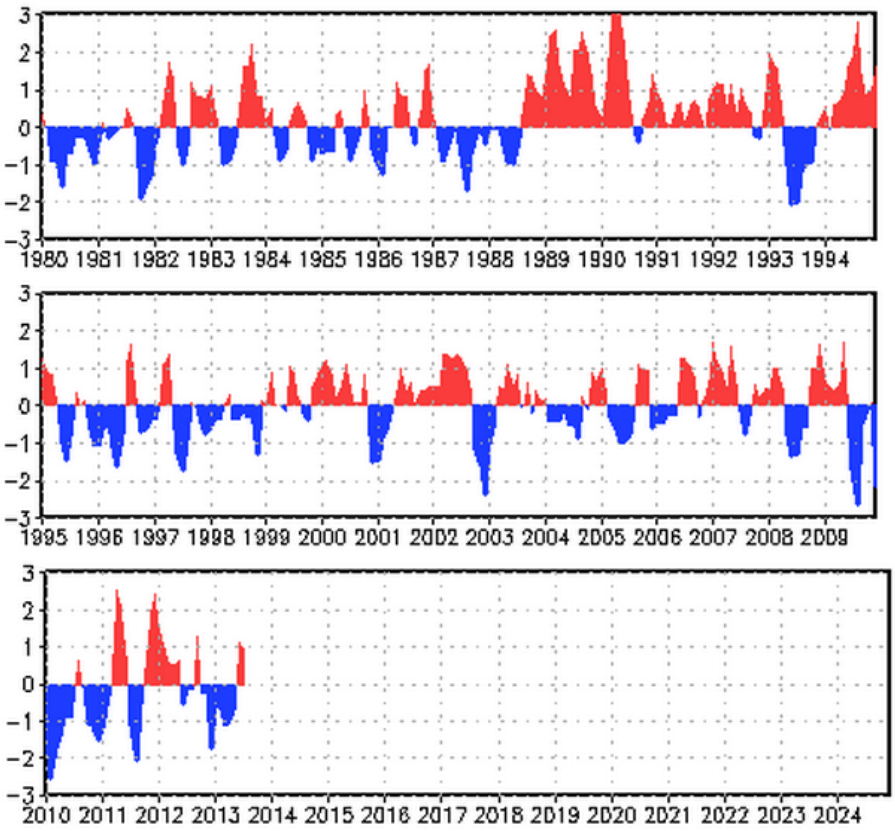

Figure 7.1: Standardized 3-month running mean AO index from 1980 to 2013. Adapted from Climate Prediction Center, National Weather Service. `http://www.cpc.ncep.noaa.gov/products/precip/CWlink/daily_ao_index/month_ao_index.shtml`

Since sea ice is already thin in recent years and thin ice takes less energy to melt, spatial extent of sea ice may be more vulnerable to anomalies in the surface energy balance. The amount of energy absorbed by the ice-ocean system is very important, because a small change in the surface energy balance can lead to dramatic changes in the surface (*Sedlar et al.*, 2011). The understanding of the interaction between solar radiation and sea ice

cover is key to the determination of the cause of sea ice melt according to many studies (*Inoue et al.*, 2008, *Itoh et al.*, 2011, *Nicolaus et al.*, 2010). In summer, the ice surface starts to melt and remains near 0 °C at all times because of the ubiquitous presence of melting ice. Summer surface air temperature over the Arctic Ocean remains close to freezing, and the flux of sensible heat from the atmosphere to the ice is small. The net radiation is primarily used to melt ice and replenish the ocean's heat reservoir through ice-free open water (*Serreze and Barry*, 2005). Thus, the relationship between surface radiation flux and sea ice retreat in the spring and summer is investigated in this chapter.

The linkages between melt season duration, the amount of solar energy absorbed into the ice-ocean system, and successive seasonal declines in sea ice volume through enhanced sea-ice-albedo feedback, have been investigated by *Perovich et al.* (2007a). They found that the total energy absorbed is more strongly related to the timing of melt onset than to the duration of melt or freeze onset. Due to larger values of incident solar energy in May and June, the increase in cumulative solar energy absorbed for each day that melt starts earlier is much larger than that for a one-day delay at freeze up. Thus, a day of melting in the spring has much greater impact than a day in late summer. The fact that melt onset date has great impact on total solar input suggests that storms and warm air masses in late spring may have great influence by triggering the onset of melt (*Bitz et al.*, 1996). The 2007 lowest sea ice extent from 1979 to 2010 has caught much attention. Clearer skies and reduced cloudiness and the consequent increase in downward shortwave radiation at the surface enhanced surface melting of the ice in the Arctic Ocean in 2007 (*Kay et al.*, 2008). However, *Nussbaumer and Pinker* (2012) showed that in 2007 in the Arctic Ocean the lowest cloud fraction and largest downwelling surface shortwave occurred over a region that showed positive or no SIC anomaly, but not over the region that exhibits the strongest signal of sea ice anomaly. Clearly, there is still much to understand.

The decrease in sea ice extent and the longer melt season lead to increased solar heat input into the Arctic ice-ocean system because the decrease of surface albedo after melt (*Perovich et al.*, 2011a). Subsequently, the thinning of the Arctic sea ice allows for larger coverage of FYI melt ponds, which allows more shortwave radiation transmitted through the sea ice to the Arctic Ocean (*Nicolaus et al.*, 2012). The solar heat input into the ocean accelerates melt on the bottom of the ice (*Perovich et al.*, 2008). However, the decreased

sea ice extent also increases the fall-winter energy loss from the Arctic Ocean (*Screen and Simmonds*, 2010).

The summer sea ice decreases in the CAA have been attributed to the increase in spring air temperature (*Tivy et al.*, 2011). Since many processes affect surface temperature, focusing on this parameter provides little understanding of the physical mechanisms that govern these temperature changes. The examination of various terms in the surface radiation balance may provide direct quantitative linkages to the mechanisms producing seasonal transitions in SIC. Using ERA-interim data, *Kapsch et al.* (2013) concluded that the greenhouse effect associated with clouds and water vapour in spring is crucial to determine the end of summer Arctic sea ice extent. In years with below normal end of summer sea ice extent, a significantly enhanced transport of humid air is evident during spring into the region where the ice retreat is encountered. This enhanced transport of humid air leads to increased cloudiness and humidity, and further leads to larger than normal longwave radiation downward at the surface in spring. In the mean time, the increase in cloud cover also decrease the shortwave radiation downward at the surface as large amount of shortwave radiation is reflected by the cloud.

The focus of this chapter is to determine the variability of radiation fluxes at temporal scales that include short-term variability on a daily basis, seasonal variability, and interannual variability. Using radiation data from the recent reanalysis project ERA-interim, the following objectives are defined to understand the causal linkages between surface radiation and the sea ice in this chapter:

- to provide an explicit description of the temporal dynamics of the daily surface radiation for the CAA region during spring and summer months,
- to investigate the relationship between the timing of the key days for each of the sea ice melt phases and the amount of cumulated radiation in the spring and summer months for that year,
- to identify the role of each of the radiation fluxes in contributing to the available energy to the sea ice melt process.

7.2 Data and Methods

For this chapter, radiation data at the surface are obtained, including net shortwave radiation, net longwave radiation, shortwave radiation downwards and longwave radiation downwards. The top of atmosphere (TOA) shortwave radiation is also obtained and used. The radiative data are accumulated forecast parameters, and they are archived at time steps of 3-, 6-, 9- or 12-h. The data values at forecast time 00:00:00 and 12:00:00 are obtained each day, both have accumulated for 12 hours (step=12). The daily mean values (w/m^2) are obtained by summing the values at forecast time 00:00:00 and 12:00:00 and divided by 24 hours, which are the averaged values at 12-h for midday and midnight. All data are downloaded from the ECMWF Research Data Server (`http://data-portal.ecmwf.int/data/d/interim_daily/`). Daily net radiation values are calculated based on daily mean net shortwave/longwave radiation for all grid values in the CAA region from April to September each year. Daily surface radiation fluxes from ERA-Interim reanalysis are used to explore the relationship between sea ice retreat and the cumulative surface radiation balance.

7.3 Results

7.3.1 Temporal Evolution of the Daily Surface Radiation

The seasonal cycles of individual components of the surface radiation flux are defined as the climatological mean of the daily radiation fluxes for the period of 1989 to 2010, shown in Figure 7.2, including shortwave radiation downward and net shortwave radiation (red), and longwave radiation downward and net longwave radiation (blue), and net radiation (black). Daily sea ice change (magenta line) is also shown in Figure 7.2, as a reference. The seasonal cycle shown is consistent with previous climatologies (*Lindsay*, 1998). However, there are large variabilities in these daily fluxes; the variance of each radiation flux is shown in Figure 7.3. Here, the variance represents interannual variability of the daily mean radiation flux values.

Driven by solar incident angle, shortwave radiation downward (K↓) has a seasonal cycle. It increases from 95 W/m^2 at the beginning of April to its maximum value of 286 W/m^2 in middle June. After that, K↓ decreases gradually to 90 W/m^2 at the end of September. K↓ varied considerably by day. The magnitude of the variance of K↓ changes through the season. The largest variation of K↓ is in the middle summer. The day-to-day variation of K↓ is determined mainly by the cloud cover. Net shortwave radiation (K^*) increases from 30 W/m^2 to 145 W/m^2 in early July and then decreases to 57 W/m^2 by the end of September. K^* is controlled by the magnitude of K↓, and surface albedo. For the CAA region, as sea ice melts, the albedo of the surface decreases and K^* increases.

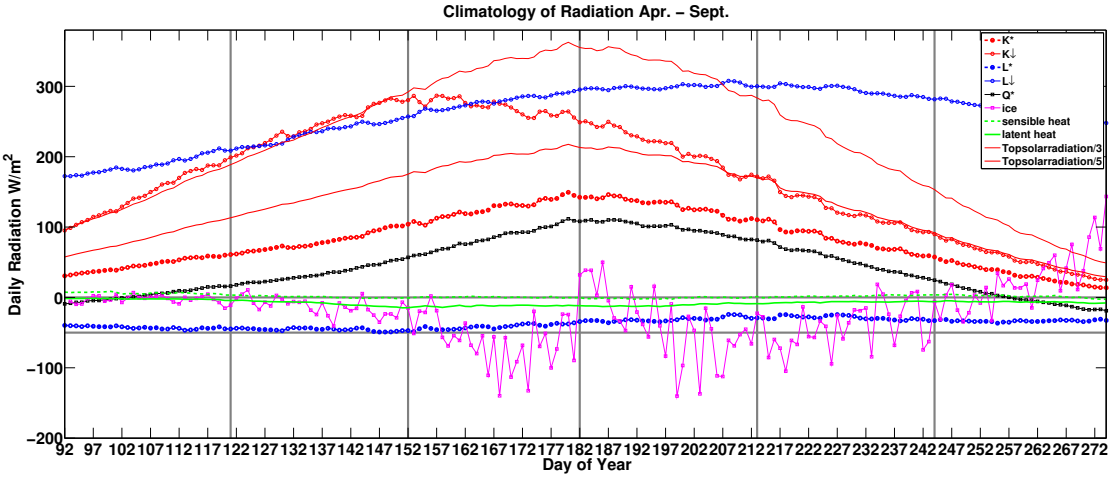

Figure 7.2: The climatology of surface radiation for the Canadian Arctic from April to September between 1989 and 2010.

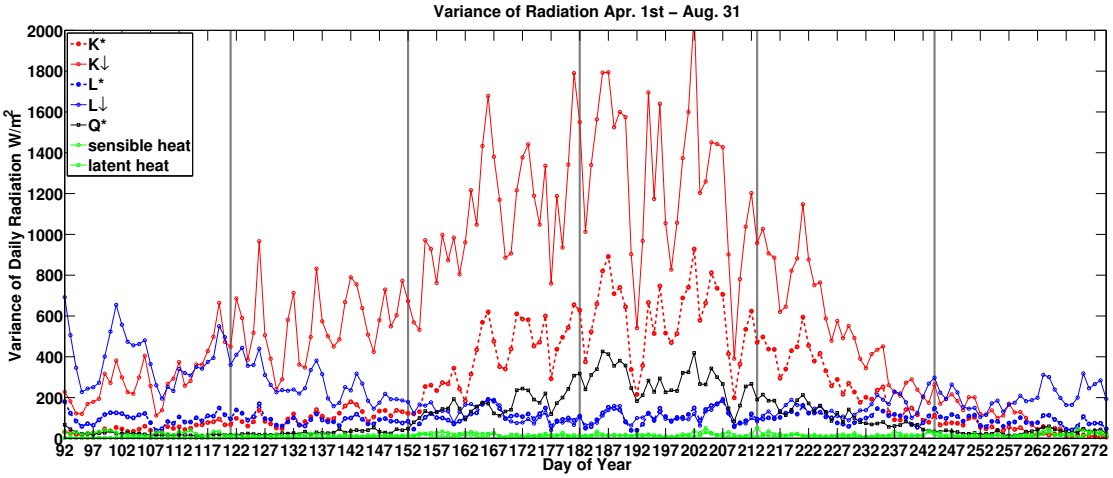

Figure 7.3: Variance of each surface radiation for the Canadian Arctic from April to September between 1989 and 2010.

Longwave radiation downward (L↓) increases from 180 W/m^2 in early April to 300 W/m^2 in middle July. L↓ rises quickly in April and May, and then stayed at that level for a few months. L↓ depends mainly on atmospheric temperature, the water vapour content of the atmosphere, and cloud cover. L↓ increases with air temperature. The maximum value of L↓ is reached in late July when air temperature is the highest of a year. L↓ has relatively small variation in summer, and has extremely large daily variation in the spring (Figure 7.3). Longwave radiation upward (L↑) is the outgoing longwave radiation. L↑ on ice mainly depends on surface emissivity and ice surface temperature. Net longwave radiation (L^*) is quite stable with very little variation (close to 50 w/m^2 loss from the surface) from April to September.

Net radiation (Q^*) is -10 W/m^2 in early April. It reaches its maximum of 107 W/m^2 in July, and then it decreases to 25 W/m^2 by the end of September. Q^* shows a reversal from negative to positive values at the beginning of April. The change of Q^* is mainly controlled by the change of net shortwave radiation K^* and net longwave radiation L^*. Net longwave radiation loss exceeds or balances solar radiation gains by the surface, resulting in a negative, or only slightly positive radiation balance in April. As summer progresses, K↓ increases dramatically, and net radiation becomes positive and increases very quickly.

7.3.2 The Changes in K↓ in phase 2 and 3 during Melt Pond

The climatological mean shortwave radiation at the top of atmosphere (TOA) and the shortwave radiation downward at the surface are illustrated in Figure 7.2. During sea ice retreat phase 1, the shortwave radiation downward at the surface is approximately one-third (33%) of that at TOA. However, there is a significant drop in the percentage of the TOA shortwave radiation that reaches the surface during sea ice retreat phase 2 and phase 3. The sea ice retreat phases are defined in Chapter 4. Beginning from phase 4, the shortwave radiation downward at the surface is approximately 20% of that at TOA. The percentage of shortwave radiation at TOA that reaches the surface, namely the aerial albedo, increases from 0.67 to 0.8 during the melt pond and pond drainage period. Similar results has been reported in *Shupe and Intrieri* (2004), *Inoue et al.* (2005) for the central Arctic after middle summer, but the decrease in percentage of the shortwave radiation at TOA that reaches the surface is from 50% to 33%. The difference in the exact percentage is a consequence of different study areas that were used in the two investigation.

High albedo snow and ice areas cause multiple reflections between the atmosphere (particularly clouds) and the surface (*Shine*, 1984). However, with the formation of melt pond on sea ice surface during the spring and summer melt, this multiple reflection has been greatly reduced due to the formation of low albedo water areas on sea ice surface. With the lack of multiple reflection during sea ice retreat phase 2 and phase 3, the percentage of the TOA shortwave radiation that reaches the surface is greatly decreased. Based on ERA-interim data used, this decrease in percentage is from 33% to 20% for the CAA region. Thus, the change in the percentage of the TOA shortwave radiation that reaches the surface is caused by the formation of melt ponds at the surface and can be attributed to the lack of multiple reflections due to the melt pond period.

7.3.3 The Start of Phase 2 and Surface Radiation Flux

Large interannual variations have been observed at the onset of melt within the CAA region, but the mechanisms that trigger the melt onset are not well understood. The following are the possible causes of the melt onset:

1. The heat influx from southerly latitudes, or from warmer terrestrial surfaces. The role of sensible heat in initiating sea ice melt through regional-scale synoptic atmospheric circulation patterns has been proposed in *Agnew and Silis* (1995). However, sensible heat flux can act to support or counteract the effect of net radiation, depending on the characteristics of the near surface atmosphere.

2. Longwave warming effect of clouds. The relative roles of wind, radiative forcing and advected heat in explaining variability in the ice edge are quite distinct for different Arctic regions (*Francis et al.*, 2005). Their analysis found that longwave radiation downward during spring-summer period accounts for approximately 40% of the variability in perennial ice extent from 1979 to 2004. *Francis and Hunter* (2006) further showed that the position of the summer ice edge was affected by springtime longwave radiation downward, which was further controlled by cloud cover and water vapour. *Maksimovich and Vihma* (2012) found that the anomaly of the surface net heat flux 1-7 days prior to snow melt onset (SMO) explained up to 65% of the interannual variance in SMO in the central Arctic, while downward longwave radiation explained up to 90% of SMO variance within the western central Arctic.

3. Increased global radiation under reduced cloud cover conditions is a potentially effective factor for initiating ice melt (*Kay et al.*, 2008).

All of the above processes can occur in tandem during the spring period. It is a challenge to identify the relative importance of these factors and which (or which combination) of these is most effective at triggering the melt process.

The relationships between cumulative surface radiation, including shortwave radiation downward, longwave radiation downward, net longwave radiation, and the start of phase 2 as defined in Chapter 4 based on SSM/I SIC data are investigated. The start of phase 2 often occurred in late May or early June, with approximately 10 days variation between different years (refer to Table 4.2). Three cumulative methods are considered here:

1. cumulative radiation for 10 days before the start of phase 2.

2. cumulative radiation for 30 days before the start of phase 2.

3. cumulative radiation for April and May.

The anomalies of the surface radiation are used instead of the actual values to avoid any trend in the radiation. The correlation coefficients and the corresponding p-values are reported in Table 7.1. Generally, the downward shortwave radiation anomaly is negatively related with the start of phase 2. The larger the downward shortwave radiation anomaly, the earlier the phase 2 will start. The longwave radiation downward anomaly and the net longwave radiation anomaly are negatively related to the start of phase 2. However, none of these relationships are statistically significant at the 0.05 level.

For the study area of Arctic Ocean, *Kapsch et al.* (2013) concluded that years with lower than normal end-of-summer sea ice extent were accompanied by larger than normal longwave radiation downward in the spring season. Even though we tried three different definitions of cumulative longwave radiation downward, no statistically significant connection is found between summer sea ice loss and spring longwave radiation downward for the CAA region for the 22-year study period. However, this relation does hold for certain years. For example, 1998 is a low ice year with large cumulative radiation for the 30 days before the start of phase 2, and year 1997 is a high ice year with small cumulative radiation for the 30 days before the start of phase 2.

Table 7.1: Correlation (r) and p value (p) between date of phase 2 and cumulative radiation anomaly.

		K↓	K*	L↓	L*
10 days before phase 2	r	-0.14	0.16	-0.24	-0.32
	p	0.55	0.49	0.27	0.15
30 days before phase 2	r	-0.33	0.07	-0.11	-0.33
	p	0.13	0.77	0.63	0.13
Apr.-May	r	-0.08	0.11	-0.12	-0.21
	p	0.73	0.63	0.58	0.35

7.3.4 Interannual Variation of Surface Radiation and Sea Ice Loss

The individual components of surface radiation flux have large interannual variability. The correlation between the sum of net radiation from April to September each year and the yearly sea ice loss for the same months is 0.61. However, considering that the calculation of net radiation relies on the sea ice concentration dataset in the ERA-interim and includes some feedback in logic, the investigation of shortwave and longwave radiation downward and their relation with the sea loss may be more meaningful. The correlation between longwave radiation downward only and sea ice loss is 0.59 (Figure 7.4), which is statistically significant at the 0.05 level. The correlation between shortwave radiation downward and sea ice loss is 0.30 (Figure 7.5). These numbers indicate that the relative role of each energy term in each year is different. In some years, the shortwave radiation may play a driving role; while in other years, the longwave radiation may be more important to understanding the total variance structure.

As shown in Figure 7.4, year 1998, 2006 and 2010 have larger than normal cumulative longwave radiation and large sea ice loss for the 6 month period; while year 1992 and 1997 have smaller than normal cumulative longwave radiation and small sea ice loss for the 6 month period. However, this relationship is not hold for 1999 and 2004.

As shown in Figure 7.5, the cumulative shortwave radiation downward in the four large ice loss years (1998, 1999, 2006 and 2010) were smaller than the two small ice loss years (1992 and 1997). This is consistent with *Kapsch et al.* (2013) that years with lower than normal end-of-summer sea ice extent were accompanied by smaller than normal cumulative shortwave radiation downward at the surface. However, this connection is not statistically significant for the CAA region for the 22-year study period. As shown in Figure 7.5, year 2004 was a high ice year with extremely low cumulative shortwave radiation downward. Thus, we conclude that the connection between summer ice loss and cumulative shortwave radiation only holds for certain years.

Table 7.2: Correlation (r) and p-value (p) between yearly ice loss and cumulative radiation.

		K↓	K*	L↓	L*	Q*
Apr.-May	r	-0.1	-0.20	0.30	0.40	0.17
	p	0.64	0.36	0.16	0.07	0.45
Apr.-Sept.	r	0.30	0.02	0.26	**0.59**	**0.61**
	p	0.18	0.93	0.23	0.004	0.003

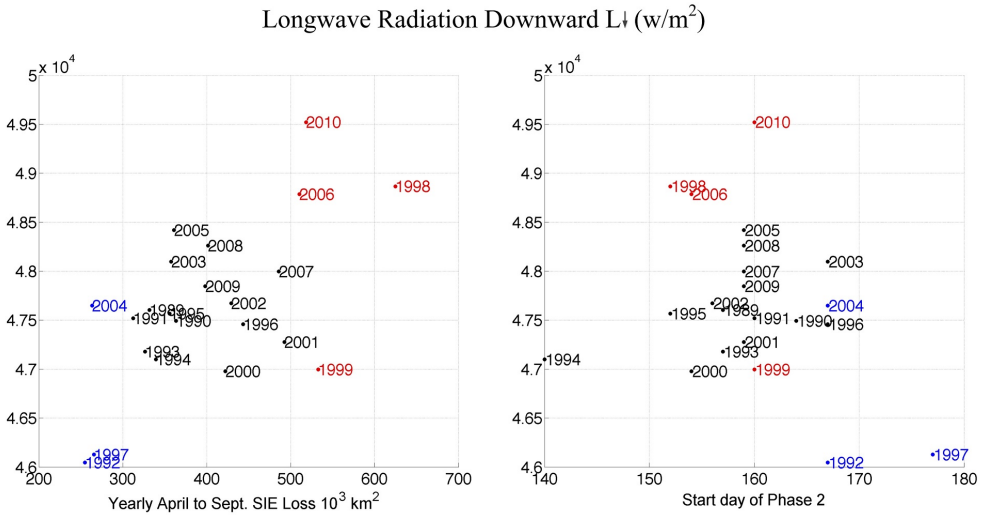

Figure 7.4: Scatterplot of cumulative longwave radiation downward and (a) yearly ice loss, both for April to September, (b) the start day of phase 2. Years with large and small ice loss identified in Table 4.1 are shown as red and blue, respectively.

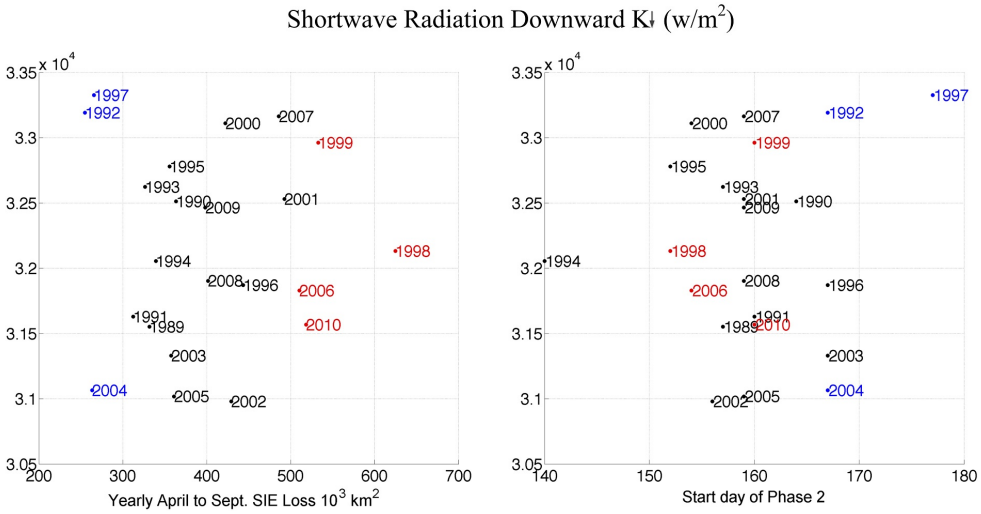

Figure 7.5: Scatterplot of cumulative shortwave radiation downward and (a) yearly ice loss, both for April to September, (b) the start day of phase 2. Years with large and small ice loss identified in Table 4.1 are shown as red and blue, respectively.

7.3.5 Daily Radiation Anomalies for Different Years

After the examination of the cumulative radiation for each radiation component for the six months period, we did not find any clear clues that indicate whether any particular radiation term is unique in forcing sea ice variability in the CAA region. In the section, we explore the daily progression of each radiation term through the months from April to September. As described in chapter 3, since ERA-interim radiation values are largely unvalidated, therefore daily anomalies instead of absolute values are used to investigate the differences between different years. For each year, the daily radiation anomalies are calculated by subtracting the daily climatological mean from the daily values. The daily progression of the surface radiation anomalies for 1998, 2004 and 2007 are shown in Figure 7.6.

The cause of the large sea ice loss may be driven by the atmosphere either through changes in downward shortwave or longwave radiation. Clouds affect the surface radiation budget in a conflicting fashion by decreasing the solar radiation and increasing the incoming

longwave radiation in summer. Which of these two effects dominates depends on the type of cloud cover present (*Intrieri et al.*, 2002, *Persson et al.*, 2002, *Uttal et al.*, 2002). In Figure 7.6 and Figure 7.7, it can be seen that the anomalies of shortwave radiation downward and the anomalies of longwave radiation downward generally have the opposite sign. This is believed to be related to the effect of clouds as noted above, as the presence of cloud can enhance the longwave radiation downward. In the mean time, the presence of cloud also reflect more solar radiation into the space and thus lead to less shortwave radiation at the surface. The sign of the net radiation anomalies depend on which of the two factors dominates the balance.

The causes of the two low ice years in 1998 and 2007 are quite different. In 1998, the longwave radiation downward was much larger than the climatological mean from April to June, as indicated by the positive anomalies of longwave radiation downward shown in Figure 7.6. The abnormally high temperature in spring and early summer of 1998 is consistent with higher than normal longwave radiation downward. Even though shortwave radiation anomalies counteracted the longwave radiation anomalies, the net radiation was higher than normal from middle May to September in 1998. However, in 2007, the shortwave radiation downward was much larger than the climatological mean from late April to early June, as indicated by the positive anomalies of shortwave radiation downward shown in Figure 7.6. It can be seen that shortwave radiation anomalies counteracted the longwave radiation, but net radiation was close to the climatological mean in April and May. In June 2007, the net radiation even became below normal. However, the net radiation anomalies turned positive since July 2007, largely due to strong shortwave radiation downward. This positive phase of net radiation lasted into September. For the Arctic Ocean, the larger than normal shortwave radiation downward was caused by unusual clear sky (*Kay et al.*, 2008). Unusual clear skies might also be evident for the CAA region in 2007, but this fact needs further confirmation by other data.

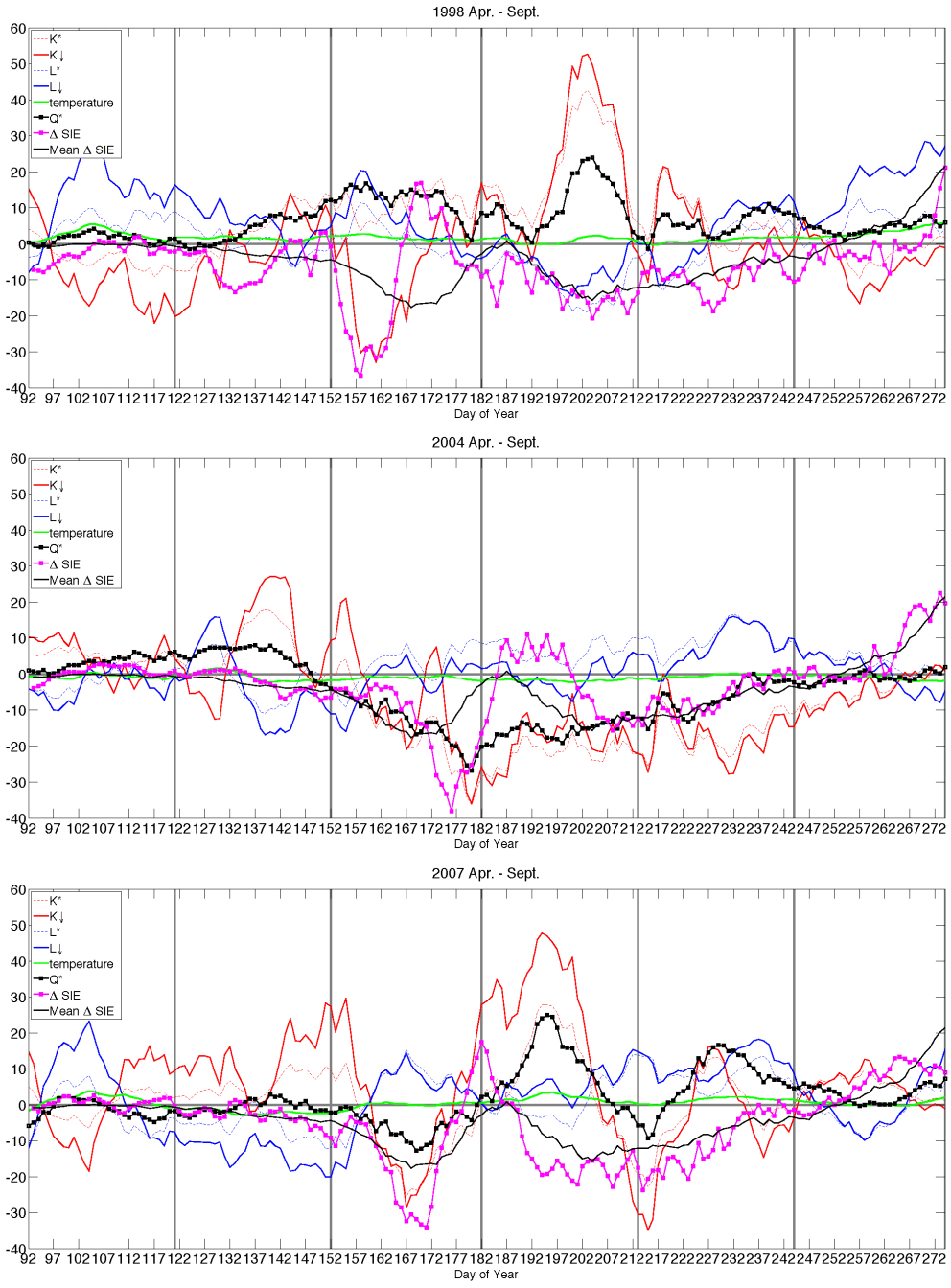

Figure 7.6: The surface radiation anomaly and sea ice daily change for the Canadian Arctic from April to September for (a) 1998, (b) 2004, and (c) 2007.

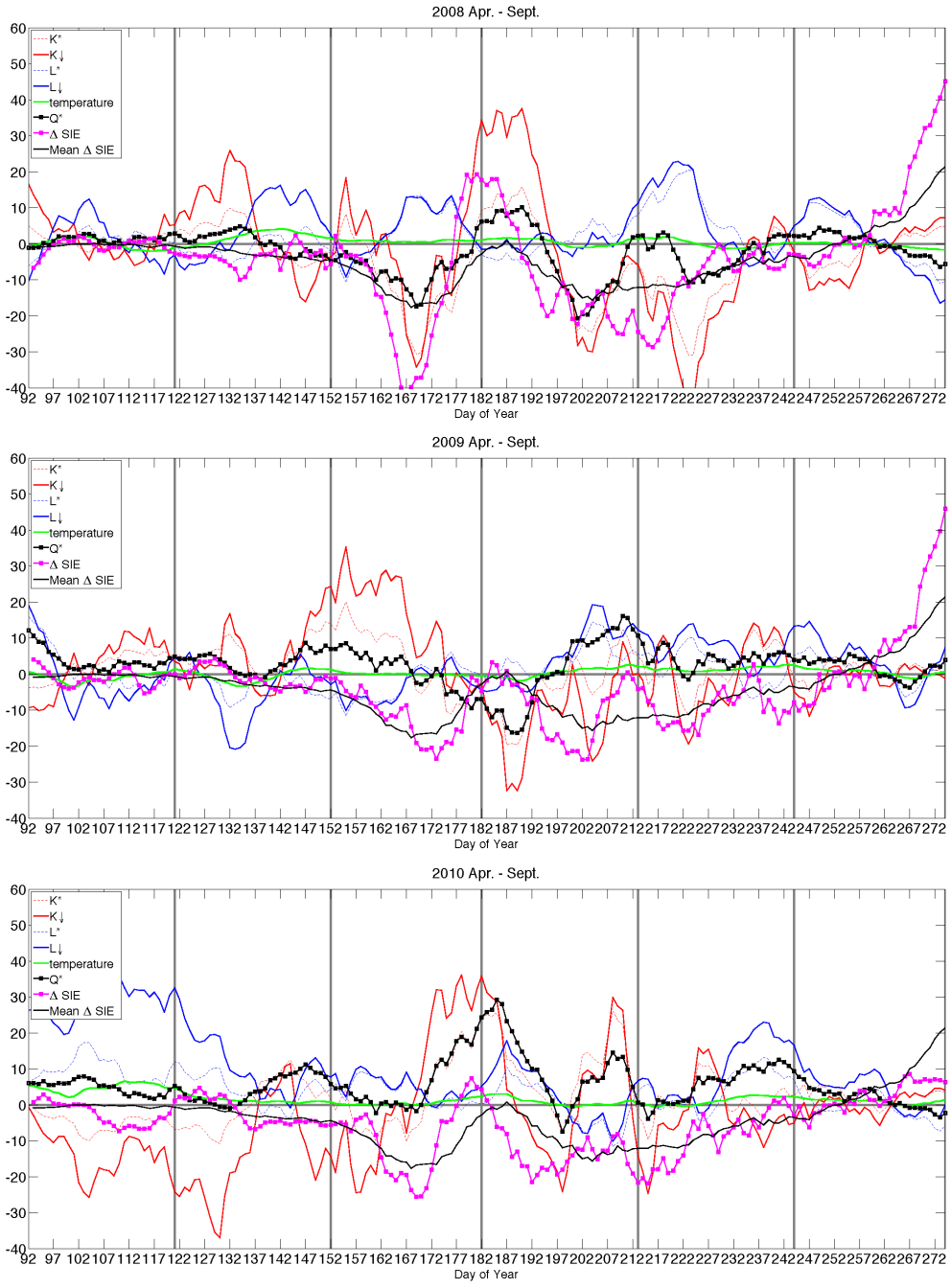

Figure 7.7: The surface radiation anomaly and sea ice daily change for the Canadian Arctic from April to September for (a) 2008, (b) 2009, and (c) 2010.

In 2004, the shortwave radiation downward was lower than the climatological mean from June to September. The longwave radiation downward and net longwave radiation were all close to the climatological mean, especially during June and July. Thus, the unusually high ice concentration in 2004 may partly caused by the lack of the shortwave radiation downward. It is speculated that the extremely low shortwave radiation downward from June to September in 2004 is related to higher than normal cloud cover in the region, but further inspection is needed to confirm the process.

The daily progression of radiation anomalies for the most recent three years in this study, year 2008 to 2010, are shown in Figure 7.7. Year 2008 was characterized as having lower than normal net radiation especially from late July to September, but 2008 was a year with relatively low ice cover for the CAA region. Year 2009 had larger than normal shortwave radiation downward from April to June, which was quite similar to year 2007. Year 2010 is another low ice year for the CAA region. From May to middle July, year 2010 had larger than normal longwave radiation downward anomalies, which was quite similar to the situation in year 1998. Thus, part of the reason for the 2010 low may also caused by warm air moving into the CAA region in April and May.

Based on the above analysis, it can be concluded that the reasons for high or low ice years in the CAA region can not be explained solely by surface radiation anomalies. Along with surface radiation anomalies, other factors including atmospheric circulation and sea ice dynamics are also important in regulating sea ice melt in the CAA region. These factors need to be addressed in future studies.

7.4 Summary

Using ERA-interim surface radiation data, we described the temporal dynamics of the daily surface radiation components during spring and summer months in the CAA region. Shortwave radiation increases from April to middle June and then decreases, while longwave radiation increases from April to July as the surface air temperature increases. The presence of melt pond on ice surface during sea ice retreat phase 2 and phase 3 is found to influence the percentage of the TOA shortwave radiation that reaches the surface, due

to the lack of multiple reflection between the surface and the atmosphere over low albedo melt pond areas.

The relationships between cumulative surface radiation components, including shortwave radiation downward, longwave radiation downward, net longwave radiation, and the start of phase 2 are investigated. Generally, cumulative downward shortwave radiation anomaly is negatively related with the start of phase 2. The larger the downward shortwave radiation anomaly, the earlier phase 2 starts. The cumulative longwave radiation downward anomaly and cumulative net longwave radiation anomaly are negatively related to the start of phase 2. However, none of these relationships are statistically significant at the 0.05 level.

The sum of each of the radiation terms at the surface for the six-month interval (April to September) has been correlated with the total sea ice loss for corresponding years. We found that the correlations are not very high, suggesting that the role of each radiation factor in forcing sea ice maybe quite different from year to year. The progression of daily radiation anomalies in three extreme ice years (1998, 2004 and 2007) are investigated. Year 1998 is characterized by extremely high downward longwave radiation, while 2007 is characterized by extremely high shortwave radiation. Year 2004 is featured as a negative downward shortwave radiation year. The progression of daily radiation anomalies for the most recent three years in the 22-year study period are also analyzed. However, the surface radiation anomalies can only partly explain the high or low sea ice years in the CAA region, it is recommended that the roles of other factors including atmospheric circulation and sea ice dynamics should also be studied in future research.

Chapter 8

Summary and Outlook

The overall objective of this research was to utilize daily passive microwave sea ice concentration data for the purposes of studying sea ice retreat processes in the CAA and to contribute to the understanding of the cause of sea ice retreat on the climate. A summary of the research and achievements toward this objective is the subject of section 1. The limitation of this study is discussed in section 2. The thesis is concluded with an outline on potential directions for future research in section 3.

8.1 Summary of Research

8.1.1 Sea Ice Retreat Processes in the CAA

In chapter 4, we have presented for the first time a detailed analysis of the daily sea ice changes in spring and summer retreat in the CAA using passive microwave data. The daily SIE and ΔSIE are calculated using a passive microwave dataset for each spring and summer from 1989 to 2010. We analyzed the daily ΔSIE for each individual year and found that the sea ice retreat in the CAA can be defined as a four phase process: a slow ice melt phase that usually lasts until early June; a quick ice melt phase with large daily ΔSIE which lasts about half-a-month; a slow sea ice melt or even a small ice increase phase which lasts

another half-a-month; and a steady ice decrease phase. The daily ΔSIE for different phases from all years are significantly different based on Kolmogorov-Smirnov (K-S) test, which confirmed that the proposed criteria to identify different phases are reasonable. The four-phase pattern occurred for most of the years from 1989 to 2010. The four-phase pattern in different years have several common characteristics. The years with large sea ice loss have earlier inception of phase 2 and phase 3; while years with small sea ice loss have later inception of phase 2 and phase 3. This pattern leads to the significant observation that the start date of phase 2 can be used as a key factor to determine the amount of ice melt for a season.

Considering the width of the waterways in the CAA, the 25 km pixel size for passive microwave SIC product is unable to provide detailed sea ice information. To facilitate the understanding of the process during each sea ice retreat phase with more spatial detail, we used the daily MODIS IST product with a spatial resolution of 4 km by 4 km. Though available each day, a large percentage of the MODIS IST image is cloud covered and only the cloud-free areas can be used. Even with the limitation, we are able to find a few images that are cloud-free in the CAA region during each of the sea ice retreat phases. Based on the common characteristics of the daily ΔSIE time series in different years, and with the assistance of MODIS melt pond fraction and IST products, we concluded that the four-phase sea ice melt pattern is actually a ice slow-melt phase, a melt ponding phase, followed by a pond-drainage phase, and then real breakup and advanced melt. The melt in April is slow but large amounts of net radiation are absorbed by the surface. Subsequently, melts accelerate at some point, with increased coverage of melt pond. The area of melt pond increases as ice continues to melt. In phase 2, sea ice concentration is underestimated because melt pond has been falsely identified as open water by passive microwave. In phase 3, melt ponds start to drain. The slow ice decreases and sometimes even some apparent ice increase in phase 3 are mainly caused by melt pond drainage. In phase 4, ice continues to melt, with ice import from the Arctic Ocean in August and September.

In summary, the sea ice retreat in the CAA region is a four-phase process, a slow ice melt phase, a melt ponding phase, a pond drainage phase, and a further melt phase with sea ice flux between neighbouring regions .

8.1.2 Improved SIC Estimation with MODIS Ice Surface Temperature

In chapter 5, we explored the possibility of improving the sea ice concentration estimation using data fusion and data assimilation techniques. Sea ice concentration data derived from passive microwave brightness temperature have large uncertainties during the sea ice melt period. We presented the benefits of combining SSM/I sea ice concentration data with MODIS ice surface temperature data to get better estimates of sea ice concentrations during the summer sea ice melt. A simplified variational data assimilation system is used and sea ice concentration analysis is produced each day by the system. The system is updated each day by assimilating both SSM/I ice concentration and MODIS ice surface temperature. The daily ice concentration analysis is validated using the NOAA IMS sea ice extent product. For the CAA region, the SSM/I product agrees with the IMS product very well until mid July. After that, the SSM/I data quality degrades greatly, which correspond to the ice melt period in the CAA. The assimilation of MODIS data is shown to improve the total proportion correct by 5% to 10% in the CAA region during the melt. Compared to the original SSM/I data, more ice pixels have been correctly identified as ice in the analysis. The analysis improves the ice estimation by identifying more ice pixels during melt, while the estimation of water does not change much.

The daily SIE and daily ΔSIE curves based on the SSM/I SIC and the ice analysis results from June to August in 2007 are both examined. We found that the curves are smoother for the ice analysis than the curves that only use SSM/I data. The data assimilation results are shown for three selected days from phase 2, 3 and 4 of the ice retreat pattern for 2007. For the selected day in phase 2, the ice data increment map indicates that ice analysis has increased the original ice concentration for most part of the CAA. For the selected day in phase 3, the ice data increment map indicates that ice analysis has decreased the original ice concentration for most part of the CAA. For the selected day in phase 4, the ice data increment map indicates that ice analysis has increased the original ice concentration in most of the CAA. In summary, during the large ice decrease phase in late June (phase 2), melt pond form in the CAA region and SSM/I underestimate the sea ice concentration, the ice concentration analysis corrects this underestimation by

increasing the sea ice concentration. In early July, because of melt pond drainage (phase 3), the SSM/I data show a few days with ice concentration increase due to pond drainage. The sea ice concentration analysis is smaller than the original SSM/I data. In late July (phase 4), sea ice gradually decreases and the analysis increase the ice concentration from the SSM/I ice concentration. Thus, the proposed method is effective in improving the SSM/I sea ice concentration estimation by bringing in ancillary information.

8.1.3 Arctic Wide Sea Ice Retreat Patterns

In chapter 6, we connected the sea ice retreat patterns in the CAA with other high Arctic regions. Locations that have highly correlated daily ΔSIE profiles are highlighted using One-Point Correlation Maps. Through these correlation maps, we identified four most representative patterns for ΔSIE. By defining several key sea ice phenological parameters for each of the sea ice retreat patterns, the yearly sea ice profiles for all the pixels from all the years are classified into several classes using a decision tree classifier. Thus, a classification map is produced each year with several phenoregions. These yearly classification maps are then used as a basis for the sea ice change detection. For the same geographic location, if it is labeled as one phenoregion in one year and labeled as another phenoregion in another year, change detection is achieved by comparing the classification map of different years. Anomaly maps are produced to map and contrast the spatial locations of the changes.

8.1.4 Possible Cause of Sea Ice Retreat in the CAA

In chapter 7, we examined the daily progression of surface radiation flux in the CAA region. Firstly, using ERA-interim surface radiation data, we described the temporal dynamics of the daily surface radiation, including shortwave and longwave radiation, and net longwave radiation during spring and summer months in the CAA. Shortwave radiation increases from April until it reaches the maximum value in middle June and then decreases, while longwave radiation increases from April until it reaches the maximum value in July.

Secondly, the presence of melt pond on ice surface during sea ice retreat phase 2 and phase 3 is found to influence the percentage of the TOA shortwave radiation that reaches

the surface, due to the lack of multiple reflection between the surface and the atmosphere over low albedo melt pond areas.

Thirdly, the relationships between the start of phase 2 and cumulative surface radiation, including shortwave radiation downward, longwave radiation downward, net longwave radiation, are investigated. The longwave radiation downward anomaly and net longwave radiation anomaly are negatively related to the start of phase 2. Years with large cumulative downward longwave radiation anomalies starts phase 2 earlier. However, none of these relationship are statistically significant at the 0.05 level.

Lastly, the role of each radiation term in forcing sea ice change is quite different from year to year. In 1998, the longwave radiation downward was much larger than the climatological mean from April to June. However, the shortwave radiation downward was much larger than the climatological mean from late April to early June in 2007. No statistically significant relationship is found between the cumulative surface radiation, including shortwave radiation downward, longwave radiation downward, net longwave radiation, and the start of phase 2 or the total sea ice loss from April to September. The sea ice concentration and extent are used in this investigation, we suspect that there might be better correlation between surface radiation balance and ice volume. With ice thickness information, ice volume can be calculated. Ice thickness depends greatly on the energy balance between the Arctic Ocean under the ice and the atmosphere above the ice. Moreover, the role of ice dynamics needs to be quantified in future investigations when more accurate sea ice import/export data for the CAA region are available.

8.2 Limitations

Due to the coarse spatial resolution of the passive microwave SIC product, we did not conduct the analysis on subregions of the CAA. We expect that each of the subregions follow the four phase retreat pattern, but the north and west subregions should have a time lag compared to the south and east subregions. Even though MODIS data have higher spatial resolution, they are greatly affected by cloud cover. Only very few cloud-free images can be found for a specific subregion for the spring and summer months. Thus,

MODIS products only have very limited use for detailed spatial-temporal sea ice retreat analysis.

Moreover, sea ice concentration and sea ice extent only provide partial information about the sea ice coverage. Other important parameters, such as ice thickness and sea ice motion, are not examined due to the scope of the current research. Sea ice movement from the Arctic Ocean to the CAA in September is an important factor that controls the summer minimum sea ice extent in the CAA, but passive microwave data do not have the capability to isolate sea ice import/export from sea ice melt.

Furthermore, the current research focused on the sea ice melt processes on a yearly basis. However, sea ice melt in the CAA is suspected to be influenced by processes that operate on the time scale of a few years, such as the drain-trap mechanism for MYI import as suggested in *Howell et al.* (2008b). Thus, the current research is only useful in defining the common processes that occur on a yearly basis. Only recently *Howell et al.* (2013) quantified sea ice dynamics for the main waterways of the CAA during the summer months. As no data was available at the time of this research, ice dynamics are not included in the correlation analysis for sea ice retreat and surface radiation.

Lastly, sea ice is influenced both by atmosphere and the ocean, and sea ice melt occurs both at the surface and from the bottom. However, we have no observation data about how much ice melts at the bottom. Thus, the potential impacts of ocean on the sea ice is not discussed in this work.

8.3 Methodological Implications

Although the research methods used in this study were not new, they were combined in ways that had not been done previously. In particular, the current research focuses on the sea ice change and variability in the CAA from a daily to weekly perspective. As synoptic-scale weather systems often last a week or so, we want to understand the processes that govern sea ice retreat on a weekly scale. Even though there is considerable uncertainty with the daily data, we are able to tease out a consistent sea ice retreat pattern for the 22 years of the study interval. The evidence from this study suggests that the analysis on a

weekly scale is very necessary to help understand the mechanism of sea ice retreat in the CAA.

The study of the daily progression of sea ice and surface radiation using daily data has been shown to be quite effective in understanding the physical processes that work on a weekly scale. Furthermore, due to the focus on individual years, this method has been proven to be quite effective at uncovering the roles that each radiation term plays in the sea ice retreat.

8.4 Theoretical Implications

In the current research, we have verified the existence of melt ponding and pond drainage phases in the CAA on a regional scale using daily passive microwave sea ice concentration of the recent 22 years. Even though the thresholds used to identify the four phases from the daily sea ice extent change profiles are not mathematically rigorous, we are able to find the consistent signals of melt pond and pond drainage using passive microwave data. The results of this study provide a way to estimate the timing for each of the sea ice retreat phases in each year. The timing of the melt ponding phase can be used to predict the summer minimum sea ice extent. With detailed information about this four-phase process, we expect to contribute to the future modeling of sea ice retreats in the CAA region.

Although sea ice extent is underestimated by passive microwave data when melt ponds are present in the summer (*Agnew and Howell*, 2003), little attempt has been made to correct this bias in the published SIC data. Using a simplified assimilation method, SIC estimation has been improved by combining the original passive microwave data with MODIS ice surface temperature data. The proposed method can be easily implemented for operational use. However, we should also note the improvement can only be achieved for cloud-free regions. Thus, we can use MODIS data to help SIC estimation during the melt ponding phase only when valid MODIS data are available.

Sea ice interacts with the ocean below and atmosphere above through positive and negative feedback processes. The relationships between sea ice melt and radiation are an area of active research. We explored the relationships between the daily progression of

surface radiation and SIC daily changes. Sea ice retreat in phase 2 and phase 3 are found to decrease the percentage of TOA shortwave radiation that reach the surface because of the presence of the melt pond, which produces a negative feedback. Although this negative feedback was also mentioned by *Inoue et al.* (2005) for the central Arctic, we verified the existence of this negative feedback for the CAA region. Future modeling of the sea ice and atmosphere interaction can be improved by adding this feedback.

We did not find any consistent relationship between the downward shortwave/longwave radiation and sea ice loss in the CAA. Part of the problem might raise from how well ERA-interim models sea ice melt in their radiation calculation. Through detailed case studies, we identified the progression of surface radiation anomalies in individual years. In this work, we choose not to use net shortwave radiation, because the calculation of net shortwave radiation in the ERA-interim takes into account surface conditions, including the use of passive microwave sea ice concentration data (*Dee et al.*, 2011), thus creating potential for false inferences. Moreover, the parameterization of sea ice albedo in the ERA-interim is based on a very crude seasonal cycle.

A large volume of sea ice data has been accumulated daily for more than thirty years. Daily, monthly, and seasonal mean maps are generally used to show sea ice conditions. A sequence of maps is needed if we want to show a full picture of how sea ice is changing through a year. In this research, we proposed a sea ice phenology-based classification and a phenoregion map is produced each year. With one phenoregion map each year, we can easily tell what is the sea ice condition in the certain location during a certain time of the year. Thus, the phenoregion map is good visualization tool for sea ice analysis and change detection.

8.5 Relation to Other Studies of the CAA

Although in this study, we focus on the daily progression of sea ice retreat in spring and summer months, the results can nonetheless be related to other studies about sea ice in the CAA as described in Chapter 2.

Sea ice in the CAA is mainly landfast at the beginning of each melt season, composed

by both FYI and MYI. The retreat of sea ice is normally influenced by thermodynamic and dynamic processes. At the start of the melt season, thermodynamic processes play a significant role by melting sea ice because sea ice is all landfast. However, dynamic processes come into play when landfast ice in the channels of the CAA become mobile in late summer, especially in August and September. Thus, in addition to melt, ice motion is another important factor that determines the retreat of sea ice in the CAA region. The summer minimum sea ice in the CAA mainly depends on two factors: the amount of sea ice that melt in the spring and summer, and the sea ice exchange between the CAA, Arctic Ocean, and Baffin Bay. Using passive microwave data only, our research can only quantify the total change of sea ice from April to September. By examining the detailed sea ice retreat phases, we mainly focus on the spring and early summer during melt ponding and pond drainage.

Ice dynamics, including ice import/export between the Arctic Ocean, the CAA and Baffin Bay, is totally not considered in the current study. As reviewed in Chapter 2, there is inconsistency between the ice dynamics calculations in *Howell et al.* (2013) and *Howell et al.* (2009). Ice dynamics quantification in the CAA region has much larger uncertainty in the summer season compared to that in the winter. Based on the most recent study of *Howell et al.* (2013) for the period of 1997 to 2012, there are a mean ice area import of $5\times 10^3\ km^2$ through the M'Clure Strait from May to September and a mean ice area import of $4\times 10^3\ km^2$ from August to September with negligible ice exchange from May to July through the QEI gates. Thus, the total mean ice import from Arctic Ocean to the CAA is $+9\times 10^3\ km^2$ from May to September. Compared to the total ice loss of approximately $500\times 10^3\ km^2$ from April to Sept., it is speculated that ice dynamics play a relatively minor role compared to ice thermodynamics in sea ice melt in the CAA region. Meanwhile, ice export through Jones Sound and Lancaster Sound has not yet been quantified. Even though summer ice import/export is small when mean values of several years are averaged, ice dynamics do play a critical role in several years.

8.6 Recommendations for Future Work

The following recommendations can be made for future work:

- Considering that the spatial area covered by the CAA region is quite large, the current analysis of daily sea ice extent change can be extended to a subregion level if datasets with higher spatial resolution are available. In addition to ice concentration, ice thickness is another important parameter of sea ice especially for the CAA region because of the existence of FYI and MYI. Ice thickness and volume can provide insights about the sea ice dynamics between the CAA and other neighbouring regions. However, sea ice thickness data in the CAA region is rather scarce at the moment. New satellite missions, such as the European Space Agency's CryoSat-2 (*Laxon et al.*, 2013), have the potential to provide new datasets of ice concentration and ice thickness.

- Passive microwave sea ice data are low spatial resolution, but they are quite consistent through the past thirty years. Canadian Ice Service sea ice archives have better spatial resolution and ice type information. MODIS and RADARSAT images also have sea ice information. Each data source has its own advantages and provides certain information about different aspects of sea ice. The integration of information from several different sources will be beneficial for better estimation of the ice condition. Data assimilation techniques have the potential of fusion of different datasets and provide better sea ice estimation.

- The investigation of how surface radiation relates to sea ice retreat needs further work. Independent radiation datasets that do not rely on the sea ice data will help isolate the role of each radiation term in influencing the sea ice retreat. Numerical models that integrate atmospheric, ocean, and ice components using reanalysis data can be used to study and isolate the factors that influence the sea ice in the CAA. The sensitivity of each component can be teased out through carefully designed experiment.

References

Agnew, T., and S. Howell, The use of operational ice charts for evaluating passive microwave ice concentration data, *Atmosphere-ocean*, *41*(4), 317–331, 2003.

Agnew, T., and A. Silis, Spring-season climate variability in the central Canadian Arctic Islands, *Annals of Glaciology*, *21*, 330–336, 1995.

Agnew, T., A. Lambe, and D. Long, Estimating sea ice area flux across the Canadian Arctic Archipelago using enhanced AMSR-E, *Journal of Geophysical Research*, *113*(C10), C10,011, 2008.

Alt, B., K. Wilson, and T. Carrieres, A case study of old-ice import and export through Peary and Sverdrup Channels in the Canadian Arctic Archipelago: 1998-2005, *Annals of Glaciology*, *44*(1), 329–338, 2006.

Andersen, S., R. Tonboe, S. Kern, and H. Schyberg, Improved retrieval of sea ice total concentration from spaceborne passive microwave observations using numerical weather prediction model fields: An intercomparison of nine algorithms, *Remote Sensing of Environment*, *104*(4), 374–392, 2006.

Andersen, S., R. Tonboe, L. Kaleschke, G. Heygster, and L. Pedersen, Intercomparison of passive microwave sea ice concentration retrievals over the high-concentration Arctic sea ice, *J. Geophys. Res*, *112*(C8), C08, 2007.

Anderson, M., and S. Drobot, Spatial and temporal variability in snowmelt onset over Arctic sea ice, *Annals of Glaciology*, *33*(1), 74–78, 2001.

Ashcraft, I. S., and D. G. Long, Comparison of methods for melt detection over Greenland using active and passive microwave measurements, *International Journal of Remote Sensing*, *27*(12), 2469–2488, 2006.

Asplin, M. G., J. V. Lukovich, and D. G. Barber, Atmospheric forcing of the Beaufort Sea ice gyre: Surface pressure climatology and sea ice motion, *Journal of Geophysical Research*, *114*(C1), C00A06, 2009.

Asplin, M. G., R. Galley, D. G. Barber, and S. Prinsenberg, Fracture of summer perennial sea ice by ocean swell as a result of Arctic storms, *Journal of Geophysical Research*, *117*(C6), C06,025, 2012.

Atkinson, D., et al., Canadian cryospheric response to an anomalous warm summer: a synthesis of the climate change action fund project The state of the arctic cryosphere during the extreme warm summer of 1998, *Atmosphere-Ocean*, *44*(4), 347–375, 2006.

Barber, D., T. Papakyriakou, E. LeDrew, and M. Shokr, An examination of the relation between the spring period evolution of the scattering coefficient (σ) and radiative fluxes over Jandfast sea-ice, *International Journal of Remote Sensing*, *16*(17), 3343–3363, 1995.

Barber, D., R. Galley, M. Asplin, R. De Abreu, K. Warner, M. Pućko, M. Gupta, S. Prinsenberg, and S. Julien, Perennial pack ice in the southern Beaufort Sea was not as it appeared in the summer of 2009, *Geophysical Research Letters*, *36*(24), L24,501, 2009.

Barry, R., and A. Perry, Synoptic climatology and its applications, *Synoptic and dynamic climatology. Routledge, New York*, pp. 547–603, 2001.

Beaven, S., and S. Gogineni, Fusion of satellite SAR with passive microwave data for sea ice remote sensing, in *Analysis of SAR Data of the Polar Oceans*, pp. 91–109, Springer, 1998.

Belchansky, G., D. Douglas, and N. Platonov, Duration of the Arctic sea ice melt season: Regional and interannual variability, 1979-2001, *Journal of Climate*, *17*(1), 67–80, 2004.

Bitz, C., D. Battisti, R. Moritz, and J. Beesley, Low-frequency variability in the Arctic atmosphere, sea ice, and upper-ocean climate system, *Journal of climate*, *9*(2), 394–408, 1996.

Bitz, C., M. Holland, E. Hunke, and R. Moritz, Maintenance of the sea-ice edge, *Journal of climate*, *18*(15), 2903–2921, 2005.

Brown, R., and P. Cote, Interannual variability of landfast ice thickness in the Canadian High Arctic, 1950-89, *Arctic*, pp. 273–284, 1992.

Buehner, M., A. Caya, L. Pogson, T. Carrieres, and P. Pestieau, A New Environment Canada Regional Ice Analysis System, *Atmosphere-Ocean*, *51*(1), 18–34, 2013.

Carsey, F., *Microwave remote sensing of sea ice*, vol. 68, American Geophysical Union, 1992.

Cavalieri, D., The validation of geophysical products using multisensor data, *Microwave Remote Sensing of Sea Ice*, *68*, 233–242, 1992.

Cavalieri, D., C. Parkinson, P. Gloersen, and H. Zwally, Sea ice concentration from Nimbus-7 SMMR and DMSP SSM/I-SSMIS passive microwave data, June 2007–August 2007. National Snow and Data Center, *Digital Media, Boulder, CO, USA*, 1996.

Cavalieri, D. J., P. Gloersen, and W. J. Campbell, Determination of sea ice parameters with the Nimbus 7 SMMR, *Journal of Geophysical Research*, *89*(D4), 5355–5369, 1984.

Cavalieri, D. J., B. A. Burns, and R. G. Onstott, Investigation of the effects of summer melt on the calculation of sea ice concentration using active and passive microwave data, *Journal of Geophysical Research: Oceans (1978–2012)*, *95*(C4), 5359–5369, 1990.

Caya, A., M. Buehner, and T. Carrieres, Analysis and forecasting of sea ice conditions with three-dimensional variational data assimilation and a coupled ice-ocean model, *Journal of Atmospheric and Oceanic Technology*, *27*(2), 353–369, 2010.

Chen, C., T. Lakhankar, P. Romanov, S. Helfrich, A. Powell, and R. Khanbilvardi, Validation of NOAA-Interactive Multisensor Snow and Ice Mapping System (IMS) by Comparison with Ground-Based Measurements over Continental United States, *Remote Sensing*, *4*(5), 1134–1145, 2012.

Comiso, J., and F. Nishio, Trends in the sea ice cover using enhanced and compatible AMSR-E, SSM/I, and SMMR data, *Journal of Geophysical Research*, *113*(C2), C02S07, 2008.

Comiso, J., D. Cavalieri, C. Parkinson, and P. Gloersen, Passive microwave algorithms for sea ice concentration: A comparison of two techniques, *Remote Sensing of Environment*, *60*(3), 357–384, 1997.

Coppin, P., I. Jonckheere, K. Nackaerts, B. Muys, and E. Lambin, Review ArticleDigital change detection methods in ecosystem monitoring: a review, *International journal of remote sensing*, *25*(9), 1565–1596, 2004.

de Beurs, K., and G. Henebry, Phenological Mixture Models: Using MODIS to Identify Key Phenological Endmembers and Their Spatial Distribution in the Northern Eurasian Semi-Arid Grain Belt., in *AGU Fall Meeting Abstracts*, vol. 1, p. 1066, 2006.

Decker, M., M. A. Brunke, Z. Wang, K. Sakaguchi, X. Zeng, and M. G. Bosilovich, Evaluation of the reanalysis products from GSFC, NCEP, and ECMWF using flux tower observations, *Journal of Climate*, *25*(6), 1916–1944, 2012.

Dee, D., and S. Uppala, Variational bias correction of satellite radiance data in the ERA-Interim reanalysis, *Quarterly Journal of the Royal Meteorological Society*, *135*(644), 1830–1841, 2009.

Dee, D., et al., The ERA-Interim reanalysis: Configuration and performance of the data assimilation system, *Quarterly Journal of the Royal Meteorological Society*, *137*(656), 553–597, 2011.

Derksen, C., et al., Variability and change in the Canadian cryosphere, *Climatic Change*, pp. 1–30, 2012.

Deser, C., and H. Teng, Evolution of Arctic sea ice concentration trends and the role of atmospheric circulation forcing, 1979–2007, *Geophysical Research Letters*, *35*(2), L02,504, 2008.

Drobot, S. D., and J. A. Maslanik, Interannual variability in summer Beaufort Sea ice conditions: Relationship to winter and summer surface and atmospheric variability, *Journal of geophysical research*, *108*(C7), 3233, 2003.

Drüe, C., and G. Heinemann, High-resolution maps of the sea-ice concentration from MODIS satellite data, *Geophysical research letters*, *31*(20), 2004.

Drüe, C., and G. Heinemann, Accuracy assessment of sea-ice concentrations from MODIS using in-situ measurements, *Remote sensing of environment*, *95*(2), 139–149, 2005.

Dulière, V., T. Fichefet, et al., On the assimilation of ice velocity and concentration data into large-scale sea ice models, *Ocean Science Discussions*, *4*(2), 265–301, 2007.

Ebert, E., and J. Curry, An intermediate one-dimensional thermodynamic sea ice model for investigating ice-atmosphere interactions, *Journal of Geophysical Research*, *98*(C6), 10–085, 1993.

Eisenman, I., Geographic muting of changes in the Arctic sea ice cover, *Geophysical Research Letters*, *37*, Art–No, 2010.

Eppler, D. T., et al., Passive microwave signatures of sea ice, *Microwave Remote Sensing of Sea Ice*, *68*, 47–68, 1992.

Fetterer, F., and N. Untersteiner, Observations of melt ponds on Arctic sea ice, *Journal of Geophysical Research*, *103*(C11), 24,821–24,835, 1998.

Fischbach, A., S. Amstrup, and D. Douglas, Landward and eastward shift of Alaskan polar bear denning associated with recent sea ice changes, *Polar Biology*, *30*(11), 1395–1405, 2007.

Flato, G., and R. Brown, Variability and climate sensitivity of landfast Arctic sea ice, *Journal of Geophysical Research*, *101*(C11), 25,767–25, 1996.

Fowler, C., W. Emery, and J. Maslanik, Satellite-derived evolution of Arctic sea ice age: October 1978 to March 2003, *Geoscience and Remote Sensing Letters, IEEE*, *1*(2), 71–74, 2004.

Francis, J., and E. Hunter, New insight into the disappearing Arctic sea ice, *Eos, Transactions American Geophysical Union*, *87*(46), 509, 2006.

Francis, J., E. Hunter, J. Key, and X. Wang, Clues to variability in Arctic minimum sea ice extent, *Geophysical Research Letters*, *32*(21), L21,501, 2005.

Gregory, S., *Statistical methods and the geographer*, Longmans London, 1963.

Hall, D., J. Key, K. Casey, G. Riggs, and D. Cavalieri, Sea ice surface temperature product from MODIS, *Geoscience and Remote Sensing, IEEE Transactions on*, *42*(5), 1076–1087, 2004.

Hall, D. K., J. E. Box, K. A. Casey, S. J. Hook, C. A. Shuman, and K. Steffen, Comparison of satellite-derived and in-situ observations of ice and snow surface temperatures over Greenland, *Remote Sensing of Environment*, *112*(10), 3739–3749, 2008.

Hall, D. K., S. V. Nghiem, C. B. Schaaf, N. E. DiGirolamo, and G. Neumann, Evaluation of surface and near-surface melt characteristics on the Greenland Ice Sheet using MODIS and QuikSCAT data, *Journal of Geophysical Research: Earth Surface (2003–2012)*, *114*(F4), 2009.

Hall, D. K., J. C. Comiso, N. E. DiGirolamo, C. A. Shuman, J. R. Key, and L. S. Koenig, A satellite-derived climate-quality data record of the clear-sky surface temperature of the Greenland ice sheet, *Journal of Climate*, *25*(14), 4785–4798, 2012.

Hall, D. K., J. C. Comiso, N. E. DiGirolamo, C. A. Shuman, J. E. Box, and L. S. Koenig, Variability in the surface temperature and melt extent of the Greenland ice sheet from MODIS, *Geophysical Research Letters*, 2013.

Hargrove, W., J. Spruce, G. Gasser, and F. Hoffman, Toward a national early warning system for forest disturbances using remotely sensed canopy phenology, *Photogrammetric Engineering & Remote Sensing*, *75*(10), 2009.

Howell, S., A. Tivy, J. Yackel, and R. Scharien, Application of a SeaWinds/QuikSCAT sea ice melt algorithm for assessing melt dynamics in the Canadian Arctic Archipelago, *Journal of geophysical research*, *111*(C7), C07,025, 2006.

Howell, S., A. Tivy, J. Yackel, B. Else, and C. Duguay, Changing sea ice melt parameters in the Canadian Arctic Archipelago: Implications for the future presence of multiyear ice, *J. Geophys. Res*, *113*(C09030), 2008a.

Howell, S., A. Tivy, J. Yackel, and S. McCourt, Multi-year sea-ice conditions in the western Canadian arctic archipelago region of the northwest passage: 1968–2006, *Atmosphere-ocean*, *46*(2), 229–242, 2008b.

Howell, S., C. Duguay, and T. Markus, Sea ice conditions and melt season duration variability within the Canadian Arctic Archipelago: 1979-2008, *Geophysical Research Letters*, *36*, L10,502, 2009.

Howell, S., A. Tivy, T. Agnew, T. Markus, and C. Derksen, Extreme low sea ice years in the Canadian Arctic Archipelago: 1998 versus 2007, *Journal of Geophysical Research*, *115*(C10), C10,053, 2010.

Howell, S. L., T. Wohlleben, M. Dabboor, C. Derksen, A. Komarov, and L. Pizzolato, Recent changes in the exchange of sea ice between the Arctic Ocean and the Canadian Arctic Archipelago, *Journal of Geophysical Research: Oceans*, 2013.

Im, J., and J. Jensen, A change detection model based on neighborhood correlation image analysis and decision tree classification, *Remote Sensing of Environment*, *99*(3), 326–340, 2005.

Inoue, J., T. Kikuchi, D. Perovich, and J. Morison, A drop in mid-summer shortwave radiation induced by changes in the ice-surface condition in the central Arctic, *Geophysical research letters*, *32*(13), L13,603, 2005.

Inoue, J., T. Kikuchi, and D. Perovich, Effect of heat transmission through melt ponds and ice on melting during summer in the Arctic Ocean, *Journal of Geophysical Research*, *113*(C5), C05,020, 2008.

Inoue, J., M. Hori, T. Enomoto, and T. Kikuchi, Intercomparison of surface heat transfer near the Arctic marginal ice zone for multiple reanalyses: A case study of September 2009, *SOLA*, *7*(0), 57–60, 2011.

Intrieri, J., M. Shupe, T. Uttal, and B. McCarty, An annual cycle of Arctic cloud characteristics observed by radar and lidar at SHEBA, *Journal of Geophysical Research*, *107*(C10), 8030, 2002.

Itoh, M., J. Inoue, K. Shimada, S. Zimmermann, T. Kikuchi, J. Hutchings, F. McLaughlin, and E. Carmack, Acceleration of sea-ice melting due to transmission of solar radiation through ponded ice area in the Arctic Ocean: results of in situ observations from icebreakers in 2006 and 2007, *Annals of Glaciology*, *52*(57), 249–260, 2011.

Jeffers, S., T. Agnew, B. Alt, R. De Abreu, and S. McCourt, Investigating the anomalous sea-ice conditions in the Canadian High Arctic (Queen Elizabeth Islands) during summer 1998, *Annals of Glaciology*, *33*(1), 507–512, 2001.

Johannessen, O. M., and N. Ivanova, Sea Ice Area and Extent obtained from algorithms: Norsex, NASA Team, UMass-AES, Bootstrap, Cal Val, Bristol, TUD and ASI @ONLINE, 2013.

Kaleschke, L., G. Heygster, C. Lüpkes, A. Bochert, J. Hartmann, J. Haarpaintner, and T. Vihma, SSM/I sea ice remote sensing for mesoscale ocean-atmosphere interaction analysis: Ice and icebergs, *Canadian Journal of Remote Sensing*, *27*(5), 526–537, 2001.

Kapsch, M.-L., R. G. Graversen, and M. Tjernström, Springtime atmospheric energy transport and the control of Arctic summer sea-ice extent, *Nature Climate Change*, 2013.

Kay, J., T. L'Ecuyer, A. Gettelman, G. Stephens, and C. O'Dell, The contribution of cloud and radiation anomalies to the 2007 Arctic sea ice extent minimum, *Geophysical Research Letters*, *35*(8), L08,503, 2008.

Key, J., J. Maslanik, T. Papakyriakou, M. Serreze, and A. Schweiger, On the validation of satellite-derived sea ice surface temperature, *Arctic*, pp. 280–287, 1994.

Kwok, R., Exchange of sea ice between the Arctic Ocean and the Canadian Arctic Archipelago, *Geophysical research letters*, *33*(16), 16,501, 2006.

Laxon, S. W., et al., CryoSat-2 estimates of Arctic sea ice thickness and volume, *Geophysical Research Letters*, 2013.

LeDrew, E. F., D. Johnson, and J. A. Maslanik, An examination of atmospheric mechanisms that may be responsible for the annual reversal of the Beaufort Sea ice field, *International journal of climatology*, *11*(8), 841–859, 1991.

Lesins, G., T. J. Duck, and J. R. Drummond, Surface Energy Balance Framework for Arctic Amplification of Climate Change, *Journal of Climate*, *25*(23), 8277–8288, doi: 10.1175/JCLI-D-11-00711.1, 2012.

Light, B., T. Grenfell, and D. Perovich, Transmission and absorption of solar radiation by Arctic sea ice during the melt season, *J. Geophys. Res*, *113*, C03,023, 2008.

Lindsay, R., Temporal variability of the energy balance of thick Arctic pack ice, *Journal of climate*, *11*(3), 313–333, 1998.

Lindsay, R., and J. Zhang, Assimilation of ice concentration in an ice-ocean model, *Journal of Atmospheric and Oceanic Technology*, *23*(5), 742–749, 2006.

Lisæter, K. A., J. Rosanova, and G. Evensen, Assimilation of ice concentration in a coupled ice–ocean model, using the Ensemble Kalman filter, *Ocean Dynamics*, *53*(4), 368–388, 2003.

Liu, J., J. Curry, W. Rossow, J. Key, and X. Wang, Comparison of surface radiative flux data sets over the Arctic Ocean, *Journal of geophysical research*, *110*(C2), C02,015, 2005.

Lorenc, A. C., Analysis methods for numerical weather prediction, *Quarterly Journal of the Royal Meteorological Society*, *112*(474), 1177–1194, 1986.

Lu, D., P. Mausel, E. Brondizio, and E. Moran, Change detection techniques, *International journal of remote sensing*, *25*(12), 2365–2401, 2004.

Lubin, D., and R. Massom, Remote sensing of earth's polar regions: Opportunities for computational science, *Computing in Science & Engineering*, *9*(1), 58–71, 2007.

Lubin, D., R. Massom, and P. Blondel, Basic remote-sensing principles relating to the measurement of sea ice and its snow cover, *Polar remote sensing. Volume 1: atmosphere and oceans*, pp. 356–380, 2006.

Lukovich, J., and D. Barber, Atmospheric controls on sea ice motion in the southern Beaufort Sea, *Journal of geophysical research*, *111*(D18), D18,103, 2006.

Maksimovich, E., and T. Vihma, The effect of surface heat fluxes on interannual variability in the spring onset of snow melt in the central Arctic Ocean, *Journal of Geophysical Research*, *117*(C7), C07,012, 2012.

Marko, J. R., *Satellite-Based Study of Sea Ice Dynamics in the Central Canadian Arctic Archipelago*, Contractor Rep. Ser. 77-4, 106 pp., Canada. Dept. of the Environment. Institute of Ocean Sciences, Patricia Bay, Victoria, B.C., 1977.

Markus, T., and D. Cavalieri, An enhancement of the NASA Team sea ice algorithm, *Geoscience and Remote Sensing, IEEE Transactions on*, *38*(3), 1387–1398, 2000.

Markus, T., J. Stroeve, and J. Miller, Recent changes in Arctic sea ice melt onset, freezeup, and melt season length, *Journal of Geophysical Research*, *114*(C12), C12,024, 2009.

Maslanik, J., C. Fowler, J. Stroeve, S. Drobot, J. Zwally, D. Yi, and W. Emery, A younger, thinner Arctic ice cover: Increased potential for rapid, extensive sea-ice loss, *Geophysical Research Letters*, *34*(24), L24,501, 2007.

Maslanik, J., J. Stroeve, C. Fowler, and W. Emery, Distribution and trends in Arctic sea ice age through spring 2011, *Geophysical Research Letters*, *38*(13), L13,502, 2011.

Meier, W. N., and C. Haas, *Changes in the physical state of sea ice. Snow, water, ice and permafrost in the Arctic (SWIPA), Arctic Monitoring and Assessment Programme (AMAP)*, Cambridge University Press, 2011.

Melling, H., Sea ice of the northern Canadian Arctic Archipelago, *Journal of Geophysical Research*, *107*(C11), 3181, 2002.

Melling, H., Sea-Ice Observation: Advances and Challenges, *Arctic Climate Change*, pp. 27–115, 2012.

Melling, H., R. Lake, D. Topham, and D. Fissel, Oceanic thermal structure in the western Canadian Arctic, *Continental Shelf Research*, *3*(3), 233–258, 1984.

Melling, H., R. Francois, P. Myers, W. Perrie, A. Rochon, and R. Taylor, The Arctic Oceana Canadian perspective from IPY, *Climatic Change*, pp. 1–25, 2012.

Moe, B., et al., Climate change and phenological responses of two seabird species breeding in the high-Arctic, *Marine Ecology Progress Series*, *393*, 235–246, 2009.

Muench, R. D., The physical oceanography of the northern Baffin Bay region., *Tech. rep.*, DTIC Document, 1971.

Nghiem, S., P. Clemente-Colón, I. Rigor, D. Hall, and G. Neumann, Seafloor control on sea ice, *Deep Sea Research Part II: Topical Studies in Oceanography*, 2012.

Nicolaus, M., S. Gerland, S. Hudson, S. Hanson, J. Haapala, and D. Perovich, Seasonality of spectral albedo and transmittance as observed in the Arctic Transpolar Drift in 2007, *Journal of Geophysical Research*, *115*(C11), C11,011, 2010.

Nicolaus, M., C. Katlein, J. Maslanik, and S. Hendricks, Changes in Arctic sea ice result in increasing light transmittance and absorption, *Geophysical Research Letters*, *39*(24), 2012.

Nussbaumer, E., and R. Pinker, The role of shortwave radiation in the 2007 Arctic sea ice anomaly, *Geophysical Research Letters*, *39*(15), L15,808, 2012.

Overland, J. E., J. A. Francis, E. Hanna, and M. Wang, The recent shift in early summer Arctic atmospheric circulation, *Geophysical Research Letters*, *39*(19), 2012.

Parkinson, C., and D. Cavalieri, Arctic sea ice variability and trends, 1979–2006, *Journal of Geophysical Research*, *113*(C7), C07,003, 2008.

Parkinson, C. L., and J. C. Comiso, On the 2012 Record Low Arctic Sea Ice Cover: Combined Impact of Preconditioning and an August Storm, *Geophysical Research Letters*, 2013.

Partington, K. C., A data fusion algorithm for mapping sea-ice concentrations from Special Sensor Microwave/Imager data, *Geoscience and Remote Sensing, IEEE Transactions on*, *38*(4), 1947–1958, 2000.

Perovich, D., On the aggregate-scale partitioning of solar radiation in Arctic sea ice during the Surface Heat Budget of the Arctic Ocean (SHEBA) field experiment, *Journal of Geophysical Research*, *110*(C3), C03,002, 2005.

Perovich, D., and C. Polashenski, Albedo evolution of seasonal Arctic sea ice, *Geophysical Research Letters*, *39*(8), L08,501, 2012.

Perovich, D., and J. Richter-Menge, Loss of Sea Ice in the Arctic*, *Annual Review of Marine Science*, *1*, 417–441, 2009.

Perovich, D., S. Nghiem, T. Markus, and A. Schweiger, Seasonal evolution and interannual variability of the local solar energy absorbed by the Arctic sea ice–ocean system, *Journal of Geophysical Research*, *112*(C3), C03,005, 2007a.

Perovich, D., J. Richter-Menge, K. Jones, and B. Light, Sunlight, water, and ice: Extreme Arctic sea ice melt during the summer of 2007, *Geophysical Research Letters*, *35*(11), L11,501, 2008.

Perovich, D., K. Jones, B. Light, H. Eicken, T. Markus, J. Stroeve, and R. Lindsay, Solar partitioning in a changing Arctic sea-ice cover, *Annals of Glaciology*, *52*(57), 192–196, 2011a.

Perovich, D., J. Richter-Menge, K. Jones, B. Light, B. Elder, C. Polashenski, D. Laroche, T. Markus, and R. Lindsay, Arctic sea-ice melt in 2008 and the role of solar heating, *Annals of Glaciology*, *52*(57), 355–359, 2011b.

Perovich, D. K., B. Light, H. Eicken, K. F. Jones, K. Runciman, and S. V. Nghiem, Increasing solar heating of the Arctic Ocean and adjacent seas, 1979-2005: Attribution and role in the ice-albedo feedback, *Geophys. Res. Lett.*, *34*(19), 2007b.

Persson, P., Onset and end of the summer melt season over sea ice: thermal structure and surface energy perspective from SHEBA, *Climate dynamics*, *39*(6), 1349–1371, 2012.

Persson, P., C. Fairall, E. Andreas, P. Guest, and D. Perovich, Measurements near the Atmospheric Surface Flux Group tower at SHEBA: Near-surface conditions and surface energy budget, *J. Geophys. Res*, *107*(10.1029), 2002.

Petrich, C., H. Eicken, J. Zhang, J. Krieger, Y. Fukamachi, and K. Ohshima, Coastal landfast sea ice decay and breakup in northern Alaska: Key processes and seasonal prediction, *Journal of Geophysical Research*, *117*(C2), C02,003, 2012.

Piwowar, J., and C. Derksen, Spatial-Temporal Variability of Northern Hemisphere Sea Ice Concentrations and Concurrent Atmospheric Teleconnections, *Journal of Environmental Informatics*, *11*(2), 103–122, 2008.

Piwowar, J., and E. LeDrew, Principal components analysis of Arctic ice conditions between 1978 and 1987 as observed from the SMMR data record, *Canadian journal of remote sensing*, *22*(4), 390–403, 1996.

Piwowar, J., D. Peddle, and E. LeDrew, Temporal mixture analysis of Arctic Sea ice imagery: a new approach for monitoring environmental change, *Remote Sensing of Environment*, *63*(3), 195–207, 1998.

Polashenski, C., D. Perovich, and Z. Courville, The mechanisms of sea ice melt pond formation and evolution, *Journal of Geophysical Research*, *117*(C1), C01,001, 2012.

Polyakov, I. V., A. V. Pnyushkov, and L. A. Timokhov, Warming of the Intermediate Atlantic Water of the Arctic Ocean in the 2000s, *Journal of Climate*, *25*(23), 8362–8370, doi:10.1175/JCLI-D-12-00266.1, 2012a.

Polyakov, I. V., J. E. Walsh, and R. Kwok, Recent Changes of Arctic Multiyear Sea Ice Coverage and the Likely Causes, *Bulletin of the American Meteorological Society*, *93*(2), 145–151, doi:10.1175/BAMS-D-11-00070.1, 2012b.

Rampal, P., J. Weiss, C. Dubois, and J. Campin, IPCC climate models do not capture Arctic sea ice drift acceleration: Consequences in terms of projected sea ice thinning and decline, *J. Geophys. Res*, *116*, C00D07, 2011.

Ramseier, R., Sea ice validation, *Final Report, Naval Research Laboratory, Washington, DC*, 1991.

Riggs, G., K. Hall, and V. Salomonson, MODIS Sea Ice Products User Guide to Collection 5, 2006.

Rigor, I., and J. Wallace, Variations in the age of Arctic sea-ice and summer sea-ice extent, *Geophysical Research Letters*, *31*(9), L09,401, 2004.

Rigor, I. G., J. M. Wallace, and R. L. Colony, Response of sea ice to the Arctic Oscillation, *Journal of Climate*, *15*(18), 2648–2663, 2002.

Rösel, A., and L. Kaleschke, Comparison of different retrieval techniques for melt ponds on Arctic sea ice from Landsat and MODIS satellite data, *Annals of Glaciology*, *52*(57), 185–191, 2011.

Rösel, A., and L. Kaleschke, Exceptional melt pond occurrence in the years 2007 and 2011 on the Arctic sea ice revealed from MODIS satellite data, *Journal of Geophysical Research*, *117*(C5), C05,018, 2012.

Rösel, A., L. Kaleschke, and G. Birnbaum, Melt ponds on Arctic sea ice determined from MODIS satellite data using an artificial neural network, *The Cryosphere*, *6*, 431–446, 2012.

Scambos, T. A., T. M. Haran, and R. Massom, Validation of AVHRR and MODIS ice surface temperature products using in situ radiometers, *Annals of Glaciology*, *44*(1), 345–351, 2006.

Scott, K. A., M. Buehner, A. Caya, and T. Carrieres, Direct Assimilation of AMSR-E Brightness Temperatures for Estimating Sea Ice Concentration, *Monthly Weather Review*, *140*(3), 997–1013, 2012.

Scott, K. A., M. Buehner, A. Caya, and T. Carrieres, A preliminary evaluation of the impact of assimilating AVHRR data on sea ice concentration analyses, *Remote Sensing of Environment*, *128*, 212–223, 2013.

Screen, J., and I. Simmonds, The central role of diminishing sea ice in recent Arctic temperature amplification, *Nature*, *464*(7293), 1334–1337, 2010.

Screen, J., and I. Simmonds, Declining summer snowfall in the Arctic: causes, impacts and feedbacks, *Climate dynamics*, *38*(11), 2243–2256, 2012.

Screen, J. A., I. Simmonds, and K. Keay, Dramatic interannual changes of perennial Arctic sea ice linked to abnormal summer storm activity, *Journal of Geophysical Research*, *116*(D15), D15,105, 2011.

Sedlar, J., et al., A transitioning Arctic surface energy budget: the impacts of solar zenith angle, surface albedo and cloud radiative forcing, *Climate dynamics*, *37*(7), 1643–1660, 2011.

Serreze, M., and R. Barry, *The Arctic climate system*, Cambridge University Press, 2005.

Serreze, M., A. Barrett, A. Slater, M. Steele, J. Zhang, and K. Trenberth, The large-scale energy budget of the Arctic, *Journal of geophysical research*, *112*(D11), D11,122, 2007a.

Serreze, M., M. Holland, and J. Stroeve, Perspectives on the Arctic's shrinking sea-ice cover, *science*, *315*(5818), 1533–1536, 2007b.

Serreze, M. C., and A. P. Barrett, The summer cyclone maximum over the central Arctic Ocean, *Journal of Climate*, *21*(5), 1048–1065, 2008.

Serreze, M. C., F. Carse, R. G. Barry, and J. C. Rogers, Icelandic low cyclone activity: Climatological features, linkages with the NAO, and relationships with recent changes in the Northern Hemisphere circulation, *Journal of Climate*, *10*(3), 453–464, 1997.

Shine, K., Parametrization of the shortwave flux over high albedo surfaces as a function of cloud thickness and surface albedo, *Quarterly Journal of the Royal Meteorological Society*, *110*(465), 747–764, 1984.

Shokr, M., and T. Markus, Comparison of NASA Team2 and AES-York ice concentration algorithms against operational ice charts from the Canadian ice service, *Geoscience and Remote Sensing, IEEE Transactions on*, *44*(8), 2164–2175, 2006.

Shupe, M., and J. Intrieri, Cloud radiative forcing of the Arctic surface: The influence of cloud properties, surface albedo, and solar zenith angle, *Journal of climate*, *17*(3), 616–628, 2004.

Simmonds, I., and K. Keay, Extraordinary September Arctic sea ice reductions and their relationships with storm behavior over 1979–2008, *Geophys. Res. Lett*, *36*, L19,715, 2009.

Simmonds, I., and I. Rudeva, The great Arctic cyclone of August 2012, *Geophysical Research Letters*, *39*(23), 2012.

Simmonds, I., C. Burke, and K. Keay, Arctic climate change as manifest in cyclone behavior, *Journal of Climate*, *21*(22), 5777–5796, 2008.

Simmons, A., S. Uppala, D. Dee, and S. Kobayashi, ERA-Interim: New ECMWF reanalysis products from 1989 onwards, *ECMWF newsletter*, *110*, 25–35, 2007.

Small, C., Spatiotemporal dimensionality and Time-Space characterization of multitemporal imagery, *Remote Sensing of Environment*, *124*, 793–809, 2012.

Smith, D., and E. Barrett, Satellite mapping and monitoring of sea ice, *Unpublished Final Report to the Defence Research Agency, Contract Reference CB/RAE/9/2/4/2034/113/ARE, RSU, University of Bristol, UK*, 1994.

Spreen, G., L. Kaleschke, and G. Heygster, Sea ice remote sensing using AMSR-E 89-GHz channels, *J. Geophys. Res*, *113*(C2), C02, 2008.

Spreen, G., R. Kwok, and D. Menemenlis, Trends in Arctic sea ice drift and role of wind forcing: 1992–2009, *Geophysical Research Letters*, *38*(19), L19,501, 2011.

Stark, J. D., J. Ridley, M. Martin, and A. Hines, Sea ice concentration and motion assimilation in a sea ice- ocean model, *Journal of Geophysical Research: Oceans (1978–2012)*, *113*(C5), 2008.

Steele, M., J. Zhang, and W. Ermold, Mechanisms of summertime upper Arctic Ocean warming and the effect on sea ice melt, *Journal of Geophysical Research*, *115*(C11), C11,004, 2010.

Stroeve, J., T. Markus, W. Meier, and J. Miller, Recent changes in the Arctic melt season, *Annals of Glaciology*, *44*(1), 367–374, 2006.

Stroeve, J., M. Holland, W. Meier, T. Scambos, and M. Serreze, Arctic sea ice decline: Faster than forecast, *Geophysical Research Letters*, *34*(9), 9501, 2007.

Stroeve, J., A. Frei, J. McCREIGHT, and D. Ghatak, Arctic sea-ice variability revisited, *Annals of Glaciology*, *48*(1), 71–81, 2008.

Stroeve, J., M. Serreze, M. Holland, J. Kay, J. Malanik, and A. Barrett, The Arctics rapidly shrinking sea ice cover: a research synthesis, *Climatic change*, *110*(3), 1005–1027, 2012.

Stroeve, J. C., J. Maslanik, M. C. Serreze, I. Rigor, W. Meier, and C. Fowler, Sea ice response to an extreme negative phase of the Arctic Oscillation during winter 2009/2010, *Geophysical Research Letters*, *38*(2), L02,502, 2011.

Strong, C., G. Magnusdottir, and H. Stern, Observed feedback between winter sea ice and the North Atlantic Oscillation, *Journal of Climate*, *22*(22), 6021–6032, 2009.

Svendsen, E., K. Kloster, B. Farrelly, O. Johannessen, J. Johannessen, W. Campbell, P. Gloersen, D. Cavalieri, and C. Mätzler, Norwegian remote sensing experiment: Evaluation of the nimbus 7 scanning multichannel microwave radiometer for sea ice research, *Journal of Geophysical Research*, *88*(C5), 2781–2791, 1983.

Swift, C., L. Fedor, and R. Ramseier, An algorithm to measure sea ice concentration with microwave radiometers, *Journal of Geophysical Research: Oceans (1978–2012)*, *90*(C1), 1087–1099, 1985.

T., P. L., Improved spatial resolution of SSM/I products, *IMSI report No 8, Nansen Environmental and Remote Sensing Center, Bergen, Norway*, 1998.

Canadian Ice Service, Sea Ice Climatic Atlas for the Northern Canadian Waters 1981-2010, *Tech. rep.*, Canadian Ice Service, 2011.

Tivy, A., S. Howell, B. Alt, S. McCourt, R. Chagnon, G. Crocker, T. Carrieres, and J. Yackel, Trends and variability in summer sea ice cover in the Canadian Arctic based on the Canadian Ice Service Digital Archive, 1960–2008 and 1968–2008, *Journal of Geophysical Research*, *116*(C3), C03,007, 2011.

Tschudi, M., J. Maslanik, and D. Perovich, Derivation of melt pond coverage on Arctic sea ice using MODIS observations, *Remote Sensing of Environment*, *112*(5), 2605–2614, 2008.

Uttal, T., et al., Surface heat budget of the Arctic Ocean, *Bulletin of the American Meteorological Society*, *83*(2), 255–275, 2002.

Wallace, J., and D. Gutzler, Teleconnexions in the geopotential height field during the Northern Hemisphere winter, *Mon. Wea. Rev*, *109*(2), 784–812, 1981.

Wang, K., J. Debernard, A. K. Sperrevik, P. E. Isachsen, and T. Lavergne, A combined optimal interpolation and nudging scheme to assimilate OSISAF sea-ice concentration into ROMS, *Annals of Glaciology*, *54*, 62, 2013.

Wang, Q., P. Myers, X. Hu, and A. Bush, Flow Constraints on Pathways through the Canadian Arctic Archipelago, *Atmosphere-Ocean*, *50*(3), 373–385, 2012.

Wohlleben, T., S. E. Howell, T. Agnew, and A. Komarov, Sea-Ice Motion and Flux within the Prince Gustaf Adolf Sea, Queen Elizabeth Islands, Canada during 2010, *Atmosphere-Ocean*, (ahead-of-print), 1–17, 2012.

Yackel, J., D. Barber, T. Papakyriakou, and C. Breneman, First-year sea ice spring melt transitions in the Canadian Arctic Archipelago from time-series synthetic aperture radar data, 1992–2002, *Hydrological processes*, *21*(2), 253–265, 2007.

Zhang, J., M. Steele, R. Lindsay, A. Schweiger, and J. Morison, Ensemble 1-Year predictions of Arctic sea ice for the spring and summer of 2008, *Geophys. Res. Lett*, *35*(8), L08,502, 2008.

Zhang, J., R. Lindsay, A. Schweiger, and M. Steele, The impact of an intense summer cyclone on 2012 Arctic sea ice retreat, *Geophysical Research Letters*, 2013.

Zhang, X., J. E. Walsh, J. Zhang, U. S. Bhatt, and M. Ikeda, Climatology and interannual variability of arctic cyclone activity: 1948-2002, *Journal of Climate*, *17*(12), 2300–2317, 2004.